Absolute Value of the Magnetic Penetration Depth and Field Profile in the Meissner State of Exotic Superconductors $YBa_2Cu_3O_{6+x}$ and $Ba(Co_{0.074}Fe_{0.926})_2As_2$

by

Md Masrur Hossain

M.Sc., The University of British Columbia, 2006

A Thesis Submitted In Partial Fulfillment
Of The Requirements For The Degree Of

Doctor of Philosophy

in

The Faculty Of Graduate Studies

(Physics)

THE UNIVERSITY OF BRITISH COLUMBIA

(Vancouver)

October 2012

ABSTRACT

One of the fundamental quantities of a superconductor is the magnetic penetration depth, λ, which is the characteristic length scale that a magnetic field penetrates into the surface of a superconductor while in the Meissner state. In the clean limit the absolute value of λ is directly related to the superfluid density n_s via $1/\lambda^2 = \mu_0 e^2 n_s/m^*$, where m^* is the effective mass. Consequently, its variation as a function of temperature, doping and orientation are of central importance in testing microscopic theories of exotic superconductors.

A low energy beam of spin polarized muons has recently been developed, at the Paul Scherrer Institute, to directly measure λ in a superconductor. When a muon (μ^+) decays, it emits a fast decay positron preferentially along the direction of its spin due to the parity violating decay. The time evolution of statistical average direction of the spin polarization of the muon ensemble depends sensitively on the local magnetic field which can be monitored as a function of the mean depth of implantation. In this way it is possible to measure the field profile near the surface of a superconductor and extract the magnetic penetration depth in a direct manner which is not otherwise possible with conventional bulk methods.

In this thesis, accurate measurements of λ and its anisotropy$\left(\equiv \lambda_a/\lambda_b\right)$ have been made for three different oxygen (x = 6.52, 6.92 and 6.998) contents of $YBa_2Cu_3O_{6+x}$ as well as in $Ba(Co_{0.074}Fe_{0.926})_2As_2$. The measured values of λ and the in-plane anisotropies are considerably different from that reported in the literature, using less direct methods. The $a-b$ anisotropy is surprisingly insensitive to x in $YBa_2Cu_3O_{6+x}$. We observe an exponential decay of the magnetic field and corresponding supercurrent density deep inside the crystals. Small deviations from the London model are observed which indicate there is a suppression of the supercurrent density close to the surface. The measured (λ) values are also found to depart substantially from the Uemura relation $\left(T_c \propto 1/\lambda^2\right)$.

PREFACE

Results presented in section 4.1.1 has been published by Kiefl, R. F., Hossain, M. D., Wojek, B. M., Dunsiger, S. R., Morris, G. D., Prokscha, T., Salman, Z., Baglo, J., Bonn, D. A., Liang, R., Hardy W. N., Suter, A. Morenzoni, E. in Direct measurement of the London penetration depth in $YBa_2Cu_3O_{6.92}$ using low-energy μSR. Phys. Rev. B, **81**, 180502 (2010). The design of research methods, literature review, data analysis, were done by myself in consultation with my supervisor R. F. Kiefl. The manuscript of this paper was written primarily by R. F. Kiefl. The co-authors have been partly involved in taking the data and reviewing and commenting on the manuscripts, or supplying the studied samples. Sections 4.1.3 and 4.1.4 are currently in the process of being published. The results presented in section 4.2 is published by Ofer, O., Baglo, J. C., Hossain, M. D., Kiefl, R. F., Hardy, W. N., Thaler, A., Kim, H., Tanatar, M. A., Canfield, P. C., Prozorov, R., Luke, G. M., Morenzoni, E., Saadaoui, H., Suter, A., Prokscha, T., Wojek, B. M. and Salman, Z. in Absolute value and temperature dependence of the magnetic penetration depth in $Ba(Co_{0.074}Fe_{0.926})_2As_2$. Phys. Rev. B, **85**, 060506 (2012). A significant of part of data analysis was done by me. Manuscript was written by O. Ofer and microwave analysis was done by J. C. Baglo.

TABLE OF CONTENTS

LIST OF TABLES

LIST OF FIGURES

LIST OF SYMBOLS

$\Delta(\boldsymbol{k}, T)$	Momentum dependent superconducting energy gap, page 15	eV
κ	Ginzburg-Landau parameter, page 4	
T_c	Superconducting critical temperature, page 1	K
ξ	Ginzburg-Landau coherence length, page 5	m
λ	London penetration depth, page 1	m
λ_{ab}	Average magnetic penetration depth, page 72	m
Φ_0	Unit of flux quantum, page 4	$2.067\,833\,667 \times 10^{-15}$ Wb
ψ	Superconducting order parameter, page 1	
σ	Optical conductivity, page 9	
τ	Relaxation time, page 17	
H_c	Critical magnetic field, page 4	Tesla
n_s	Superfluid density, page 5	
T^*	Strange metallic phase temperature, page 6	K
γ_μ	Muon gyromagnetic ratio, page 26	MHz/Tesla
$\mathcal{A}(t)$	Time dependent muon asymmetry, page 40	
$\mathcal{R}$	Ratio of magnetic penetration depth, ie, $\frac{\lambda_a}{\lambda_b}$, page 58	
τ_μ	Muon lifetime, page 26	s

GLOSSARY

UBC University of British Columbia

PSI Paul Scherrer Institute, Villigen, Switzerland

CIFAR Canadian Institute for Advanced Research, Canada

TRIUMF TRI-University Meson Facility, Canada

NSERC Natural Sciences and Engineering Research Council of Canada

YBCO Yttrium Barium Copper Oxide/$YBa_2Cu_3O_{6+x}$

FE-PNICTIDE Fe-As Based Superconductors

MUSR Muon Spin Resonance/Rotation/Relaxation

QCP Quantum Critical Point

HTSC High Temperature Superconductor

ODLRO Off Diagonal Long Range Order

ACKNOWLEDGEMENT

First and foremost, I would like to thank my supervisor Rob Kiefl and his support and advice throughout the course of my PhD. I am very grateful for his responses to my inquiries and availability during my entire stay at UBC. I would also like to thank my committee members: D. A. Bonn, M. Franz, and A. Damascelli for their comments, and for reading the thesis.

I also thank Zaher Salman and Gerald Morris who have always been very helpful in providing software expertise and acting as general UNIX/LINUX gurus. Zaher's super-fast response to queries for technical help has been invaluable in many occasions. Special thanks to D. Arseneau for letting me use the fastest computer in μSR group in TRIUMF. This has saved many precious hours of analysis time and possible frustrations. Many thanks to R. Liang for providing the YBCO samples with three different oxygen contents. Also thanks to AMES laboratory for providing the FE-PNICTIDE samples.

I wish also to thank my colleagues in βNMR group. Special thanks to Susan Q. Song for helping taking magnetization data at AMPEL. A big thanks to J.C. Baglo for providing supplementary microwave analysis. My colleagues Terry Parolin, Dong Wang, Micheal Smadella, Hassan Saadaoui, Susan Q. Song, J.C. Baglo and others have spent many nights taking the actual data; for that and for the helpful discussions and good times we had together, I am very grateful.

The data in this project was taken over many years and a lot of people, other than the ones that have been already mentioned above, have helped to take shifts and helped doing supplementary analysis. I will also like to thank μSR support staff and colleagues at PSI, B. M. Wojek, T. Prokscha, A. Suter. Special thanks goes to B. M. Wojek for his critical and thorough analysis of data and valuable insight.

I would like to mention the βNMR technical support staff R. Abasalti, D. Arseneau, K. H. Chow, S. Dunsiger, B. Hitti, C. D. P. Levy, R. Miller, M. R. Pearson, and D. Vyas.

The μSR measurements were performed at PSI. These works were supported by NSERC, CIFAR and the U.S. Department of Energy.

Finally, thanks to the writers of LaTeX and many accompanying packages, used in typesetting this thesis.

CHAPTER 1 INTRODUCTION

1.1 Brief History of Superconductivity

Historically, superconductivity has played an important role in condensed matter physics. With the discovery of superconductivity in Hg [2], about 100 years ago, it remains a very active area of research with continuing surprises. Figure 1.1 roughly shows the number of publications on the phenomenon of superconductivity in the last decade. Before the discovery of the phenomena of superconductivity, it was known that the resistivity of a metal drops with decreasing temperature. In a perfect crystal, resistivity in metals is generally attributed to electron-phonon scattering (and to a lesser extent electron electron interactions) the rate of which is proportional to the thermally excited phonons. However, the number of thermally excited phonons is finite above absolute zero and thus the resistivity is expected to be non zero at any finite temperature. Consequently, K. Onnes' discovery of virtual absence of resistivity in Mercury below 4.15 K, in 1911 [3] was rather surprising. Soon after, in 1913, Lead was found to be superconducting below 7.2 K and after 17 years of this discovery, niobium was found to be superconducting at 9.2 K. The virtual absence of resistance in a superconductor has been demonstrated by experiments with persistent currents in superconducting rings. Such currents have a decay time of on the order of 10^5 years. The other important characteristic beyond zero resistivity is the Meissner effect in which magnetic field is expelled ([4] figure 1.2) out of a sample when it's cooled below the critical temperature T_c. The Meissner effect is different from perfect diamagnetism in a perfect conductor. In perfect diamagnetism, currents are generated to oppose any change in the applied field such that, if the sample already had non-zero magnetic flux through it, cooling through T_c wouldn't result in any flux expulsion. However, in the Meissner effect, the field is expelled from the sample when cooled below T_c. This Meissner effect led the London brothers [5] to propose equations to predict how the field is excluded from the sample and in particular, the field penetration near the surface. Londons' theory was later (1950) derived from the phenomenological theory of Ginzburg and Landau [6] (GL), who described superconductivity in terms of a macroscopic complex order parameter ψ which is a rough measure of the extent to which a system is ordered. In the case of superconductivity, the amplitude of the order parameter is proportional to superconducting electron density or condensate. One of the most remarkable aspects of a superconductor is that the electrons remain coherent over macroscopic distances. The QM phase at one position is correlated with the phase everywhere else in the sample.

Although the phenomenological GL theory had been successful, an accepted microscopic theory only came in 1957 from J. Bardeen, Leon Cooper and John Schrieffer [7, 8], now famously known as BCS theory. BCS theory explained superconductivity in terms of an electron-electron interaction mediated by short wavelength phonons and McMillan *et al.* predicted that supercon-

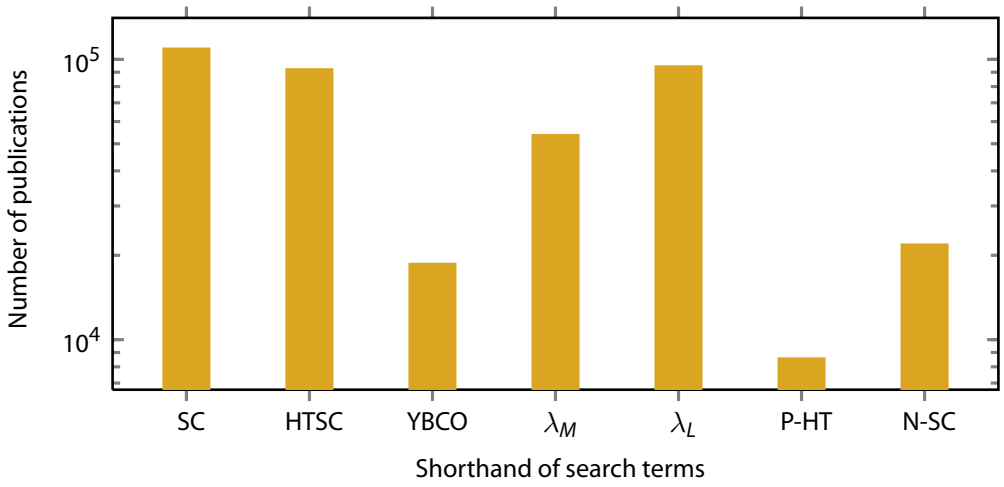

Figure 1.1 : Number of publications (year 2000 onwards) in log scale, for different search terms from a prominent search engine's scholar edition, done on August 7, 2012. Expansion of the shorthand terms: SC: superconductivity; HTSC: high temperature superconductivity; YBCO: YBCO; λ_M: magnetic penetration depth; λ_L: London penetration depth; P-HT: pseudogap in high temperature superconductivity; N-SC: normal state in high temperature superconductivity. As may be seen, an enormous scholarly interest in the phenomenon of superconductivity exists in contemporary condensed matter physics.

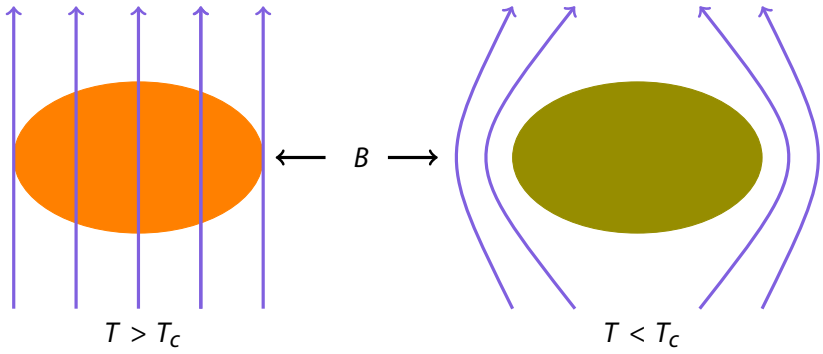

Figure 1.2 : Meissner effect for a type I superconductor. When a superconductor is placed in an external magnetic field H and cooled below its superconducting temperature T_c, the magnetic flux is abruptly expelled. For $B < B_c$, it penetrates the surface of the superconductor within the penetration depth λ.

ductivity may be found with critical temperatures $T_c \leq 28\,\mathrm{K}$ [9] (for Nb_3Sn). It was believed that the electron phonon interaction was strong enough to create lattice instablility and thus there was a fundamental limit to T_c from electron phonon interaction. The carriers of supercurrents were shown to be a pair of electrons ("Cooper pairs" [10]) with opposite spin and momentum. Many new metals and alloys with superconducting properties, at low temperatures, were found by 1980, with the noted exceptions of ferromagnets such as Fe, Ni. It was later realized that magnetic order is antagonistic to the conventional so called low-T_c superconductivity.

In 1986, J.G. Bednorz and K.A. Muller [11] discovered superconductivity in $La_{2-x}Ba_xCuO_4$ at 35 K, thus initiating the era of high-temperature superconductivity. Building on that, Maw-Kuen Wu and his graduate students, Ashburn and Torng [12] at the University of Alabama dis-

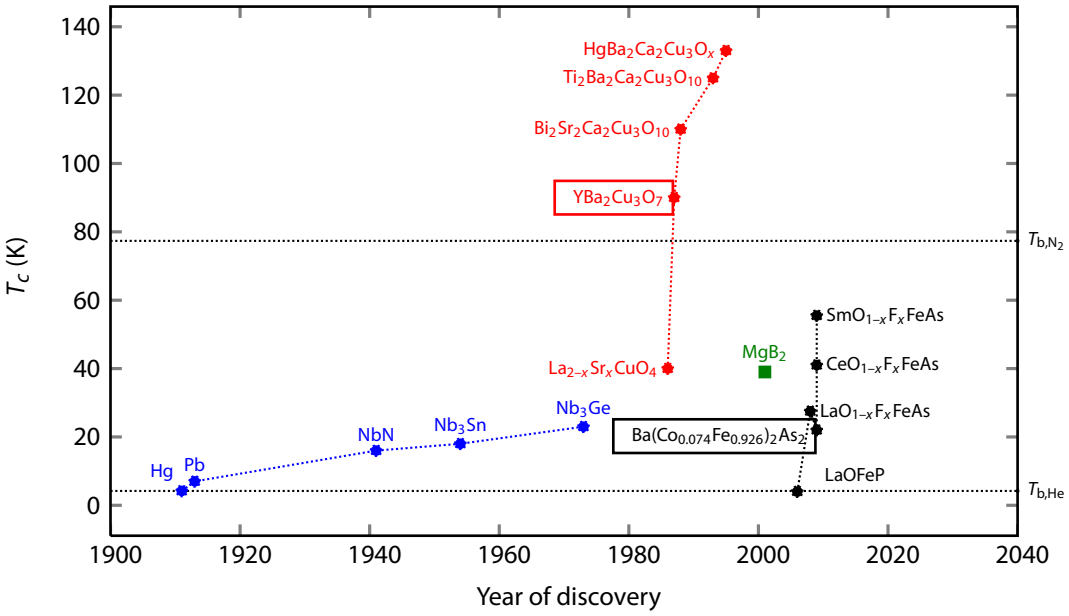

Figure 1.3 : Superconducting critical temperature ([13]) T_c has risen almost linearly with time, from 4 K to 40 K till about 1986. Around 1987, one of the CuO based high temperature superconductor family was found. In 2008, one new family of Fe-based superconductors were discovered. Due to the typical antagonistic relationship of superconductivity and magnetism, this was a significant surprise for science.

covered YBCO has a T_c of 93 K. Their work led to a rapid succession of new high temperature superconducting materials, ushering a new era in material science and chemistry. YBCO was the first family of materials to become superconducting above 77 K, the boiling point of liquid nitrogen. All materials developed before 1986 became superconducting only at temperatures near the boiling points of liquid helium $\left(T_{b,He} = 4.2\,K\right)$ or liquid hydrogen $\left(T_{b,H} = 20.28\,K\right)$ - the highest being Nb_3Ge at 23 K. Although met with initial skepticism, the observations were validated when Uchida *et. al.* and Chu *et. al* reproduced original results in 1987. In 2008, a new family of Fe-based superconductors were discovered. Due to the typical antagonistic relationship of superconductivity and magnetism, this was quite surprising. Remarkable progress has been made in discovering high-T_c superconductors as shown in the figure 1.3. As superconductivity is found in so many different material families, it is considered an almost "common" phenomenon for metals which have a partially filled conduction band. Nevertheless the discovery of high-T_c superconductivity has lead to many open questions regarding the microscopic mechanism.

1.2 Brief Review of Superconducting Properties

Besides having a critical temperature T_c, superconductors also have critical magnetic fields (H_c), above which their properties change. In this respect, superconductors are classified in two broad categories (figure 1.4), i) Type I, in which the material becomes normal above a critical magnetic field $H_{c,0}$. ii) Type II, in which the material has two critical magnetic fields H_{c1} and H_{c2}. In type II, at $H < H_{c1}$, the material remains in the Meissner state and at $H_{c1} < H < H_{c2}$, magnetic field

penetrates the material in the form of vortices carrying a quantized amount of magnetic flux (for a very detailed review, consult [14]) and for $H > H_{c2}$, it becomes normal. Two other parameters characterize superconductivity in general, namely the coherence length ξ and the magnetic penetration depth λ. The coherence length ξ is the distance over which order parameter ψ varies appreciably and penetration depth λ is the depth over which shielding currents circulate to expel the applied external field. λ and ξ are two fundamental length scales in superconductivity. Other parameters of interest such as Ginzburg-Landau parameter $\kappa = \frac{\lambda}{\xi}$, two critical fields H_{c1}, H_{c2}, thermodynamical critical field H_c may be derived from them:

$$H_{c1} = \frac{\Phi_0}{4\pi\lambda^2} \ln\left(\frac{\lambda}{\xi}\right), \tag{1.1a}$$

$$H_{c2} = \frac{\Phi_0}{2\pi\xi^2}, \tag{1.1b}$$

$$H_c = \frac{\sqrt{2}\Phi_0}{4\pi\lambda\xi}, \tag{1.1c}$$

where $\Phi_0 = \frac{h}{2e}$ is unit of flux quantum. The thermodynamic critical field H_c is related to the free energy difference between the normal and superconducting states.

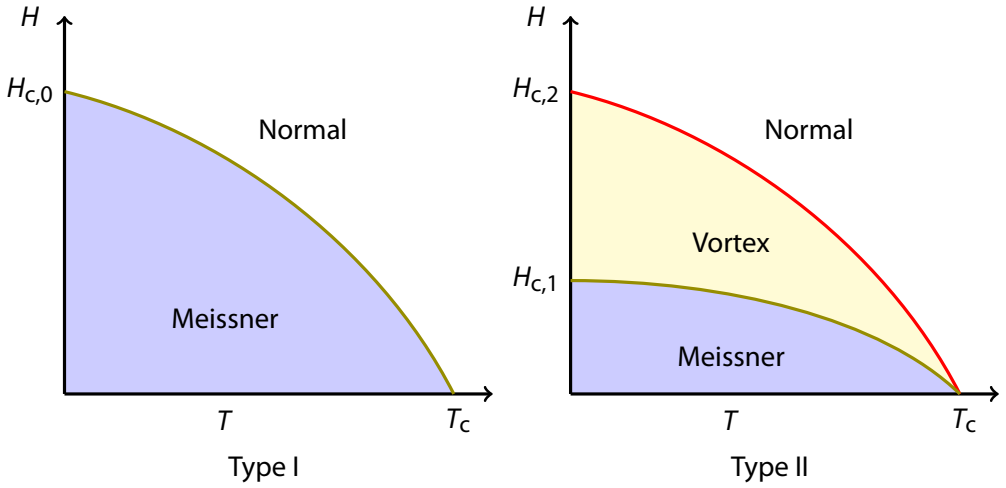

Figure 1.4 : Superconductivity is destroyed when the external field is too large or temperature too high. Superconductors are divided in two classes depending on the manner of this destruction. For type I superconductors, superconductivity is abruptly destroyed in a first order phase transition if $H > H_c$ or $T > T_c$. Type II superconductivity has a complete Meissner region (below $H < H_c$) in $H - T$ phase diagram, however, in the "vortex" ($H_{c1} < H < H_{c2}$) state, laminar vortices with normal state cores enter into superconductor and superconductivity is destroyed in a continuous 2nd order phase transition to a normal state. Most high-T_c superconductors are type II.

When the external magnetic field exceeds H_{c1} in a type II superconductor, the material enters into a "mixed state" in which laminar vortices with normal state cores enter into the superconductor. At the center of a vortex, superconductivity is completely destroyed, i.e, the order parameter $|\psi|^2$ vanishes (figure 1.5). However, the velocity of the carriers tends to increase as one

approaches the core. Beyond a radial distance of ξ, the superfluid density n_s and order parameter reaches its bulk value. The radius ξ is known as "vortex core". The supercurrent flowing around the vortex produces a magnetic field which is maximum at the center and decays approximately exponentially, with a length scale of λ in the radial direction. The vortices are usually arranged in a periodic lattice known as the Abrikosov lattice, the flux lattice or the flux line lattice. Vortices may also be dynamic and interacting depending on the level of doping and the magnetic field [15].

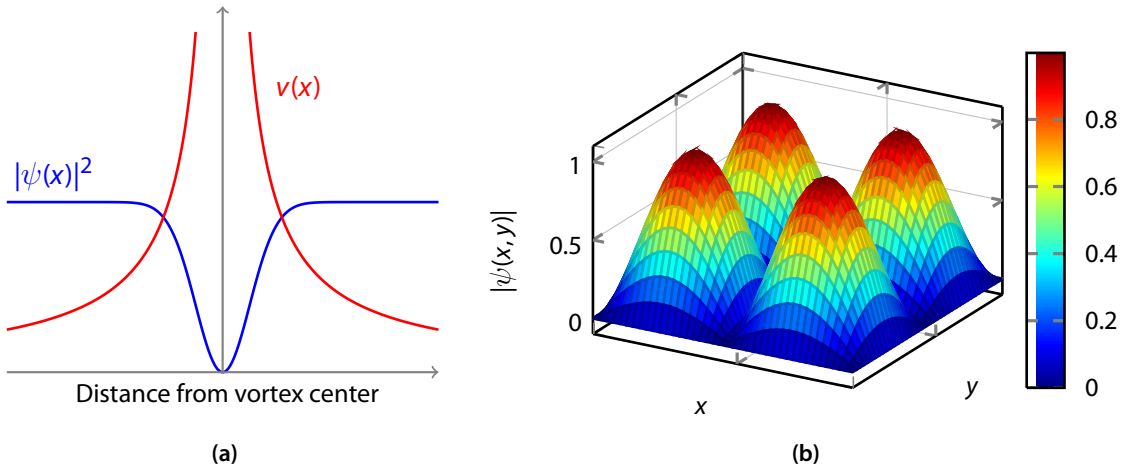

Figure 1.5 : Left: A schematic model of the electronic/magnetic structure of the HTSC vortex core. Superfluid velocity $v(x)$ rises and the HTSC order parameter $|\psi(x)|$ falls as the core is approached. Right: The superconducting order is suppressed at the cores of the vortices. The colored surface shows the envelope of this order parameter, superimposed on the vortex lattice. This type of order can be static or dynamically fluctuating depending on the level of doping and the magnetic field.

1.3 High Temperature Superconductivity: A Review

1.3.1 Cuprates: CuO2 Layer Based High Temperature Superconductor

Discovery of superconductivity in the ceramic cuprate materials has led to a pursuit to understand this new phenomenon. This new type of superconductivity is considerably different from the "conventional" (i.e, BCS)-type superconductivity and the exact microscopic mechanism is still being debated. However, significant inroads have been made in understanding different aspects of this "unconventional" superconductivity.

A traditional description of electronic behavior in solids is modeled after Drude, Sommerfield, Wiedemann and Franz, where heavier positively charged cores of atoms form a periodic lattice and are immobile and upper valance electrons are almost free as in gas molecules in a jar, aptly named as "free electron gas". This is also the basis for Landau's "Fermi-liquid theory" (FL) where weak short range interactions between electrons are taken into account similar to a normal liquid. The Wiedemann-Franz (WF) law (an empirical observation) is one of the basic properties of a Fermi liquid, reflecting the fact that the ability of a "free electron" to transport

heat is the same as its ability to transport charge and is written as

$$\frac{k}{\sigma T} = \frac{\pi^2}{3}\left(\frac{k_B}{e}\right)^2 = \text{constant} \tag{1.2}$$

where k and σ are the heat/electrical conductivity, respectively. In high-T_c cuprate superconductor $(Pr,Ce)_2CuO_4$, it has been reported that the the WF law is violated in the normal state [16]. The standard theory of electrons, including FL and band theory, is highly successful in explaining metallic, insulating and semiconducting behavior, however fails to account for unconventional superconductivity where electron-electron interaction is too strong. Strong Coloumb repulsion among electrons leads to antiferromagnetic Mott insulating behavior in CuO materials at a composition where "free electron gas" theory predicts a metal (e.g $YBa_2Cu_3O_{6.0}$, This should be a metal but is an AF insulator).

Changes in composition (O doping) leads to many exotic phenomena such as superconductivity, charge ordering, strange metallicity, quantum criticality and Fermi liquid behavior. A Mott insulator is very different from a regular (band) insulator. In a band insulator, lack of conductivity arises due to Pauli exclusion principle as the highest occupied band contains two electrons per site and all the bands are filled. In a Mott insulator, there is one electron per atom and thus the band is exactly half filled. However conduction is blocked by the strong Coulomb repulsion which prevents double occupancy. Typically the ground state is an antiferromagnet (figure 1.8). Doping (hole/electron) restores some electrical conductivity by creating sites to which electrons can jump without having to gain additional Coloumb energy. The resulting motion of the electrons is highly correlated.

High-temperature superconductivity arises in a family of layered copper oxides that all feature weakly coupled square-planar sheets of CuO_2. Structure of one of the member of this family, $YBa_2Cu_3O_{7-\delta}$ (hereafter "YBCO", possibly the most studied) is shown in figure 1.6, as this material was a subject of this research. For $YBa_2Cu_3O_7$, three copper-oxygen layers are stacked along the tetragonal $\hat{\mathbf{c}}$ axis. Two of these layers have oxygen atoms between the copper ions in both the $\hat{\mathbf{a}}$ and $\hat{\mathbf{b}}$ directions, and are called CuO_2 plane layers. The third layer, called the CuO chain layer, has oxygen ions only along the $\hat{\mathbf{b}}$ direction [19]. The phase diagram for YBCO, dependent on oxygen(hole) doping, is shown schematically in figure 1.7. As may be noted from the phase diagram, with increased hole doping, the antiferromagnetic insulating state evolves into a superconducting state. The dependence of critical temperature $T_c(p)$ on doping is given by an empirical relationship [20],

$$T_c(p) = T_{c,\max}\left[1 - 82.6(p - 0.16)^2\right], \tag{1.3}$$

where doping level p varies from 0.05 to 0.27. The proximity of antiferromagnetism and superconductivity gives rise to the conjecture that superconductivity is driven by magnetic interactions

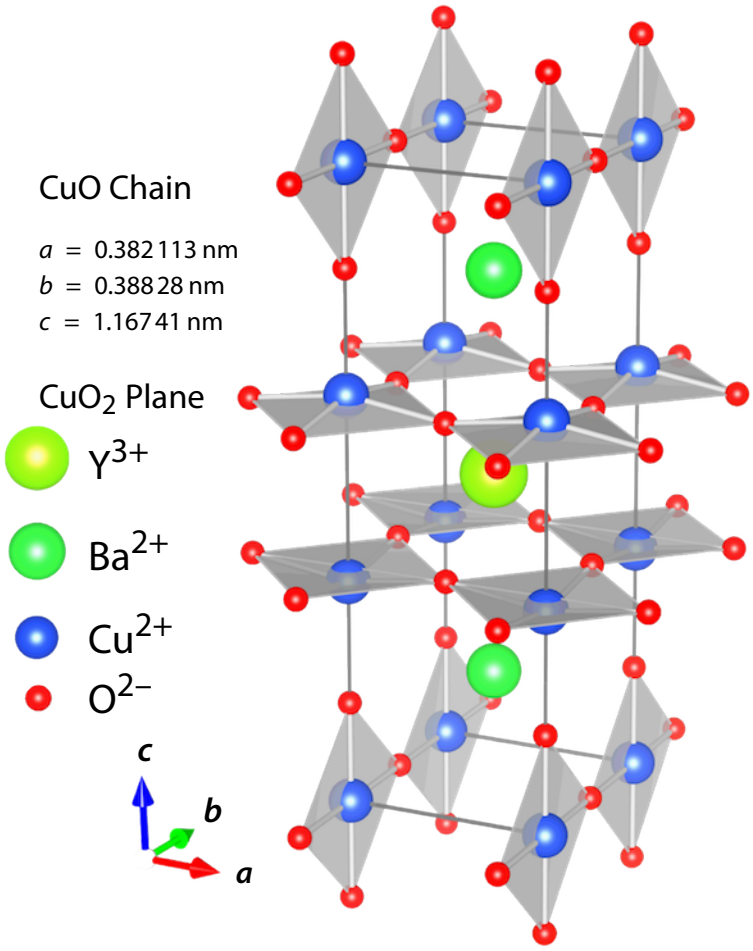

Figure 1.6 : YBCO consists of CuO_2 planes and CuO chains. Each plane layer consists of a single Cu atom sharing with four Oxygen vertices. The CuO chains run parallel to the planes along the *b* direction shown in the figure. Each Cu atom in the chain in the fully oxygenated crystal of $YBa_2Cu_3O_7$ shares two oxygen vertices. Other phases have a reduced number of oxygens in the chain layer. The Yttrium atoms are found between CuO_2 planes, while the Barium atoms are found between CuO_2 planes and CuO chains. Non-stoichiometric compounds have some disorder in the CuO chains. In $YBa_2Cu_3O_{6+x}$, with $x = 0$, the structure is tetragonal and insulating. For $x < 0.35$, CuO chains along *b*-axis start to form and the structure becomes orthorhombic. Maximum $T_c \sim 95$ K occurs for $x \sim 0.92$ [17, 18].

between electrons rather than pairing via phonons. Also it is important to note that, a signature of phonon driven superconductivity, ie, the "isotope effect" has been found to be small [21] in Cuprates. However there has been renewed interest in the possible role of electron-phonon coupling [22--27] in high-T_c superconductivity, although the role is suggested to be indirect [27] and small [24, 28]. A possible mechanism proposed by P. W. Anderson [29] is that "quantum fluctuations" may create instability in the antiferromagnetic order and give rise to a resonating valence bond state [30--32] in which the spins form a "spin-liquid" phase of singlet($s = 0$) pairs. "Spin liquid" is defined to be aggregation of pairs of antiparallel spins. The motion of such singlet pairs is similar to the resonance of π bonds in benzene, and thus is the origin of the

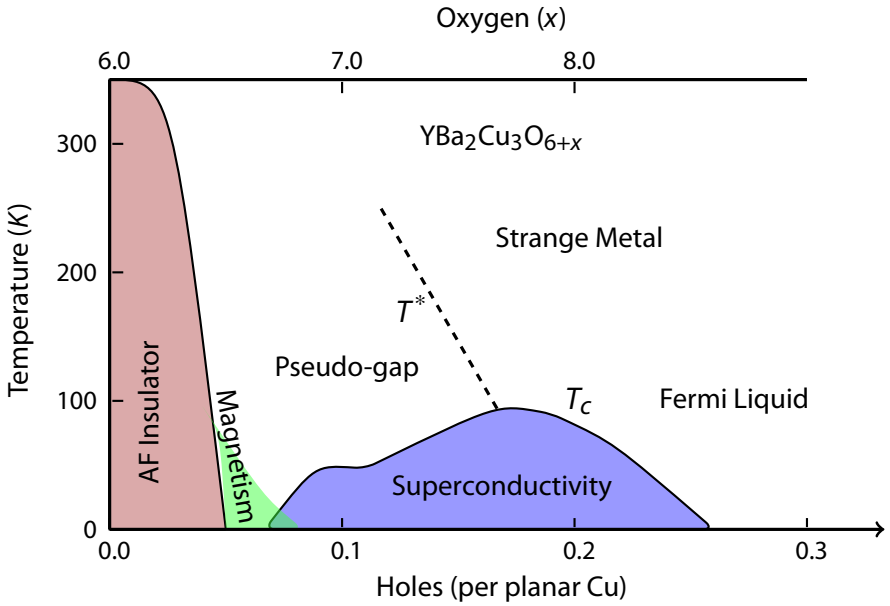

Figure 1.7 : Schematic phase diagram: At very low levels of electron-hole doping, cuprates are insulating and antiferromagnetic (the materials' neighboring spins point in opposite directions). With increased hole doping, YBCO shows disordered magnetism, superconductivity (at temperatures below T_c) and Fermi liquid behavior. At temperatures above T_c but below T^*, YBCO shows a pseudogap phase. The "strange metal" region, above T_c, shows anomalous $\left(\rho(T) \propto T\right)$ temperature dependent electrical resistivity. The boundary of the pseudogap region at low doping levels is unknown. The transition between the Fermi liquid phase and the strange metal phase occurs gradually.

term "resonating valence bond" (RVB), schematically shown in figure 1.8. In this picture, electrons are paired up in antiparallel spin-formation but cannot move due to Coloumb repulsion. Anderson argued, reducing average occupancy, from one, will make these singlet pairs mobile, giving rise to superconductivity. In contrast, YBCO was found out to be an antiferromagnet and not a spin-liquid [33--35]. It has been established that in cuprate systems, antiferromagnetic ordering resides predominantly on the CuO_2 planes [36, 37], with a three-dimensional magnetic transition dictated by weaker coupling between planes.

As seen in the phase diagram in figure 1.7, T_c varies (peaks at "optimal" doping) as a function of doping and is a commonly observed phenomenon in all CuO_2 layer based superconductors [38]. With increased doping 3D antiferromagnetic ordering gives way to a disordered magnetic state with short range correlations [38], thereby retaining some magnetism. At $T > T_c$, metallic behavior is observed for a broad range of dopings and d.c electrical resistance is T-dependent rather that T^2-dependent as would have been expected from a normal metal Fermi liquid behavior. In the overdoped regime, the copper oxides behave more like ordinary metals with a T^2 dependence of d.c resistivity [39]. A naturally overdoped Copper oxide $TlBa_2Cu_3O_{6+x}$ has been observed to show polar angular magnetoresistance oscillations [40, 41], in high mag-

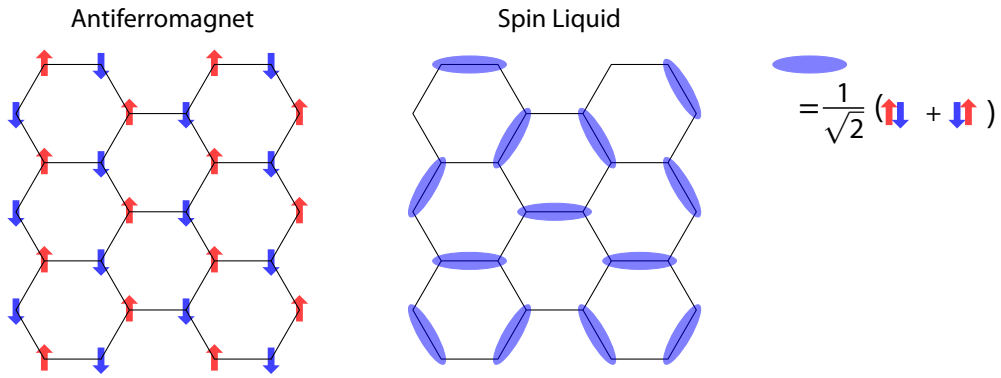

Figure 1.8 : Left: In the antiferromagnetic state, spins on alternating sites are antiparallel and the net spin magnetization is zero. Right: an example of a short range "resonating valence bond" (an aggregation of antiparallel neighboring spins). An oval represents a superposition of different possible spin configurations. This is a "spin-liquid" since there is no static order but their motions are highly correlated. Motions of singlet pairs are hindered due to Coloumb repulsion. Reducing average occupancy from one may make these singlet pairs mobile.

netic fields, establishing the existence of a 3D Fermi surface, consistent with the prediction from band theory, i.e, as in a conventional metal. In underdoped regime, copper oxides have been found to show quantum oscillations [42], an indication of metallic behavior, in de Haas-van Alphen spectra. As may be noted in the phase diagram, Cu-O based superconductors includes a "pseudogap" region [43, 44], a precursor to the superconducting state. It has been shown that this phase originates in CuO_2 planes and not in the CuO chains [45]. Whether this is a distinct state of matter is still under debate [46]. It is metallic, however some parts of the Fermi surface show gaps [43, 44, 47]. A quantum critical point (QCP) [48--50] in the cuprates is speculated to be the end point of a line (T^*) [51] that separates the pseudogap and "strange metal" regions. It has also been speculated that the phase diagram is controlled by such a quantum critical point [52, 53]. A QCP develops in a material at zero temperature when a new form of order emerges from it's ground state as function of some external parameter such as pressure, doping or electric field etc. The quantum critical points are of great interest because of their ability to influence the finite temperature properties of materials. The "normal" region ("strange metal") above the transition temperature T_c has very unusual properties [54--56] (thermal conductivity $k(T)$, optical conductivity $\sigma(\omega)$, the nuclear relaxation rate $T_1^{-1}(T)$), with a large temperature-dependent resistivity implying a scattering rate linear in T [57, 58].

Although there are significant differences compared to conventional superconductivity, supercurrents are still carried by electron pairs, as shown by quantization of magnetic flux in units of $\frac{h}{2e}$ [59--61]. Most of the physical properties of the CuO_2 superconductor have experimentally been established with a high degree of reliability and advances in preparing the materials are such that spurious effects and uncertainties in materials compositions, homogeneities and impurity content may be eliminated as hindrance to the understanding of the phenomenon of high-T_c superconductivity. In spite of substantial efforts, both experimental and theoretical, there remain

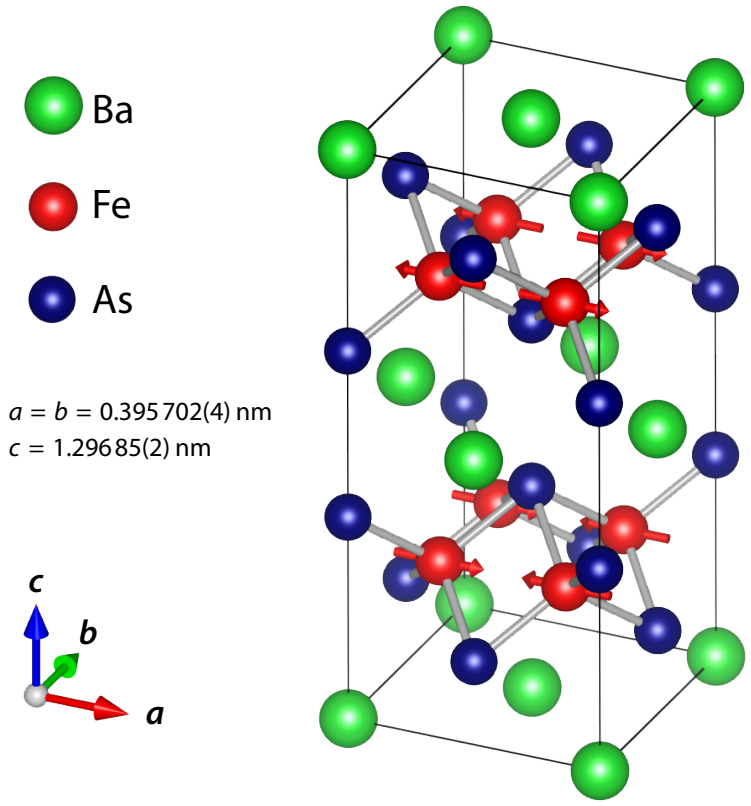

Figure 1.9 : Pnictide crystal structure [69] shows the antiferromagnetic alignment and magnetic moment (red arrows) both along the longer *a* axis in the FeAs plane of the parent compound $BaFe_2As_2$. The magnetic unit cell is the same as the orthorhombic chemical unit cell. It is widely believed that superconductivity originates in the FeAs plane. Although this parent compound $BaFe_2As_2$ is antiferromagnetic, another pnictide parent compound LaOFeAs reportedly shows spin-density-wave (SDW) [70] type magnetic order.

many open questions regarding the underlying microscopic mechanism for high-T_c superconductivity.

1.3.2 Pnictide: A New Type of High Temperature Superconductor

The antagonistic relationship between superconductivity and magnetism has led researchers to avoid using magnetic elements (eg. Fe), as potential building blocks of new superconducting materials. The recent (2008) discovery of superconductivity at T_c's up to 55 K in iron pnictide systems [62--66] has sparked enormous interest in this new class of materials. Even more surprising is that pnictides are the only class of material other than cuprates (CuO_2 layer based superconductors) to have a T_c higher than 40 K (~BCS theoretical maximum). The crystal structure of the parent compound (of the so called 122 system) $BaFe_2As_2$ is shown in the figure 1.9. Co-doped pnictide ($Ba(Co_{0.074}Fe_{0.926})_2As_2$) (grown using self-flux methods [67, 68]) is a subject of this work.

Cuprates and pnictides show similar behavior, such as (i) both are layered structures, (ii) in both cases, the parent (non-superconducting) compounds are antiferromagnets (iii) both mate-

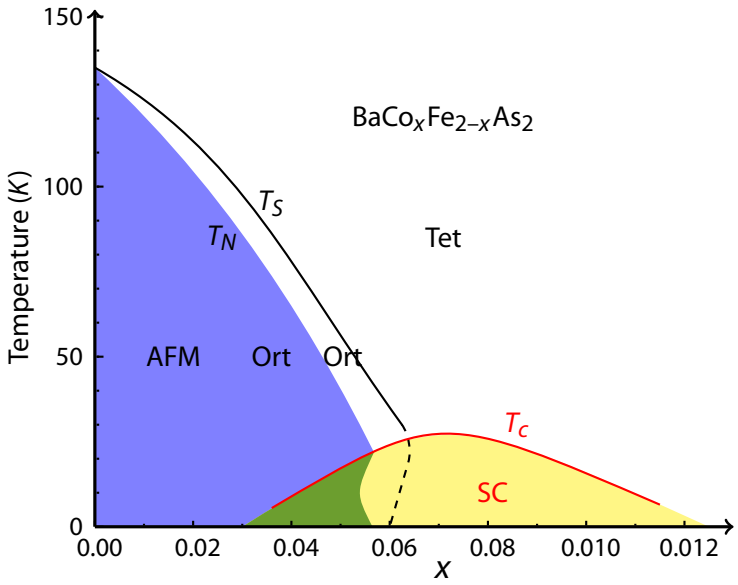

Figure 1.10 : Phase diagram [81, 82] for $BaCo_xFe_{2-x}As_2$. Yellow indicates the superconducting phase, which appears below the superconducting transition temperature T_c. A structural transition occurs at T_s from the tetragonal phase (Tet) at higher temperature to the orthorhombic phase (Ort). Blue represents the antiferromagnetic order (AFM), which appears at T_N, slightly below T_s. The stripes of enhanced superfluid density are observed only in the regime $0.04 < x < 0.06$.

rials show superconducting order upon doping. There are also striking dissimilarities (i) parent compound for cuprates are Mott insulators while for pnictides, they are semimetals, (ii) cuprates have a single band crossing the Fermi surface while iron pnictides have multiple bands at the Fermi energy, (iii) the superconducting gap order parameter has $d_{x^2-y^2}$-symmetry in cuprates whereas for pnictides, the strong contender is an "extended s-wave", also called $s\pm$-symmetry.

Two of the families (parent materials) of pnictides originate from RFeAsO [65] (R=rare earth, abbreviated as 1111 for its 1:1:1:1 ratio of the four elements) and AFe_2As_2 [71] (A=alkaline,the 122 compounds) earth metal, which are tetragonal at room temperature but undergo an orthorhombic distortion in the range 100 K to 200 K that is associated with the onset of antiferromagnetic order [69, 70, 72--75]. Tuning the system via element substitution [76, 77] or oxygen deficiency [78, 79] suppresses the magnetic order and structural distortion, in favor of superconductivity with T_c up to 55 K, with an overall behavior strikingly similar to the high-T_c copper oxide family of superconductors. However, the induced superconductivity by Co doping or other transition metals into the Fe site indicates that atomic disorder in the superconducting Fe layer ostensibly does not suppress superconductivity, contrary to the behaviors of layered cuprate high-T_c superconductors where doping onto the Cu sublattice is always detrimental [80] to T_c.

A preliminary phase diagram [81, 82] of pnictide superconductors is shown in the figure 1.10. It may be noted that the parent compound of the superconducting iron arsenides exhibits a spin density wave (SDW)-type magnetic ordering at low temperatures [70, 83]. It appears that in high-T_c superconductivity, AF order needs to be suppressed before superconductivity may ap-

pear. This has led many to the propose that dynamic AF fluctuations rather than static antiferromagnetism is favorable for high-T_c superconductivity. A recent neutron-scattering experiment found that, in $BaFe_{1.85}Co_{0.15}As_2$, the AF fluctuations are as strong as that in $YBa_2Cu_3O_{6+x}$ [84] and electron-phonon coupling is not the primary driver of superconductivity in pnictides, as in the case of cuprate.The origin of antiferromagnetic ordering in the pnictide parent compounds is a hotly debated topic, largely owing to its implications for the pairing mechanism: the electronic structure suggests that the same magnetic interactions that drives the AFM ordering also produces the pairing interaction for superconductivity [85]. Regardless of the exact nature of magnetic order, it is believed that magnetostructural coupling is prevalent throughout the Fe-based superconductors in the form of coupled magnetic and structural transitions [86, 87]. The presence of both superconductivity and AF spin fluctuations has led to suggestions that quantum criticality may play an important role [88--90], however, prominence of quantum critical behavior in iron pnictides is disputed elsewhere [91]. Due to the large number of pnictides and the nature of chemical substitution, one limitation so far is that many experiments have been carried out on different systems or different chemical compositions of the same crystalline system, which makes comparisons difficult. However their generic features enable general conclusions to be drawn from several experiments. For instance, NMR Knight shift measurements indicate that the superconducting state has a singlet spin symmetry [92--94], suggesting an even order parameter symmetry (eg. *s* wave, *d* wave).

1.4 Pairing Symmetry and Magnetic Penetration Depth Measurement

One fundamental quantity in any superconductors is the London penetration depth λ, which is closely related to superfluid density ($\rho_s \equiv \frac{1}{\lambda^2} \propto \frac{n_s}{m^*}$). In general, the penetration depth λ is given as a function of the superfluid density n_s, effective mass m^*, Ginzburg-Landau coherence length ξ and the mean free path l as [95]

$$\frac{1}{\lambda^2} = \frac{4\pi n_s e^2}{m^* c^2} \times \frac{1}{1 + \xi/l} \tag{1.4}$$

In the clean limit, $\frac{\xi}{l} \to 0$ and the second term in (1.4) becomes unity. In this case, the variation in λ as a function of temperature, doping and orientation are of central importance in testing microscopic theories of exotic superconductors. For example, the linear variation of $1/\lambda^2$ with respect to temperature was a key finding confirming the d-wave nature of the pairing in $YBa_2Cu_3O_{6+x}$ [96, 97]. Also, early μSR studies of the vortex phase in polycrystalline samples found a linear correlation between $1/\lambda^2$ and T_c in the under-doped region [98, 99]. The resulting Uemura plot has played a prominent role in theoretical efforts to understand high T_c superconductivity [100]. Departure from Uemura scaling and the decline of the slope as the $T_c = 0$ quantum critical point is approached can be understood in terms of a 3D-QCP model [101]. Scaling of T_c with $n_s(0)$ in underdoped cuprates may also be due to quantum fluctuations near a 2D quantum critical

point [102].

It is widely believed that cuprate high-T_c superconductivity originates in the two dimensional CuO_2 layers [35, 36, 103]. $YBa_2Cu_3O_{6+x}$ also has one dimensional (1D) CuO chains which may contribute to superconductivity, the mechanism for which is not fully understood [104]. However, it is clear that CuO chains act as a quasi-1D system and charge reservoir [19]. Due to differences in band structures between planes and chains [105], one natural explanation for the same transition temperature is the proximity effect [106--108] whereby electron hopping between chains and planes contribute to superfluidity along chain direction. The 1D chain induces, $a-b$ anisotropy which has been observed in dc resistivity [109, 110] and optical conductivity and penetration depth measurements [111, 112].

In this simple model of multiband superconductivity in $YBa_2Cu_3O_{7-\delta}$, there is an intrinsic pairing interaction in the plane, but the chains are intrinsically normal, which means that the superconducting order parameter is nonzero in the plane layer only [106]. The pairing mechanism of $YBa_2Cu_3O_{6+x}$ is thought to be predominantly d-wave type. Other possible pairing states involving complicated gap functions, have been suggested [113--116]. The pairing symmetry in the recently discovered $BaFe_2As_2$ family of superconductor is still unclear. An accurate determination of $\lambda(T)$ is one way to probe the symmetry of the pairing state. It has been theorized [117] that only the temperature dependence of $\lambda(T)$ at very low T is sensitive to pairing state of the superconductor. It is clear that accurate measurements of λ and $a-b$ anisotropy are essential in clarifying central questions in $YBa_2Cu_3O_{6+x}$.

Unfortunately, accurate measurements of λ are difficult due to many possible systematic uncertainties. For example, in any bulk measurement the assumption of an exponential decay of the field in the Meissner state is only valid in the local London limit of a perfect surface [118]. Significant non-local effects are expected if the coherence length is comparable to the penetration depth [119] or if there are nodes in the superconducting gap function [120]. Even within the London limit, there may be a non-exponential decay of the field, arising from any depth dependent change in the magnitude or symmetry of the order parameter. These add uncertainty to all conventional bulk measurements where the field profile is assumed and not measured. Alternatively, one can determine the absolute value of λ from μSR studies in the vortex state where the muon acts as a sensitive probe of the local magnetic field distribution. However, an accurate determination of λ requires there to be a well ordered vortex lattice with known symmetry. Also, there are substantial non-local and non-linear effects associated with vortices which complicate the theory and make it difficult to extract the true λ [120--123]. One approach is to fit the observed field distribution to a simple Ginzburg-Landau model involving an effective λ and then to extrapolate to zero magnetic field (or vortex density) [124]. Until now, the penetration depth has been measured in the vortex state via muon spin rotation [125] and using microwave techniques [96, 126--128] and using tunnel diode resonator method. In vortex state measurement, Sonier *et al.* used a GL model for magnetic field distribution to extract λ as a function of applied

magnetic field. However, it was mentioned that λ_{ab} measured is an effective penetration depth which is model dependent. Consequently, one may expect some difference in λ measured in the Meissner state where there are no vortices. The microwave techniques used in [96, 126--128] reported London penetration depth for a number of high-T_c superconductors. Microwave techniques are well-suited to measuring temperature dependence of λ but generally not very sensitive to the absolute value of λ. This is also true for the TDR method - which is closely related to the microwave techniques.

In this thesis, we present measurements of the London penetration depth in detwinned crystals of YBCO for three oxygen dopings and a Co doped FE-PNICTIDE using low energy μSR. The field profiles are obtained directly by measuring the muon frequency spectrum - which contains most of the relevant information about muons' interaction with the local magnetic environment.

The thesis is organized as follows: chapter 2 briefly discusses BCS pairing, London model and order parameter symmetry; chapter 3 discusses low energy μSR technique, stopping distribution of muons and Fourier analysis of asymmetry spectra; chapter 4 contains all the results and discussion followed by summary in chapter 5.

CHAPTER 2 THEORY

2.1 BCS Theory

The basic idea behind the BCS superconductivity is that an attractive interaction between electrons, regardless of their strength, can bind the electrons into pairs [10]. We consider a case for only two electrons added to the Fermi sea. The first electron attracts positive ions and these ions, in turn, attract the second electron giving rise to an effective attractive interaction between electrons. Since the lattice distortion can be expressed in terms of phonons, the interaction between electrons is said to be phonon mediated. The total energy of the electron system is minimized when there are Cooper pairs compared to a Fermi gas with no such pairing. The center of mass of a Cooper pair is zero since the electrons have opposite momenta and spin $|\hbar\boldsymbol{k}, \uparrow\rangle$ and $|-\hbar\boldsymbol{k}, \downarrow\rangle$. Due to this opposite momenta and spin, it is labelled s-wave pairing since the relative angular momenta of the two electrons is zero. The electron-phonon system is described by the single complex order parameter ψ. A schematic of "in-phase" motion of the system is shown in the figure 2.1.

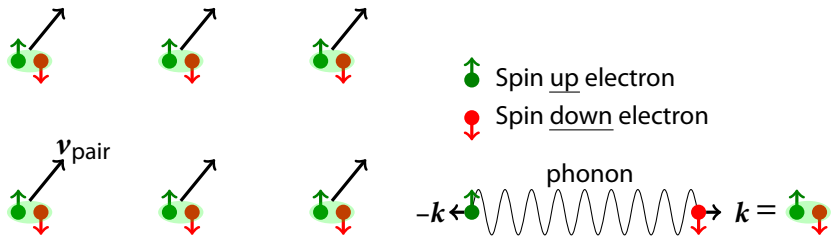

Figure 2.1 : In the superconducting state, electrons pair up in zero-spin composites. They all move "in phase" and are said to be "coherent". This is considered to be a ordered state and the whole electron-phonon system may be described by a single wavefunction.

One important consequence of the BCS theory is the presence of a momentum dependent energy gap $\Delta(\boldsymbol{k})$ at the Fermi surface so that an amount of $2\Delta(\boldsymbol{k}, T)$ energy is required to create an excitation which loosely amount to breaking up a Cooper pair and removing it from the ground state. The energy gap is schematically shown in the figure 2.2. The gap is opened at the Fermi energy as the temperature is lowered below the critical temperature. A d-wave density of states is also shown in the figure 2.2. Unlike s-wave superconductors, some states are always available at the Fermi surface or where it was prior to the transition to superconductivity.

In the weak coupling limit, the gap $\Delta(0)$ is much smaller than the characteristic phonon energy $\hbar\omega_D$,

$$\frac{2\Delta(0)}{k_B T_c} = 3.52. \tag{2.1}$$

The numerical factor 3.52 is well tested in experiments and found to be reasonable, in the weak

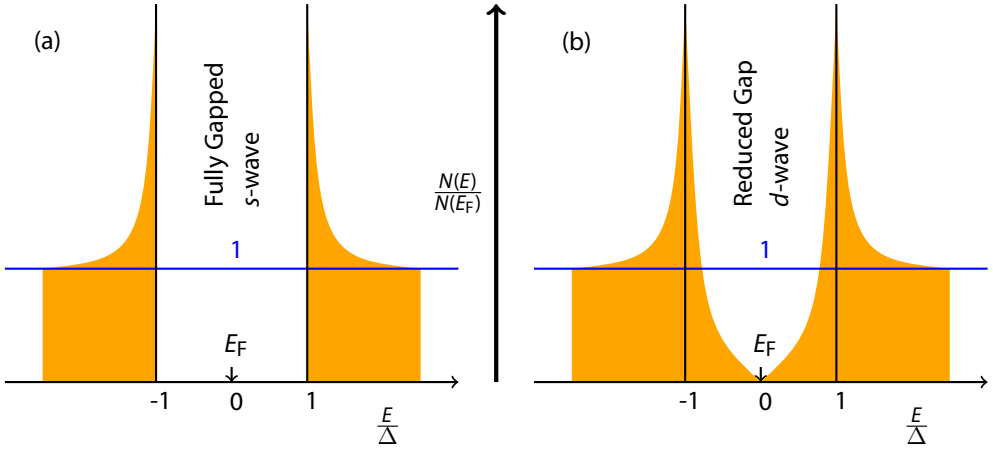

Figure 2.2 : (a), *s*-wave: Density of states in a conventional superconductor such as Nb. Note there is a region near E_F where there are no available states and that excitations require a finite amount of energy given by the gap. This region comprises the superconducting energy gap. On either side of this gap there are singular peaks in the density of states. (b), *d*-wave: Density of states in a high-T_c superconductor like YBCO. The density of states is reduced at the Fermi surface, however there is no true energy gap since there are certain directions in k space (the so called nodes) where it is possible to create an excitation with an arbitrarily small energy.

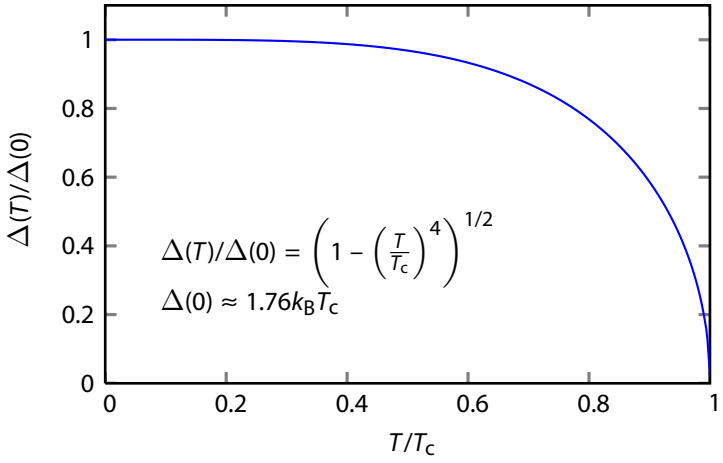

Figure 2.3 : Temperature dependence of the superconducting energy gap in the weak coupling limit of BCS interaction. The superfluid density $\Delta(T) \propto n_s^{1/2}$ in a two-fluid model [129] implies the (T/T_c) dependence of energy gap. This gap model is also experimentally verified [130].

coupling limit. $\Delta(T)$ remains fairly constant until the thermal energy becomes enough to excite quasiparticles, at low temperature. As will be shown shortly, the superfluid density depends on effective penetration depth as

$$n_s \left(\sim \Delta^2(T)\right) = \lambda^{-2} \frac{mc^2}{4\pi e^2} \tag{2.2}$$

Inserting the empirical approximation,

$$\lambda^{-2} \propto (1-t)^4 \quad \left(\text{where } t \equiv \frac{T}{T_c}\right) \tag{2.3}$$

into (2.2)

$$\begin{aligned} n_s\left(\sim \Delta^2(T)\right) &= 1 - t^4 \\ &= (1-t)(1+t)(1+t^2) \\ \Rightarrow \Delta^2(T) &\approx 4(1-t) \quad (\text{at } T \sim T_c) \\ \Delta(T) &\sim (1-t)^{1/2} \end{aligned} \tag{2.4}$$

Near the transition temperature T_c, a more accurate form of $\Delta(T)$ may be given as

$$\frac{\Delta(T)}{\Delta(0)} \sim 1.74\left(1 - \frac{T}{T_c}\right)^{\frac{1}{2}}, \qquad T \sim T_c. \tag{2.5}$$

This is shown graphically in the figure 2.3.

The most important manifestation of the electron-phonon interaction is the superconducting state itself. According to our present understanding of Cooper pairing, the electron-phonon induced attraction between two electrons would not overcome their direct Coulomb repulsion, except for the fact that the former is retarded (where the second electron interacts with the lattice distortion after some time the first electron leaves that location), whereas the latter is not.

2.2 London Penetration Depth

We consider the penetration depth in the Meissner state of a type II superconductor. Below H_{c1}, the London equations provide a good description of the electromagnetic properties. According to Maxwell's equations,

$$\vec{\nabla} \times \vec{E} = -\frac{1}{c}\frac{\partial \vec{B}}{\partial t}. \tag{2.6}$$

In the classical Drude model of electrical conductivity, we have

$$\vec{F} = -m\frac{\vec{v}}{\tau} - e\vec{E} = m\frac{d\vec{v}}{dt}, \tag{2.7}$$

where $\vec{v}$ is the average drift velocity of the electrons, m is the mass of an electron, $\vec{E}$ is the electric field the electrons are in and τ is the relaxation time, i.e, roughly the time required to bring the drift velocity to zero if the electric field was suddenly set to zero. In a normal metal, the competition between the scattering and the acceleration in (2.7) leads to a steady state average (or drift) velocity

$$\vec{v} = \frac{e\vec{E}\tau}{m}. \tag{2.8}$$

Assuming n conduction electrons per unit volume, we get the electric current density via Ohm's Law,

$$\vec{J} = ne\vec{v} = \left(\frac{ne^2\tau}{m}\right)\vec{E} = \sigma\vec{E}. \tag{2.9}$$

To describe superconductivity, London assumed that a certain fraction of electron density n_s experience no relaxation i.e., letting τ_s in (2.7) go to infinity. This leads to

$$\frac{d\vec{J}_s}{dt} = \left(\frac{n_s e^2}{m}\right)\vec{E}, \tag{2.10}$$

where n_s is density of the superconducting carriers. Taking curl on both side of the (2.10), we get

$$\frac{m}{n_s e^2}\left(\vec{\nabla}\times\frac{d\vec{J}_s}{dt}\right) = \vec{\nabla}\times\vec{E}. \tag{2.11}$$

Substituting Maxwell's equation (2.6) into (2.11), we obtain the second London equation

$$\frac{mc}{n_s e^2}\left(\vec{\nabla}\times\frac{d\vec{J}_s}{dt}\right) + \frac{d\vec{B}}{dt} = 0. \tag{2.12}$$

London postulated

$$\frac{mc}{n_s e^2}\left(\vec{\nabla}\times\vec{J}_s\right) + \vec{B} = 0, \tag{2.13}$$

which is consistent with (2.12). Assuming no time varying electric field, another of Maxwell's equations connects $\vec{J}_s$ with $\vec{B}$

$$\vec{J}_s = \frac{c}{4\pi}\left(\vec{\nabla}\times\vec{B}\right). \tag{2.14}$$

Substituting (2.14) into (2.13), we get

$$\begin{aligned}\lambda^2\left(\vec{\nabla}\times\vec{\nabla}\times\vec{B}\right) + \vec{B} &= 0,\\ \lambda^2\nabla^2\vec{B} + \vec{B} &= 0,\end{aligned} \tag{2.15}$$

where

$$\frac{1}{\lambda^2} = \frac{4\pi n_s e^2}{mc^2}. \tag{2.16}$$

In a vacuum-superconductor interface (which is also the case in our experiment), the solution of (2.15) is given by

$$B(x) = B_0\exp\left(-\frac{x}{\lambda}\right) \tag{2.17}$$

where B_0 is the magnitude of the external applied field. The quantity λ is known as the London penetration depth. The most important success of the London equations (2.14) and (2.15) is that a static magnetic field is screened from the interior of a bulk superconductor over a characteristic penetration depth λ. A simple estimate shows that this distance is mesoscopic and much larger

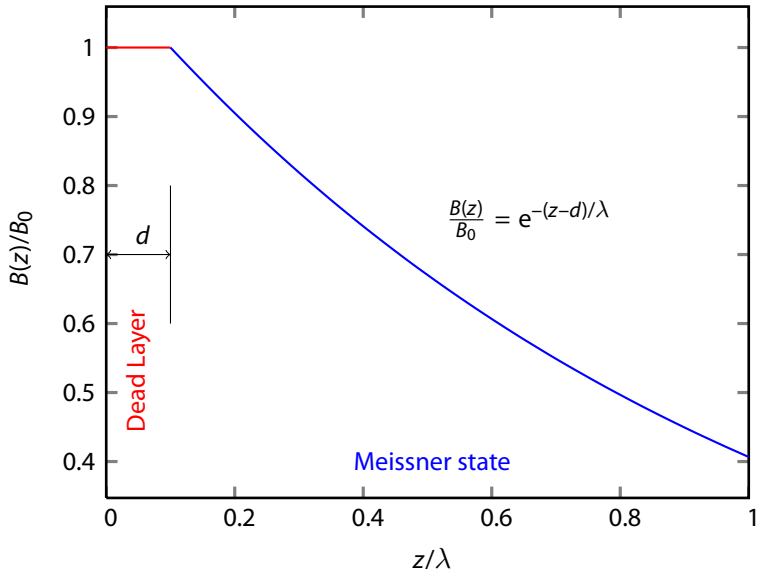

Figure 2.4 : External magnetic field drops exponentially ((2.18)) as it enters a superconductor in Meissner state. The characteristic distance λ is called the London penetration depth. Close to the surface, a reduction of superfluid density has been observed (cf. figure 4.23). With all of our experimental observations for energies ($E \geq 2$ keV i.e. average muon stopping depth $\langle z_\mu > 12\,\text{nm}\rangle$), a simple model of the presence of normal state close to the surface suffices to fit the data.

than the mean distance r between electrons in the superconductor. As $T \to T_c$ from below, $n_s \to 0$ continuously and as a consequence, $\lambda(T)$ diverges according to (2.16). While (2.17) may be valid for a superconductor with an atomically flat surface, a real surface where the translations symmetry is broken and is non-flat might give rise to a suppressed order parameter for several nanometers and a modified London model (figure 2.4)

$$B(z) = \begin{cases} B_0 \exp\left(-\dfrac{z-d}{\lambda_{a/b}}\right) & \text{if } z \geq d \\ B_0 & \text{if } z < d \end{cases} \tag{2.18}$$

may be more appropriate. Here B_0 is the magnitude of the applied field, $\lambda_{a/b}$ is the magnetic penetration depth in the a or b direction, respectively, z is the depth into the crystal, and d is an effective dead layer inside of which the supercurrent density is suppressed. Naively one might expect d to be the coherence length since the order parameter must be zero at the surface. However there are many other effects that might contribute to a d larger than the coherence length as will be discussed later.

2.3 Pairing Mechanism and Order Parameter Symmetry

The critical temperature T_c is the onset of long-range, macroscopic phase coherence in the Cooper pairs. Long range correlations between pairs are described by off-diagonal long-range order (ODLRO) [131, 132], with no classical analog, which implies non-zero value of the pair correla-

tion function

$$\begin{aligned}\rho(\vec{r},\vec{r}') &= \left\langle \psi_{\downarrow}^{\dagger}(\vec{r})\psi_{\uparrow}^{\dagger}(\vec{r})\psi_{\downarrow}(\vec{r}')\psi_{\uparrow}(\vec{r}') \right\rangle \\ &= \left\langle \psi_{\downarrow}^{\dagger}(\vec{r})\psi_{\uparrow}^{\dagger}(\vec{r}) \right\rangle \left\langle \psi_{\downarrow}(\vec{r}')\psi_{\uparrow}(\vec{r}') \right\rangle \end{aligned} \tag{2.19}$$

in the limit the pair separation $|\vec{r} - \vec{r}'|$ is infinite. Here, $\psi_{\uparrow}^{\dagger}(\vec{r})$ and $\psi_{\uparrow}(\vec{r})$ are the particle field operators[1] for creation and annihilation at a coordinate $\vec{r}$, with momentum $\vec{k}$ and spin $\uparrow$. From the finite value of the pair correlation function ((2.19)), the local pair amplitude $\left\langle \psi_{\downarrow}^{\dagger}(\vec{r})\psi_{\uparrow}^{\dagger}(\vec{r}) \right\rangle$ must be non-zero, which is, in essence the amplitude squared of the GL order parameter, $|\psi(\vec{r})|^2 \propto n_s$, the superfluid density. It's important to note that, although n_s is a "local pair" amplitude, pairings are non-local, ie, partners of a single pair are in macroscopic distance. Given macroscopic ODLRO, it's possible to derive the Meissner effect [131, 133] and flux quantization [131]. It is thought that ODLRO is a property not only of BCS superconductors but also of high-T_c superconductivity [133, 134], including the recently discovered Pnictide superconductors [135].

As in any appearance of order, superconducting order lowers the symmetry of the system. In case of a 2nd order, continuous, superconducting transition, the order parameter is a measure of the "amount" of symmetry breaking in the ordered state. The symmetry group H describing the superconducting state is generally a subgroup of the normal state symmetry group G:

$$G = X \times R \times U(1) \times T \quad \text{for } T > T_c \tag{2.20}$$

and

$$H \subset G \quad \text{for } T < T_c \tag{2.21}$$

where X is the symmetry group of the crystal lattice, R the symmetry group of spin rotation, $U(1)$ the one dimensional global gauge symmetry, and T the time reversal symmetry operation. Nearly all group-theoretic classifications of superconducting states are based on point-group symmetry. Point-group symmetry classification of pair states has been extensively studied in cuprate superconductors [136--138].

Order parameter symmetry can give insight into the mechanism/nature of the pair condensate and limit the possible interactions that are possible. Crystal structures that have mirror symmetry (eg, CuO_2 layer based superconductors) can be described by parity of the pair state. It has been argued that the complex phase diagram of high-T_c superconductors can be deduced from a symmetry principle that unifies antiferromagnetism and superconductivity [139].

The superconducting energy gap $\Delta(\vec{k}, T)$ for s-wave superconductors, is believed to be symmetric in momentum space (figure 2.6a). One other very important pairing symmetry is of

[1] $\psi_{\uparrow}(\vec{r}) = \left\langle \psi \mid \psi_{\uparrow}(\vec{r}) \mid \psi \right\rangle$ is the real space representation, where $|\psi\rangle$ is the ground state wavefunction.

$d_{x^2-y^2}$-wave where the energy gap is thought to be of the form

$$\begin{aligned}\Delta(\vec{k}_F, T) &= \Delta_0 g(T)(\cos k_x - \cos k_y) \\ &\approxeq \frac{\Delta_0}{2} g(T)(k_x^2 - k_y^2), \text{ for } (k_x, k_y) \text{ close to the nodes,}\end{aligned} \tag{2.22}$$

where momentum $\vec{k}_F$ is measured from the Fermi surface. It may be noted that for $|\hat{k}_x| = |\hat{k}_y|$, the gap is zero (figure 2.6b) meaning thermal excitations can be created with an arbitrarily small energy, implying there is significant T dependence in the superfluid density even at very low T. The temperature and angular dependence of the energy gap function, $\Delta_d(\phi, T)$, may be obtained by integrating over momentum:

$$\Delta_d(\phi, T) = \Delta_{0,d}\, g_d(T) \int_{k=0}^{k_{\max}} (\cos(\cos k\phi) - \cos(\sin k\phi))\, \mathrm{d}k \tag{2.23a}$$

$$\equiv \Delta_{0,d}\, g_d(T)\, g_d(\phi) \tag{2.23b}$$

$$\propto \Delta_{0,d}\, g_d(T) \cos(2\phi) \tag{2.23c}$$

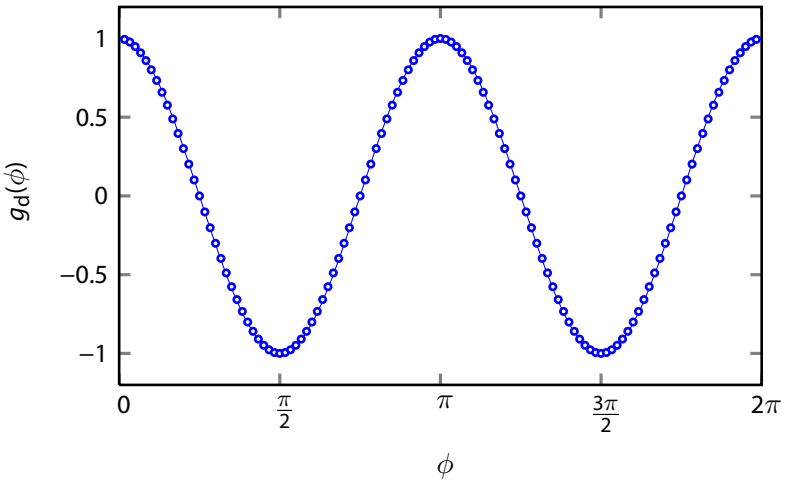

Figure 2.5 : Angular dependence of a $d_{x^2-y^2}$-wave gap.

High-T_c superconductors such as YBCO are believed to be primarily of $d_{x^2-y^2}$-wave character [140--142]. Establishment of predominantly d-wave order in T_c materials, over a wide range of doping and temperature ranges implies that d-wave symmetry is a feature of the cuprates. This also suggests that d-wave pairing in cuprates has a common origin. The newly discovered family of Fe based superconductors may have $s_{\pm}$ (figure 2.6c) symmetry in the order parameter from band structure calculations [85, 144]. Although a superconducting mechanism isn't determined by the order parameter, the pairing Hamiltonian must obey the point-group symmetry of the gap function $\Delta(\vec{k})$.

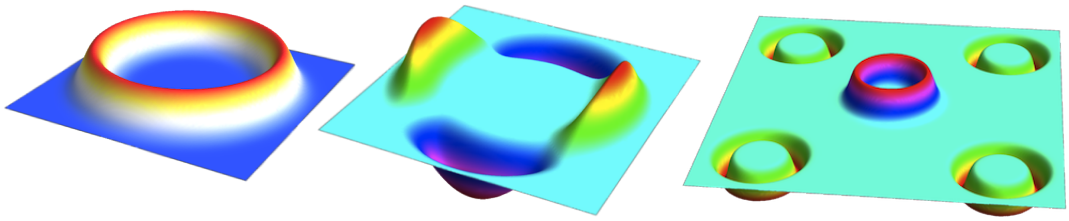

Figure 2.6 : A schematic 2D representation of the superconducting order parameter $\Delta(\boldsymbol{k})$ (where energy gap = $|\Delta(\boldsymbol{k})|$) in different cases:(a) a conventional, *s* wave superconductor (eg. Nb); (b) a *d* wave, as is the case in copper oxides; (c) an $s_{\pm}$ wave, as is thought to be the case in iron-based superconductors. In (a) and (b), the two-dimensional Fermi surface is approximated by one circle. In (c), the Fermi surface is approximated by a small circle in the center (the first band) surrounded by four larger circles (to comply with the tetragonal symmetry [143]; the second band). In all cases, the height of the "rubber sheet" is proportional to the magnitude of the order parameter (including its sign).

2.4 Critical Temperature and Bose Einstein Condensation

In a conventional superconductor, the formation of Cooper pairs[2] and that coherence set in at the same temperature. In cuprates, there is some evidence that Cooper pairs form above the critical temperature and that T_c represents the temperature where phase coherence (LRODO) sets in. This is similar to Bose-Einstein condensation (BEC). A simple model for a superconductor in this limit is to assume a gas of non-interacting bosons, which are Cooper pairs. The bosons are assumed to be confined to a box of volume $V\ \left(=L^3\right)$. The time-independent Schrodinger equation in such a case,

$$-\frac{\hbar^2}{2m}\nabla^2\psi(\boldsymbol{r}) = E\psi(\boldsymbol{r}) \tag{2.24}$$

may be solved with periodic boundary conditions of

$$\psi(x+L,y,z) = \psi(x,y+L,z) = \psi(x,y,z+L) = \psi(x,y,z) \tag{2.25}$$

yielding

$$k_{x,y,z} = \left(\frac{2\pi}{L}\right) n_{x,y,z} \tag{2.26}$$

and

$$E(\boldsymbol{k}) = \frac{\hbar^2 k^2}{2m} = \frac{\hbar^2}{2m}\left(\frac{2\pi}{L}\right)^2\left(n_x^2+n_y^2+n_z^2\right), \tag{2.27}$$

where n_x, n_y, n_z are non-negative integers. In other words, allowed $\boldsymbol{k}$- wave vectors form a simple cubic lattice with a lattice constant $2\pi/L$. Therefore, each state occupies a volume in $\boldsymbol{k}$-space equal

[2]The arguments in this section are largely from Prof. Rob Kiefl and has been included with his permission.

to

$$\Delta \boldsymbol{k} = \left(\frac{2\pi}{L}\right)^3 = \frac{8\pi^3}{V} \tag{2.28}$$

A summation of any smooth function $F(\boldsymbol{k})$ may be written as

$$\sum_{\boldsymbol{k}} F(\boldsymbol{k}) = \frac{V}{8\pi^3} \sum_{\boldsymbol{k}} F(\boldsymbol{k}) \Delta \boldsymbol{k} \tag{2.29a}$$

$$\Rightarrow \lim_{V\to\infty} \frac{1}{V} \sum_{\boldsymbol{k}} F(\boldsymbol{k}) = \frac{1}{8\pi^3} \int \mathrm{d}\boldsymbol{k} F(\boldsymbol{k}) \tag{2.29b}$$

In the independent electron approximation, the Cooper pair density may be written as

$$n = \frac{N}{V} = 2 \sum_{\boldsymbol{k}} f\left(E(\boldsymbol{k})\right) = \frac{1}{4\pi^3} \int \mathrm{d}\boldsymbol{k} f\left(E(\boldsymbol{k})\right) \tag{2.30}$$

using (2.29b), where $f\left(E(\boldsymbol{k})\right)$ is the Bose-Einstein distribution function and the multiplication factor of 2 is due to spin degeneracy of electronic energy level. Changing the integration variable from $\boldsymbol{k}$ to E, (2.30) may be written as

$$n = \int_{k=0}^{\infty} \frac{k^2 \mathrm{d}k}{\pi^2} f\left(E(\boldsymbol{k})\right) = \int_{E=0}^{\infty} \mathrm{d}E g(E) f\left(E\right), \tag{2.31}$$

where the density of states $g(E)$ in three dimensions is given by

$$g(E) = \frac{1}{4\pi^2} \left(\frac{2mE}{\hbar}\right)^{3/2}. \tag{2.32}$$

The first excited state has the energy

$$\Delta \equiv \frac{\hbar^2}{2m} \left(\frac{2\pi}{L}\right)^2. \tag{2.33}$$

In general, $k_B T >> \Delta$ and as such large number of states have non-zero Bose-Einstein distribution function

$$f(E) = \frac{1}{\exp\left(\beta(E-\mu)\right) - 1}, \tag{2.34}$$

where $\beta = k_B T$ and μ is the chemical potential. The number of Cooper pairs may be written as

$$N \approx V \int_0^{\infty} \frac{g(E)}{\exp\left(\beta(E-\mu)\right) - 1} \mathrm{d}E, \tag{2.35}$$

With a change of variable $x = \beta E$, (2.35) may be written as

$$N = \frac{V}{4\pi^2} \left(\frac{2m\beta}{\hbar^2}\right)^{3/2} \int_0^{\infty} \frac{x^{1/2}}{\exp\left(x - \beta\mu\right) - 1} \mathrm{d}x. \tag{2.36}$$

The maximum value of the integral in (2.36) is $1.36\pi^{1/2}$, as $\mu \to 0$. However, an unlimited number of Cooper pair can condense into the ground state. Thus with a suitable choice of chemical potential $\mu \to 0$, the occupation number diverges

$$f(0) = \frac{1}{\exp(\beta(E-\mu))-1} \approx \frac{1}{(1-\beta\mu+\cdots)-1} = \frac{k_B T}{|\mu|}. \tag{2.37}$$

For excited states, $(E-\mu) > \Delta$, no such divergence can occur in $f(E)$. Therefore, the ground state contribution to N is treated separately and the total number of Cooper pairs is written as

$$\begin{aligned} N &= f(0) + \frac{V}{4\pi^2}\left(\frac{2m\beta}{\hbar^2}\right)^{3/2}\int_0^\infty \frac{x^{1/2}}{\exp(x-\beta\mu)-1}\mathrm{d}x \\ &\approx N_0 + 2.612V\left(\frac{mk_\mathrm{B}T}{2\pi\hbar^2}\right)^{3/2} \end{aligned} \tag{2.38}$$

Rearranging and dividing by N, the fraction of particles in the ground state may be written as

$$\frac{N_0}{N} = 1 - \frac{2.612\,V}{N}\left(\frac{mk_\mathrm{B}T}{2\pi\hbar^2}\right)^{3/2} = 1 - \left(\frac{T}{T_\mathrm{BE}}\right)^{3/2}, \tag{2.39}$$

where the Bose-Einstein condensation temperature may be written as

$$T_\mathrm{BE} = \frac{2\pi\hbar^2}{mk_\mathrm{B}}\left(\frac{\rho}{2.612}\right)^{2/3}, \tag{2.40}$$

with $\rho = N/V$ being the density of total number of pairs. Identifying T_BE as the temperature at which pairs start to condense into the ground state, it is indeed the critical temperature T_c. Rewriting (2.40), the superfluid density (N_0/N) may be written as

$$\rho_\mathrm{s}(T) = 1 - \left(\frac{T}{T_\mathrm{c}}\right)^{2/3}. \tag{2.41}$$

When *c*-axis effective carrier mass m_c is different than the *a* – *b*-plane carrier mass *m*: The energy equation (2.27) may be written as

$$E(\boldsymbol{k}) = \frac{\hbar^2k^2}{2m} = \frac{\hbar^2}{2m}\left(\left(\frac{2\pi}{L}\right)^2\left(n_x^2+n_y^2\right) + \left(\frac{2\pi}{L\alpha}\right)^2 n_z^2\right), \tag{2.42}$$

where

$$\alpha = \sqrt{\frac{m_\mathrm{c}}{m}}. \tag{2.43}$$

In essence, the effective mass in all three axis directions may be taken equal to m, with the constant energy surface being an ellipsoid. For such a case, density of states $g(E)$ in (2.31) may be

shown to be

$$g(E) = \frac{\alpha}{4\pi^2}\left(\frac{2mE}{\hbar}\right)^{3/2}. \tag{2.44}$$

Using the same arguments and calculations as before, the fraction of bosons in the ground state may be written as

$$\frac{N_0}{N} = 1 - \frac{2.612\, V\, \alpha}{N}\left(\frac{mk_{\mathrm{B}}T}{2\pi\hbar^2}\right)^{3/2} = 1 - \left(\frac{T}{T_{\mathrm{BE}}}\right)^{3/2}, \tag{2.45}$$

where

$$T_{\mathrm{BE}} = \frac{2\pi\hbar^2}{mk_{\mathrm{B}}}\left(\frac{1}{2.612}\frac{\rho}{\alpha}\right)^{2/3}. \tag{2.46}$$

In the limit, the effective mass ratio $\alpha \to \infty$, $T_{\mathrm{c}} \to 0$ - which is expected as the system becomes two dimensional and the Bose-Einstein critical temperature is zero in such a system. It is also clear that anisotropic effective mass will tend to suppress T_{BE}. It will be seen in section 4.3 that dimensionality of possible BEC interaction may be influential in setting critical temperature, T_{c}, of phase coherence.

CHAPTER 3 EXPERIMENTAL TECHNIQUES

3.1 Introduction To μSR

Muons were discovered in the 1930's and their properties continue to be studied even now. Parity violation in muon decay was discovered by Garwin *et al.* in 1957. Wu *et al.* discovered parity non-conservation in β-decay that same year [145]. The meson factories such as TRIUMF and PSI made μSR experiments much easier in the 1970's. Low energy-μSR was only developed about 15 years ago. μSR/MUSR refers to muon spin Rotation/Relaxation/Resonance techniques which use the anisotropic decay of almost 100 % spin-polarized muons to investigate the local magnetic environment of matter, both in bulk and in thin films. This is very different compared to other magnetic resonance probes such as nuclear magnetic resonance (NMR) and electron spin resonance (ESR) methods which rely on thermal equilibrium spin polarization in a magnetic field to generate polarization and electrical circuits are used to detect the time evolution of polarization. Typically this implies relatively high magnetic fields which are not required in μSR.

When a positive muon decays, it emits a fast decay positron preferentially along the direction of its spin at the time of decay due to the parity violation. From a single decay positron one cannot be certain which direction the muon spin is pointing in the sample. However, by measuring the anisotropic distribution of the decay positrons from a large number of muons, the statistical average direction of the spin polarization of the muon ensemble as a function of time after arrival in the sample can be determined. The time evolution of the muon spin polarization depends on the static and dynamic local magnetic field at the muon site. As such, the muon acts as sensitive probe of the local magnetic environment.

3.1.1 Properties and Production of Muons

Muons are leptons, 207 times more massive than electrons. Muon properties are briefly mentioned in the following table 3.1. Muons are generated from the decay of charged pions ($\pi^{\pm}$), typically produced via energetic collisions of high-energy protons with target nuclei, such as car-

Table 3.1 : Properties of Muon [146]

Mass, m_μ	105.658389(34) MeV/c^2
Lifetime, τ_μ	2.197034(21) μs
Charge, q	$\pm e$
Spin	$\frac{\hbar}{2}$
Magnetic moment	$4.49044786(16)\times10^{-26}$ J/T
Spin g-factor, g_μ	2.0023318414(12)
Gyromagnetic ratio, $\gamma_\mu = g_\mu \mu_\mu / h$	$2\pi \times 135.69682(5)$ MHzT^{-1}

bon or beryllium. The positively charged pions have a mean lifetime of about 26 ns and decay into a muon and muon neutrino (antineutrino)

$$\begin{aligned} \pi^+ &\rightarrow \mu^+ + \nu_\mu \\ \pi^- &\rightarrow \mu^- + \overline{\nu}_\mu \end{aligned} \tag{3.1}$$

and is schematically shown in figure 3.1. The most common source of muons is from positive

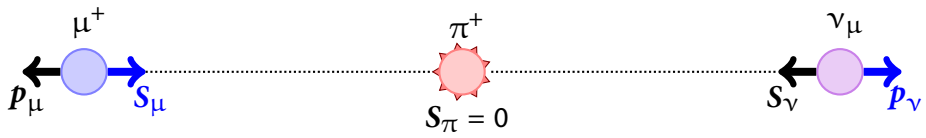

Figure 3.1 : Positively charged pions live for about 26 ns and then decay into a muon and a neutrino. Both the muon and neutrino are 100 % spin-polarized along their momentum direction. The muons carry a kinetic energy of 4.12 MeV in the rest frame of pion. Muons, originating from pions decaying near the surface of the production target, are called "surface muons".

pions those stop near the surface of the production target and decay at rest into a positive muon. The resulting muons have an energy close to 4.1 MeV since they do not lose much energy before escaping from the target. This is called a ``surface'' muon beam. Negative pions, those stopping in the production target, behave as heavy electrons and are captured by the nucleus before they can decay into negative muons. Positive pions occupy interstitial positions in the target material and subsequently decay into a positive muon and a neutrino with a lifetime equal to that in free space. Therefore, positive muons are most commonly used to investigate local magnetic environments in materials. Because of the parity violating nature of weak beta-decay, the positron in a μ^+ decay is correlated with direction of muon spin at the time of decay. The time evolution of the ensemble average polarization may be determined from the decay pattern measured from a large ensemble of muons. The probability per unit time, that the positron is emitted in decaying at an angle θ with respect to the μ^+ spin polarization is given by

$$\frac{\mathrm{dW}(\epsilon,\theta)}{\mathrm{d}t} = \frac{e^{-t/\tau_\mu}}{\tau_\mu}\left[1 + \mathrm{a}(\epsilon)\cos(\theta)\right]\mathrm{n}(\epsilon)\,\mathrm{d}\epsilon\,\mathrm{d}(\cos(\theta)) \tag{3.2a}$$

$$\equiv \frac{e^{-t/\tau_\mu}}{\tau_\mu}\mathrm{K}(\epsilon,\theta)\,\mathrm{n}(\epsilon)\,\mathrm{d}\epsilon\,\mathrm{d}(\cos(\theta)) \tag{3.2b}$$

where the "reduced energy" $\epsilon = E/E_{\max}$, the **asymmetry** $\mathrm{a}(\epsilon) = (2\epsilon - 1)/(3 - 2\epsilon)$, the energy density function $\mathrm{n}(\epsilon) = 2\epsilon^2(3-2\epsilon)$. The maximum positron energy $E_{\max} \simeq 52.8$ MeV, is slightly less than half of the muon rest mass. Integrating over reduced energy (ϵ), we get

$$\mathrm{dW}(\theta) = \frac{e^{-t/\tau_\mu}}{\tau_\mu}\left[1 + \langle \mathrm{a}(\epsilon)\rangle\cos(\theta)\right]\mathrm{d}(\cos(\theta))\mathrm{d}t \tag{3.3}$$

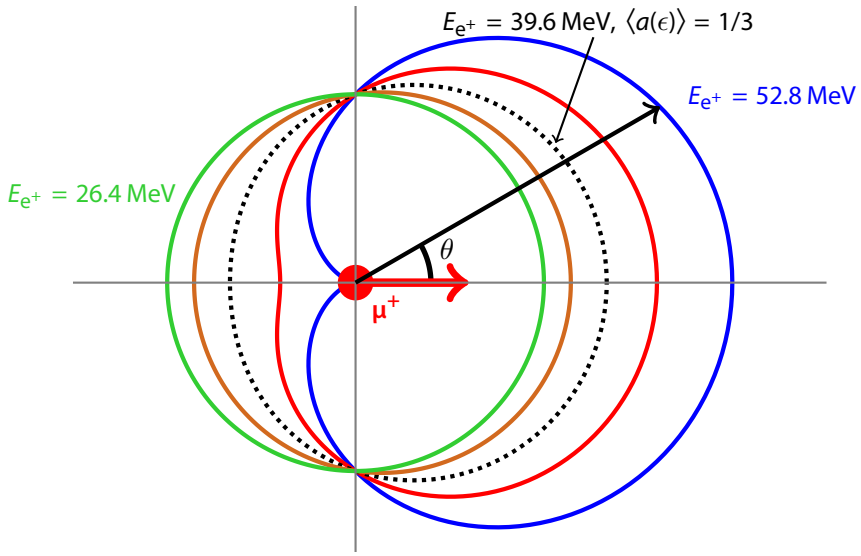

Figure 3.2 : Angular probability distribution (K(ϵ, θ), between 26.4 MeV and 52.8 MeV) of positrons emitted from muons with polarization along the red arrow direction is shown. The maximum average asymmetry for such a β-decay process is 1/3 (the dotted curve).

where, the average of the asymmetry function is

$$\langle a(\epsilon)\rangle = \int_0^1 a(\epsilon)\, n(\epsilon)\, d\epsilon = \frac{1}{3} \tag{3.4}$$

The probability function K(ϵ, θ) as a function of polar angle θ is plotted in figure 3.2 for reduced energy values of ϵ =0.5, 0.625, 0.75, 0.875 and 1.0. The average theoretical β-decay asymmetry is therefore 1/3. The asymmetry is determined in our experiments in a **transverse field (TF-μSR)** arrangement as shown in figure 3.3. **TF-μSR** refers to the case of incoming muon polarization being perpendicular to the external field direction For more details of muon production the reader is referred to references [147, 148].

3.1.2 General μSR Techniques

Detailed descriptions of the various techniques may be found in the following references: the book of Schenck [149], the review article of Cox [150] & of H. Keller [151]. For general technical and statistical details, readers may consult these theses: Riseman [147], Chow [152] and Luke [153]. While conventional surface muon beams can be used to investigate rather small samples, there is a desire for still lower energy muons those can be stopped near sample surfaces (for example to determine depth dependent magnetic field), in thin films and near multi-layer interfaces (to determine exotic magnetic phenomena). Several innovative methods have been developed to produce **ultra slow** muon beams. The results, in this thesis, were obtained using the most successful method mentioned in the next section.

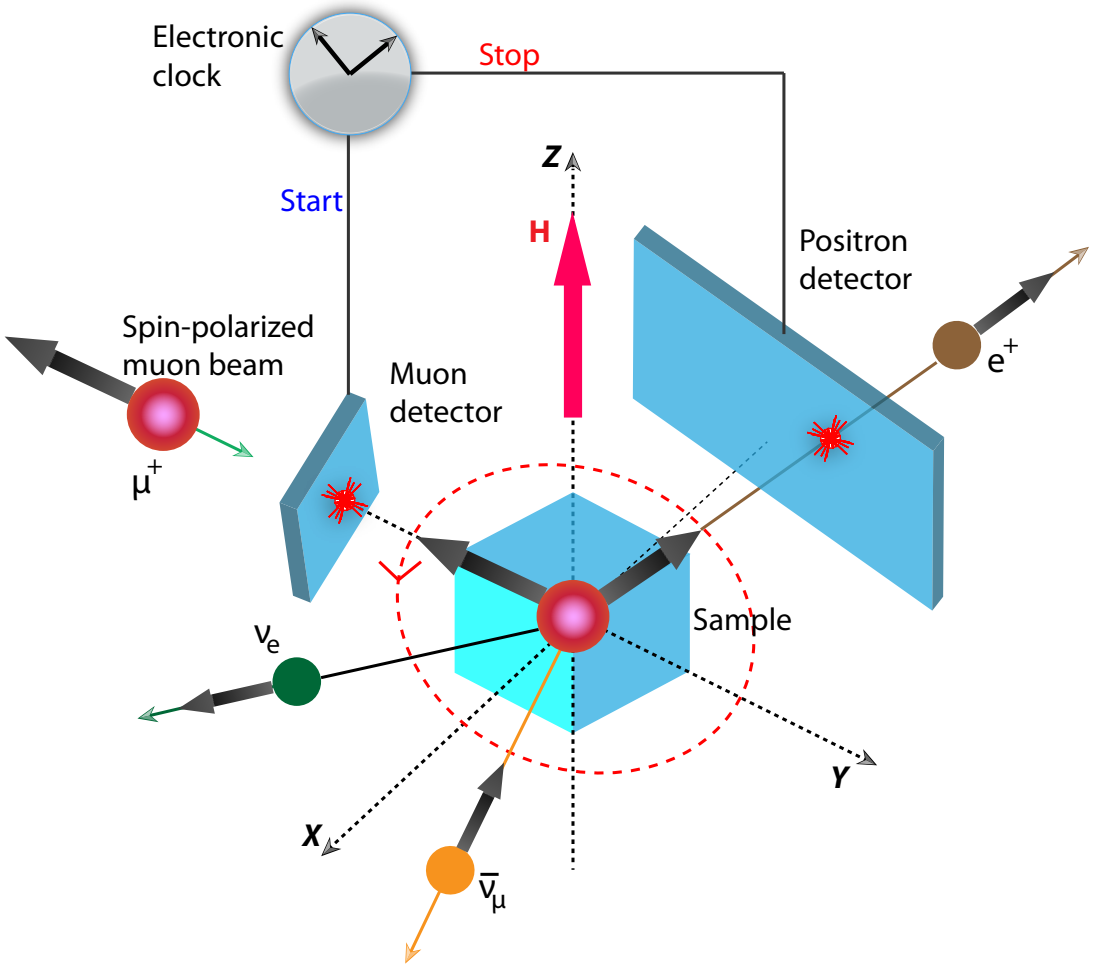

Figure 3.3 : Schematic of the arrangement for a TF-μSR experiment. The muon spin Larmor precesses about the local magnetic field $\boldsymbol{B}$ at its stopping site in the sample, and subsequently undergoes the three-body decay $\mu^+ \rightarrow e^+ + \nu_e + \overline{\nu}_\mu$. The time evolution of the muon spin polarization is accurately determined by detection of the decay positrons from ~ 10^6 muons implanted one at a time.

3.2 Low Energy μSR

The experiments detailed in this thesis were done in the Low Energy Muon ($\leq$ 30 keV) **LEM**-μSR beamline (μE4 [154]) at Paul Scherrer Instituit (PSI). The LEM group has developed a technique of moderating a surface muon beam of 4 MeV down to about 15 eV and then accelerating these muons to form a beam with a tunable energy between 2 keV to 30 keV. Remarkably, these low energy muons remain 100 % spin polarized. Figure 3.4 shows the schematic low energy beamline μE4. The 4 MeV beam passes through a **moderator** consisting of a thin layer (~ 100 nm) of rare gas solid or solid nitrogen deposited on 125 μm silver substrate. A small fraction $\left(10^{-5} \text{ to } 10^{-4}\right)$ of the muons escape the moderator with a mean energy of about 15 eV with an energy spread (FWHM) of ~ 20 eV. The dominant fraction of the beam exits the moderator target as **fast** (de-

graded but not moderated) muons with a mean energy of 500 keV and a FWHM of the same order. These fast muons are separated from the slow ones by an electrostatic mirror composed of a fine wire grid, to deflect the low energy muons by 90 degrees. This deflection, of slow muons, necessarily changes the momentum direction of muons while keeping the spin direction unaltered. After deflection, the muon spin and momentum directions are perpendicular. Fast muons are unaffected by the electrostatic mirror and are monitored by a multi channel plate (MCP) detector. The **low energy muons** are clearly identified by a time-of-flight (TOF) measurement between the start scintillator and the **trigger detector**. The trigger detector, made of an ultra-thin carbon foil $\left(2.2\,\mu g\,cm^{-2}\right)$, is used to set **time-zero,** t_0 for the incoming low energy muons. The muons, traversing the foil, emit a few electrons, which are deflected by 90° and detected by a MCP to give the start signal for the μSR measurement. The trigger detector causes an energy loss of the muons ~ 1.6 keV with a Gaussian energy spread ~ 500 eV. Detection efficiency of the trigger detector is ~ 80 %. After passing the trigger detector, the μ^+ beam is focused on the sample by an Einzel lens (L3) and a conically shaped electrostatic lens. The ring anode labelled RA in figure 3.4 is the final element which also acts to steer and focus the muons onto the sample.

The sample and its Ni-coated[1] Al holder are electrically insulated by a thick sapphire crystal and can be biased -12.5 keV to +12.5 keV. The sapphire crystal also provides a good thermal contact between the cold finger and the sample. The bias voltage (between 12 keV to 20 keV), coupled with the voltage at the trigger detector, determines the muon energy at the sample which is typically in the range 1 keV to 30 keV. A small coil is used to generate a small external magnetic field of up to 20 mT applied parallel to the sample surface and perpendicular to the beam direction. Extensive details on low energy muon beamline may be found elsewhere [155, 156].

3.2.1 Principles of LE-μSR

For each detector one creates a histogram of events as a function of time after arrival of the muon in the sample. The resulting time histograms have the following form:

$$N(t) = N_{\text{bg}} + N_0 e^{-t/\tau_\mu}\left(1 + \mathcal{A}(t)\right), \tag{3.5}$$

where N_0 is the normalization, N_{bg} is a time-independent background and $\mathcal{A}(t)$ is the time dependent asymmetry for the detector along $\hat{\boldsymbol{n}}$ direction, defined as

$$\mathcal{A}(t) = A_0 \mathcal{P}(t) = A_0 \hat{\boldsymbol{n}} \cdot \boldsymbol{\mathcal{P}}(t) \tag{3.6}$$

where A_0 is directly related to the theoretical maximum **asymmetry** a(ϵ) referred in (3.4) The

[1] The sample holder is coated with ~ 1 μg of Ni. Since Ni is ferromagnetic, muons, those miss the sample, strike Ni-coated sample plate and experience a large hyperfine field and disappear from the frequency window of interest. This very effective background suppression method was the critical step which allows low energy μSR to be applied to crystals much smaller than the beam diameter.

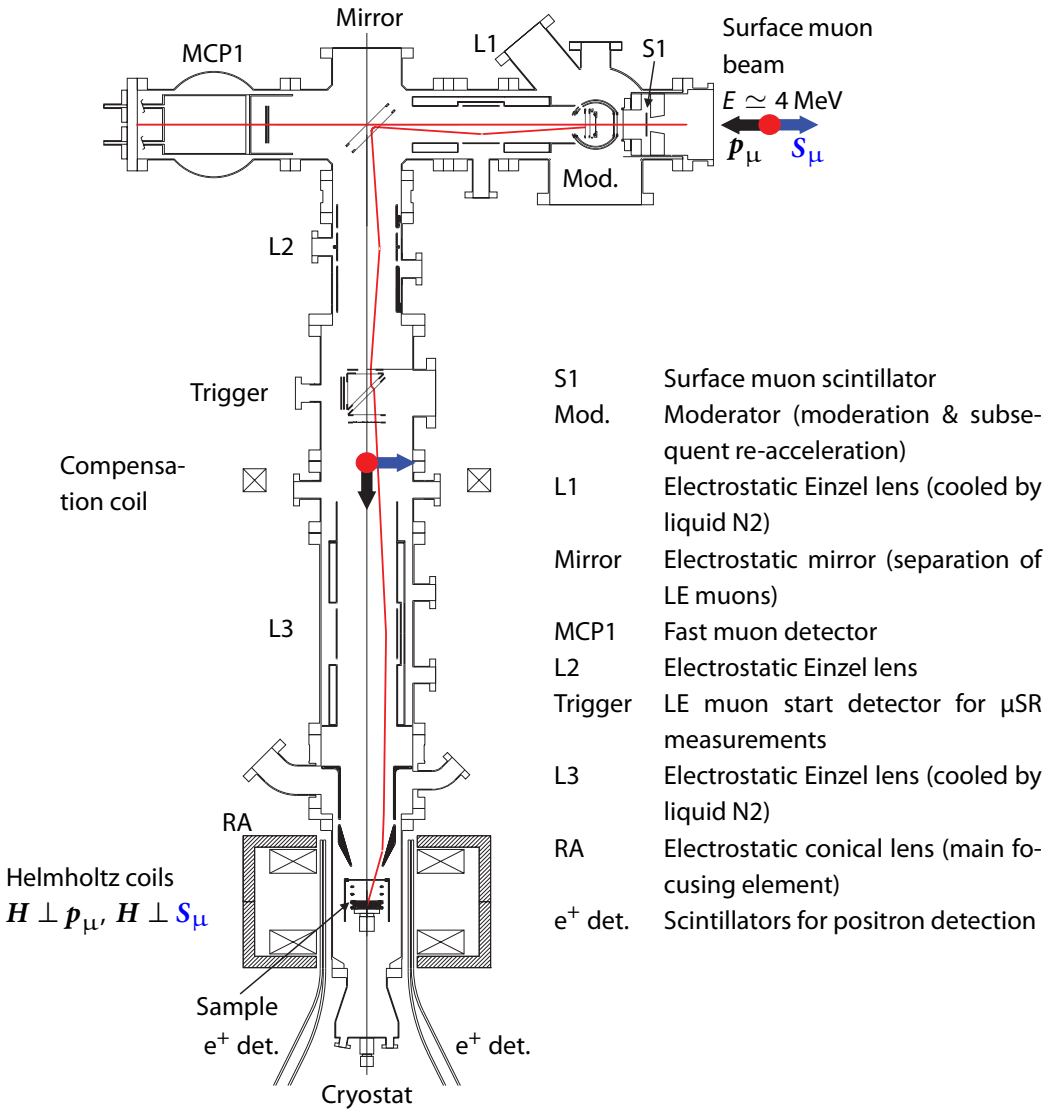

Figure 3.4 : Adapted from [155]: A small fraction of incoming muons incident on the cold moderator come out as slow muons with a mean energy of about 15 eV. They are subsequently accelerated to energies up to 20 keV. The positrons, from the muons decaying in the sample, are detected by four pairs of scintillators surrounding the vacuum tube.

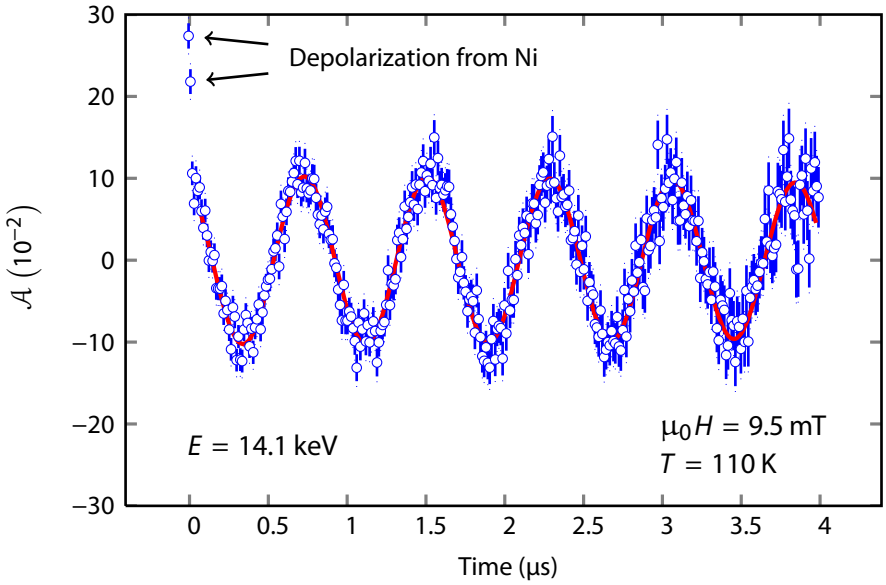

Figure 3.5 : LE-μSR asymmetry spectrum of a $YBa_2Cu_3O_{6.92}$ mosaic in a transverse field of 9.5 mT. The muon implantation energy is 14.1 keV and the temperature is 110 K. Note that the first two points are off the curve; these are attributed to a fast precessing signal in the Ni film which is rapidly dephased in a time $t < 150$ ns. The almost undamped oscillation with a frequency corresponding to the applied field at higher times resulting from muons in the $YBa_2Cu_3O_{6.92}$ mosaic. Consequently all the subsequent analysis cuts out the first 150 ns of data.

muon polarization $\mathcal{P}(t)$ reflects time-dependent spin-polarization and its modulus defined as

$$\mathcal{P}(t) = \frac{\langle \boldsymbol{S}(t) \cdot \boldsymbol{S}(0) \rangle}{\langle S(0)^2 \rangle} \tag{3.7}$$

where $\mathcal{P}(0) = \pm\hat{\boldsymbol{n}}$ and $\hat{\boldsymbol{n}}$ refers to the direction of observation (detector).

The observed asymmetry at $t = 0$ in our samples is typically about 0.12. The reduction compared to theoretical maximum 1/3 is mainly due to the fact that emitted positrons are collected in a finite solid angle and about half of the muons miss the sample. Those that strike the Ni-coated sample plate precess outside the the frequency window of interest and effectively reduce the amplitude of precession close to the Larmor frequency.

3.2.1.1 Spin Evolution in Quantum Mechanics

This discussion follows largely from [157]. In quantum mechanics of a spin-$\frac{1}{2}$ system, the spin operator is given by

$$\boldsymbol{S} = \frac{\hbar}{2}\boldsymbol{\sigma}, \tag{3.8}$$

where $\sigma_x, \sigma_y, \sigma_z$ are Hermitian Pauli matrices, given as

$$\sigma_x = \begin{pmatrix} 0 & 1 \\ 1 & 0 \end{pmatrix}, \sigma_y = \begin{pmatrix} 0 & -i \\ i & 0 \end{pmatrix}, \sigma_z = \begin{pmatrix} 1 & 0 \\ 0 & 1 \end{pmatrix}. \tag{3.9}$$

The eigenstates $\left(|\uparrow\rangle, |\downarrow\rangle\right)$ of σ_z is conventionally chosen as basis states to represent any general spin state (wavefunction)

$$|\psi\rangle = \alpha|\uparrow\rangle + \beta|\downarrow\rangle, \tag{3.10}$$

with the normalization condition,

$$|\alpha|^2 + |\beta|^2 = 1. \tag{3.11}$$

A spin pointing in direction $\hat{\boldsymbol{n}} = (\cos\varphi \sin\theta, \sin\varphi \sin\theta, \cos\theta)$, will be an eigenstate of the projection of the spin operator (3.8), along $\hat{\boldsymbol{n}}$, with eigenvalue of 1, i.e,

$$\hat{\boldsymbol{n}}.\boldsymbol{\sigma} \begin{pmatrix} \alpha \\ \beta \end{pmatrix} = \begin{pmatrix} \alpha \\ \beta \end{pmatrix} \tag{3.12}$$

Solving (3.12), one arrives at the normalized wavefunction

$$|\psi\rangle = \begin{pmatrix} \exp\left(-i\frac{\varphi}{2}\right) \cos\left(\frac{\theta}{2}\right) \\ \exp\left(i\frac{\varphi}{2}\right) \sin\left(\frac{\theta}{2}\right) \end{pmatrix} \tag{3.13}$$

The time evolution of a spin system is dictated by the Zeeman interaction Hamiltonian,

$$\mathcal{H} = -\boldsymbol{\mu} \cdot \boldsymbol{B}, \tag{3.14}$$

where $\boldsymbol{\mu} = \gamma \boldsymbol{S}$ with γ being the gyromagnetic ratio of the relevant particle (or system). Time evolution of the spin system is given by the unitary operator

$$U(t) = \exp\left(-\frac{i}{\hbar}\mathcal{H}t\right) = \exp\left(\frac{i}{2}\boldsymbol{\sigma} \cdot \boldsymbol{B}t\right). \tag{3.15}$$

For simplicity, the applied field may be assumed to be in the z direction, i.e, $\boldsymbol{B} = B\hat{\boldsymbol{z}}$ and the time evolution operator may be written as

$$U(t) = \begin{pmatrix} \exp\left(\frac{i}{2}\gamma Bt\right) & 0 \\ 0 & \exp\left(-\frac{i}{2}\gamma Bt\right) \end{pmatrix} \tag{3.16}$$

At time t, the initial wavefunction (3.13) evolves to

$$|\psi(t)\rangle = U(t)|\psi(0)\rangle = \begin{pmatrix} \exp\left(-\frac{i}{2}(\varphi - \gamma Bt)\right) \cos\left(\frac{\theta}{2}\right) \\ \exp\left(\frac{i}{2}(\varphi - \gamma Bt)\right) \sin\left(\frac{\theta}{2}\right) \end{pmatrix}, \tag{3.17}$$

which clearly shows the initial spin gets rotated around the applied field direction by an angle γBt, with a Larmor precession frequency

$$\omega_{\mathrm{L}} = \gamma B. \tag{3.18}$$

If the initial spin is in the $+x$ ($\varphi = 0, \theta = \pi/2$) direction, (3.13) becomes

$$|\psi\rangle = \frac{1}{\sqrt{2}} \begin{pmatrix} 1 \\ 1 \end{pmatrix} \tag{3.19}$$

and wavefunction at t may be written as

$$|\psi(t)\rangle = \frac{1}{\sqrt{2}} \begin{pmatrix} \exp\left(\frac{i}{2}\omega_{\mathrm{L}} t\right) \\ \exp\left(-\frac{i}{2}\omega_{\mathrm{L}} t\right) \end{pmatrix}. \tag{3.20}$$

The expectation value of the spin operator $S_x = \frac{\hbar}{2}\sigma_x$ may be written as

$$\begin{aligned} \langle\psi(t)|S_x|\psi(t)\rangle &= \left(\frac{\hbar}{2}\right)\left(\cos^2\left(\frac{\omega_{\mathrm{L}} t}{2}\right) - \sin^2\left(\frac{\omega_{\mathrm{L}} t}{2}\right)\right) \\ &= \left(\frac{\hbar}{2}\right)\cos\left(\omega_{\mathrm{L}} t\right) \end{aligned} \tag{3.21}$$

Similarly, the expectation values of spin operators S_y and S_z may be written as

$$\langle\psi(t)|S_y|\psi(t)\rangle = \left(\frac{\hbar}{2}\right)\sin\left(\omega_{\mathrm{L}} t\right) \tag{3.22a}$$

$$\langle\psi(t)|S_z|\psi(t)\rangle = 0 \tag{3.22b}$$

In other words, ensemble average spin precesses in the $x - y$ plane when the applied field is in the z direction.

3.2.1.2 Classical Spin Precession

A similar result can be obtained classically as follows. The ensemble average spin changes according to the Bloch equation may be written as,

$$\frac{\mathrm{d}\boldsymbol{S}}{dt} = \boldsymbol{\mu} \times \boldsymbol{B} \tag{3.23}$$

where, $\boldsymbol{B} = \boldsymbol{B}_{\text{ext}} + \boldsymbol{B}_{\text{int}}$ is the sum of external and internal field. For total magnetic field along $\hat{z}$, $\boldsymbol{B}_{\text{ext}} = B\hat{z}$,

$$\frac{\mathrm{d}S_x}{\mathrm{d}t} = \gamma S_y B \tag{3.24a}$$

$$\frac{\mathrm{d}S_y}{\mathrm{d}t} = \gamma S_x B \tag{3.24b}$$

$$\frac{\mathrm{d}S_z}{\mathrm{d}t} = 0 \tag{3.24c}$$

The above equations (3.24a) and (3.24b) are solved by

$$\begin{aligned} S_x(t) &= S(0)\sin(\gamma B t + \varphi) \\ S_y(t) &= S(0)\cos(\gamma B t + \varphi) \end{aligned} \tag{3.25}$$

where $S(0)$ and φ are determined by spin direction at $t = 0$.

3.2.1.3 Spin Polarization and Asymmetry Spectrum

Here we discuss the effects of (random) internal fields those are present in any sample due to randomly oriented magnetic moments:

$$\mathcal{P}(t) = \iiint P(\boldsymbol{B})\mathcal{P}_B(t)\mathrm{d}\boldsymbol{B} \tag{3.26}$$

where $\boldsymbol{B}$ is the local magnetic field muon experiences, $B = |\boldsymbol{B}|$, $P_B(t)$ is the time-dependent (oscillating) muon polarization and $P(\boldsymbol{B})$ is the normalized probability distribution of magnetic field inside the sample. Inside the sample, randomly oriented magnetic moments can generate a distribution of magnetic field, at any given muon site, and may be approximated by a three-dimensional Gaussian distribution,

$$P(\boldsymbol{B}) = \left(\frac{\gamma_\mu}{\sqrt{2\pi}\sigma}\right)^3 \exp\left(-\frac{\gamma_\mu^2 B^2}{2\sigma^2}\right), \tag{3.27}$$

where γ_μ is the muon gyromagnetic ratio. For an external field perpendicular to muon spin direction, e.g. $\boldsymbol{B}_{\text{ext}} = B_{\text{ext}}\hat{\mathbf{z}}$, the Gaussian probability distribution (3.27) is centered on field $\boldsymbol{B} = (0, 0, B_{\text{ext}})$, and has the form

$$P(\boldsymbol{B}) = \left(\frac{\gamma_\mu}{\sqrt{2\pi}\sigma}\right)^3 \exp\left(-\frac{\gamma_\mu^2\left(B_x^2 + B_y^2 + (B_z - B_{\text{ext}})^2\right)}{2\sigma^2}\right) \tag{3.28}$$

With $\mathcal{P}(0) \parallel \hat{\mathbf{x}}$, the muon polarization may be written as,

$$\begin{aligned}
\mathcal{P}(t) &= \left(\frac{\gamma_\mu}{\sqrt{2\pi}\sigma}\right)^3 \int\int\int \exp\left(-\frac{\gamma_\mu^2\left(B_x^2 + B_y^2 + (B_z - B_{\text{ext}})^2\right)}{2\sigma^2}\right)\cos(\gamma_\mu B t)\mathrm{d}\boldsymbol{B} \\
&\simeq \frac{\gamma_\mu}{\sqrt{2\pi}\sigma}\int_{B_z=-\infty}^{\infty}\exp\left(-\frac{\gamma_\mu^2\left(B_z - B_{\text{ext}}\right)^2}{2\sigma^2}\right)\cos(\gamma_\mu B_z t)\mathrm{d}B_z \\
&= \left(\frac{\gamma_\mu}{\sqrt{2\pi}\sigma}\right)\left(\frac{\sqrt{2}\sigma}{\gamma_\mu}\right)\int_{n=-\infty}^{\infty}\exp\left(-n^2\right)\cos\left(\gamma_\mu\left(\frac{\sqrt{2}\sigma n}{\gamma_\mu} + B_{\text{ext}}\right)t\right)\mathrm{d}n \\
&= \left(\frac{1}{\sqrt{\pi}}\right)\int_{n=-\infty}^{\infty}\exp\left(-n^2\right)\cos\left(\sqrt{2}\sigma t n + \gamma_\mu B_{\text{ext}} t\right)\mathrm{d}n \\
&= \exp\left(-\frac{\sigma^2 t^2}{2}\right)\cos\left(\gamma_\mu B_{\text{ext}} t\right)
\end{aligned} \tag{3.29}$$

As may be seen from (3.29), random moments in a sample cause damping in the muon polarization. Additionally, when muons are implanted into a sample with inequivalent magnetic sites (e.g. superconducting state), there will be a distribution ($\rho(B)$), discussed in detail in the following section, of fields ($B(z) \equiv B_{\text{ext}}(z)$) inside the sample & the polarization (3.29) takes the form

$$\mathcal{P}(t) = \exp\left(-\frac{\sigma^2 t^2}{2}\right)\int_0^{\infty}\rho(z)\cos\left(\gamma_\mu B(z) t\right)\mathrm{d}z \tag{3.30}$$

The asymmetry $\mathcal{A}(t) = A_0\mathcal{P}(t)$ is fitted to the experimentally observed asymmetries to obtain physical parameters $A_0,\ \sigma, d,\ \lambda$, where d and λ are deadlayer and London penetration depth in the Meissner state.

An example histogram of raw data, from the **forward** counter and asymmetry $\mathcal{A}(t)$ are given in figure 3.6. In this experiment, a transverse external field of 9.5 mT was applied and the resulting sinusoidal oscillations can be taken into account by the theoretical model in (3.30). For the purposes of this thesis, the most important characteristic of the muon polarization decay spectrum is the average precession frequency - which is a direct measure of the local magnetic field averaged over the stopping distribution.

3.2.2 Stopping Distribution

Even at a single muon implantation energy, ions bombarded onto a material, end up at different depths due to randomness in the collision process. The energy dependent stopping profiles can be generated using "Transport of Ions in Solids" (TRIM) codes introduced by Ziegler *et al* [158] based on the ideas of Eckstein [159]. The accuracy of TRIM, in calculating ion range distributions in various materials, is well established and they are routinely used in similar depth controlled experiments such as Low-Energy μSR. By specifying the energy, charge, and mass of the probe ions (μ^+ in this thesis), and the mass density and atomic numbers of the elements of the probed material, one is able to simulate the implantation profile using TRIM. Generated

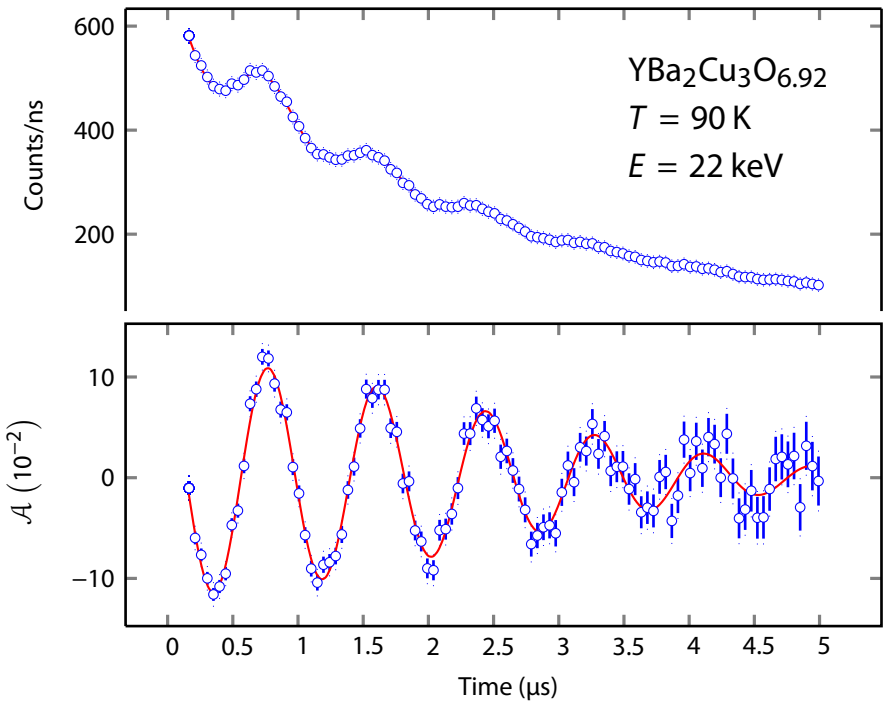

Figure 3.6 : Top: A histogram from "forward" positron detector in a time-differential measurement on the sample of $YBa_2Cu_3O_{6.92}$ crystal mosaic, depicting the exponential decay of the muons and muon precession. Bottom: Larmor precession of muons' spin magnetic moment may be noticed from the time dependence of asymmetry $\mathcal{A}(t)$, in an external applied field of 9.5 mT with an implantation energy of 22 keV, at the temperature of 90 K.

energy-dependent profiles of YBCO are shown in figure 3.7. The average depth of muons increases with energy and an almost linear relationship ($\langle z_\mu \rangle (E) = 3.26 + 4.37^*E$ nm) is obtained as shown in figure 3.7. For $Ba(Co_{0.074}Fe_{0.926})_2As_2$, a different energy dependent linear relationship ($\langle z_\mu \rangle (E) = 4.26 + 4.53^*E$ nm) is obtained. The non-zero mean depth at $E = 0$ is due to the Gaussian distribution (of width 0.45 keV) of any energy that has been set. The stopping profiles are only relevant for the μ^+ ions stopping in the probed material. A fraction of incoming μ^+ ions stop at Ni-coated sample plate where it quickly depolarizes (see figure 3.5) and do not affect the frequency spectrum from the sample. A review of depth resolved studies of materials may be found in [156, 160] and references therein.

3.2.3 Maximum Entropy (ME) Fourier Analysis

The stopping distribution $\rho(z)$ introduced in the previous sections, in conjunction with the London model field decay, can be used to calculate a theoretical muon frequency spectrum in the Meissner state. Typically, we fit the observed precession frequency to the above model to extract the parameters of interest such as the magnetic penetration depth. However, sometimes it is useful to compare the theoretical frequency distribution with an experimental frequency distribution with minimal modeling. In principle, a fast Fourier transform is one way to approximate the experimental frequency distribution. However there are distortions due to ringing etc. in a

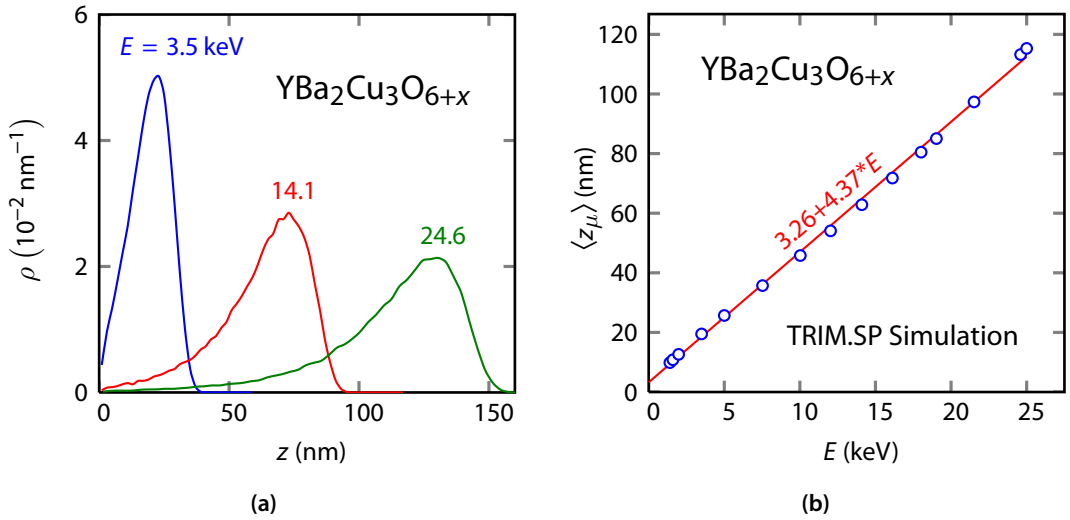

Figure 3.7 : Muon implantation profiles in YBCO: **(a)** Implanted muons stop at different depths even if the incoming beam energy is the same. By specifying the energy, charge and mass of the μ^+ ions, and the mass density and atomic numbers of the elements, profiles are simulated via Monte-Carlo algorithm using TRIM.SP. The accuracy of TRIM.SP, in calculating ion range distributions in various materials, is well established and TRIM.SP is routinely used in similar depth controlled experiments. **(b)** Average muon implantation depth $\left(\langle z_\mu \rangle = \int \rho(z) dz\right)$ is shown. A linear fit (3.26 + 4.37*E) well describes the average implantation depth as a function of muon energy.

Fourier transform. A better way is to generate the experimental frequency distribution by using the principle of maximum entropy (ME). In the ME method, a trial field distribution function $P_{\mathrm{ME}}(b_j)$ is proposed where the the amplitudes of histogram bin j, are the fitting parameters. Fourier transforming the trial field distribution, one obtains the theoretical complex asymmetry

$$A_{\mathrm{complex}}(t_k) = \sum_{b_{j,\min}}^{b_{j,\max}} P_{\mathrm{ME}}(b_j) \exp\left(i2\pi\gamma_\mu b_j t_k\right) \delta b_j \equiv A_r(t_k) + iA_i(t_k), \tag{3.31}$$

where $A_r(t_k)$ and $A_i(t_k)$ correspond to fictional detectors with phases of 0 and 90 degrees with respect to the initial muon polarization. The actual ME asymmetry for a counter is then calculated as

$$A_{\mathrm{ME}}(t_k) = \cos(\phi) A_r(t_k) + \sin(\phi) A_i(t_k), \tag{3.32}$$

where ϕ is the detector phase relative to the incoming muon spin direction. The theoretical function above can then be used to calculate a χ^2:

$$\chi^2 = \sum_{k=1}^{M} \frac{\left(A(t_k) - A_{\mathrm{ME}}(t_k)\right)^2}{\sigma^2(t_k)}, \tag{3.33}$$

where $A(t_k)$ is the measured asymmetry amplitude in k-th bin and $\sigma(t_k)$ is the error in measured asymmetry. Unfortunately, the (3.33) has many fit parameters and additional information is required to obtain the **most likely solution**. The ME method introduces an entropy term, in this

regard:

$$S = -\sum_j \frac{P(b_j)}{e(b_j)P_d} \ln \frac{P(b_j)}{e(b_j)P_d}, \tag{3.34}$$

with the default value P_d is related to statistical noise in the spectra and $e(b_j)$ are ``independent errors''. Adding the χ^2 term using a Lagrange multiplier α, a constrained entropy S_c is defined as

$$S_c = \alpha S - \frac{1}{2l^2}\chi^2, \tag{3.35}$$

with the constraint

$$\chi^2 \equiv l^2 M, \tag{3.36}$$

where the ``looseness'' factor l is introduced to account for any imperfect timing in the experimental electronics and to account for the ME Fourier transformation being overly sensitive to errors $\sigma(t)$. In practice, a l few percent above 1 is good enough to estimate field distributions for most data described in this thesis. The goal of the ME fitting routine is to maximize the constrained entropy given in the (3.35). Extensive details of ME analysis may be found elsewhere [161--164].

CHAPTER 4 RESULTS AND ANALYSES

In this chapter, we present the first direct measurements of λ in the Meissner state of high quality crystals of cuprates and pnictides. Measurements of λ and its anisotropy in the $a-b$ plane are presented for three different oxygen (x = 6.52, 6.92 and 6.998) contents of $YBa_2Cu_3O_{6+x}$. In addition we present measurements of the in-plane λ on a single crystal of Co doped $Ba(Co_{0.074}Fe_{0.926})_2As_2$. Measured values of λ and the anisotropies are, in some cases, considerably different from that of literature, often found with less direct methods.

The local magnetic field decreases inside a superconductor, on a length scale λ, according to the London model, described in section 2.2. Close to the surface, there may be deviations from a purely exponential $B(z)$ as conjectured in (2.18). The magnetic field profile can be detected using LE-μSR since the muon precession frequency is proportional to the local magnetic field. A schematic representation of the fitting procedure to obtain λ and other parameters is shown in figure 4.1. In the normal state, the external field ($\mu_0 H$) penetrates the sample fully yielding an average muon precession frequency of $\left(\gamma_\mu \mu_0 H\right)/2\pi$. A distribution of the local fields, from randomly oriented nuclear moments (see (3.29)), is accounted for by the broadening parameter σ. In the superconducting state, the muon precession frequency depends on implantation depth (z). For the muons landing between depth z and $z + \mathrm{d}z$, the time dependent asymmetry may be written as

$$\mathcal{A}(t) = A_0 \exp\left[-\sigma^2 t^2/2\right] \times \int \rho(z) \cos\left[\gamma_\mu B(z, d, \lambda) t + \varphi\right] dz. \tag{4.1}$$

A slightly modified form (4.2) of the above equation (4.1) is used to fit **all** the data presented in this chapter and thereby to extract the relevant parameters of interest $A_0, d, \sigma, \lambda, \varphi$. Average magnetic fields $\langle B \rangle$ are computed from the above mentioned parameters for various externally applied magnetic fields ranging from 1.5 mT to 10 mT. All measurements in the superconducting state were carried out under **zero-field-cooled** conditions in order to avoid flux penetration into the sample. Note in a field-cooled experiment it is possible for vortices to become trapped inside the sample even below H_{c1}.

The data analyses, in this chapter, are presented chronologically:

(i) $YBa_2Cu_3O_{6.92}$, section 4.1.1.

(ii) $YBa_2Cu_3O_{6.998}$, section 4.1.3

(iii) $YBa_2Cu_3O_{6.52}$, section 4.1.4

(iv) $Ba(Co_{0.07}Fe_{0.93})_2As_2$, section 4.2

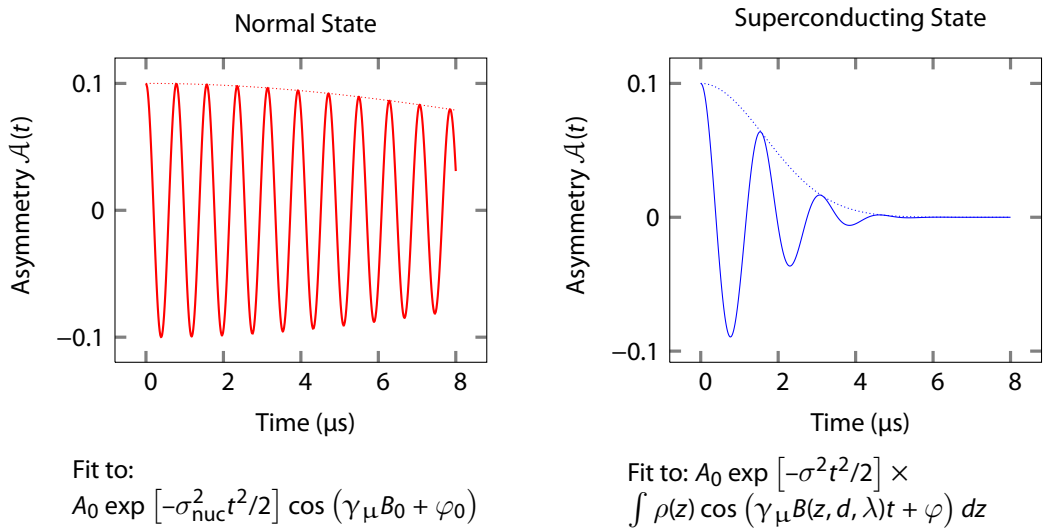

Figure 4.1 : Quick outline of the fitting procedure: Left: In the normal state, oscillatory signal in muon polarization is fitted to a cosine function with a small Gaussian broadening (σ_{nuc}) originating from randomly oriented local internal fields. Right: In the superconducting state, polarization is a sum of frequency $\left(\gamma_\mu B\right)$ dependent oscillation and an additional broadening σ taking into account expelled flux from neighboring crystals or from any other sources of random fields.

4.1 LE-μSR Experiments on YBCO Single Crystals

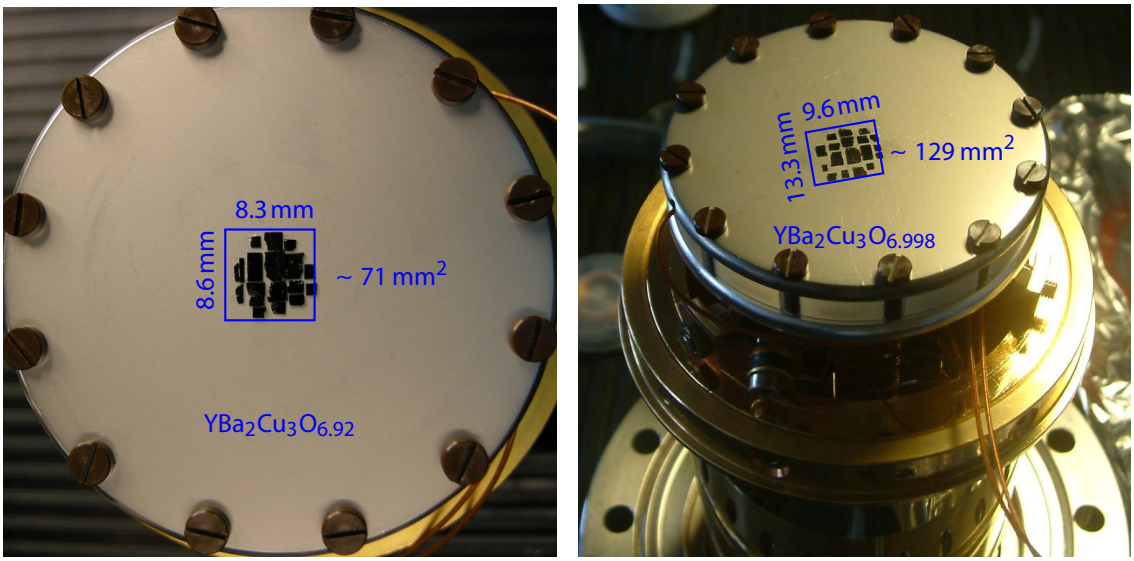

Figure 4.2 : Mosaics of detwinned crystals: The total areas of the boxes surrounding the mosaics are about 71 mm^2 and 129 mm^2 for $YBa_2Cu_3O_{6.92}$ and $YBa_2Cu_3O_{6.998}$, respectively. Each of the crystals was approximately 1 mm to 3 mm in the $a-b$ plane and a c-axis thickness of 0.1 mm to 0.3 mm. An ultra high vacuum compatible Ag epoxy was used to attach each crystal to the sample holder of high purity Al coated with 1 μm of Ni.

The LE-μSR experiments on $YBa_2Cu_3O_{6+x}$ were conducted on a mosaic of small freshly grown single crystals using the self-flux method [165]. The purity of the crystals is the same as for

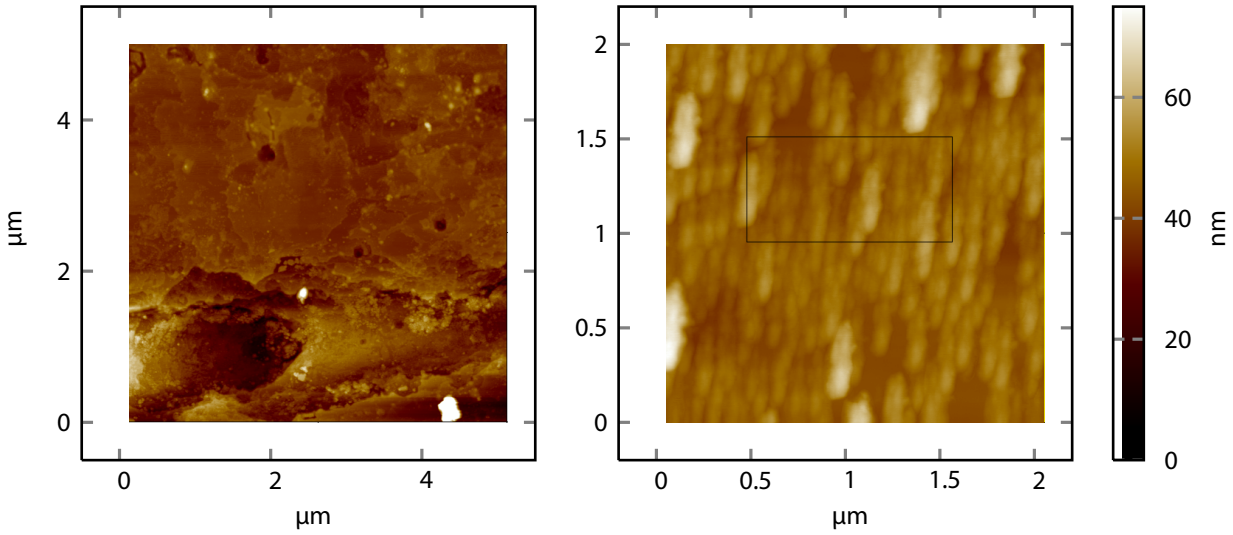

Figure 4.3 : YBCO roughness: Left figure shows a 5 µm×5 µm area of a $YBa_2Cu_3O_{6.92}$ crystal being scanned by tapping AFM. Right figure shows another region of a smaller size and even smaller sized box. A 2 nm to 3 nm of average roughness is found from these measurements.

crystals in which quantum oscillations in resistivity have recently been reported [166]. Each of the crystals was approximately rectangular in shape with lateral dimensions in the a-b plane ranging from 1 mm to 3 mm and a thickness in the c-direction ranging from 0.1 mm to 0.3 mm. They were detwinned to a level greater than 95 %. The mosaic of $YBa_2Cu_3O_{6.92}$ and $YBa_2Cu_3O_{6.998}$ on the coldfinger is shown in the figure 4.2. Two crystal mosaics with different O concentrations were mounted in a very similar method. The crystal faces were mirror-like in appearance and atomic force microscopy indicated the roughness of the surface was few nm on a short length scale (cf. figure 4.3). A UHV compatible Ag epoxy was used to attach each crystal to the sample holder made of high purity Al coated with 1 µm of Ni. Muons that miss the sample stop at the polycrystalline Ni coated sample holder and experience a large (~ 64 mT, see [167]) hyperfine field from Ni moments; thereby removing them from the frequency window of interest. Control experiments on a Ag disc the same size as the sample showed that such a thin layer of Ni has no effect on the precession signal in the Ag sample. The amplitude of the precession signal in all the experiments was typically about 0.11 which is considerably smaller than the instrumental maximum asymmetry of about 0.28. As mentioned previously in chapter 3, this reduction is due to the fact that only about 40 % muons land in the $YBa_2Cu_3O_{6+x}$ crystals; the remaining muons which land in the Ni do not contribute to the precession signal but still produce positrons that are detected by the telescopes.

4.1.1 $YBa_2Cu_3O_{6.92}$

The precession signal in the superconducting state was fit to the following form which is equivalent to (4.1)

$$\mathcal{A}(t) = A_0 \exp\left(-\frac{\sigma^2 t^2}{2}\right) \int \rho(B) \cos\left[\gamma_\mu B(z, d, \lambda)t + \varphi\right] \mathrm{d}B, \tag{4.2}$$

The difference compared to (4.1) is that the integration is over the field distribution $\rho(B)$ instead of the stopping distribution $\rho(z)$. $\rho(B)$ is defined as

$$\rho(B) = \rho(z) \left|\frac{dB}{dz}\right|^{-1} \tag{4.3}$$

Although equations (4.1) and (4.2) are mathematically equivalent for the analysis presented in this thesis, the latter offers a more general approach for analyzing data using models where a specific field distribution is believed to be present. To take into account any random local field present at a muon site, a Gaussian probability model is assumed as,

$$P\left(B', B\right) = \left(\frac{1}{\sqrt{2\pi}\Delta B}\right) \exp\left(-\frac{1}{2}\left(\frac{B' - B}{\Delta B}\right)^2\right) \tag{4.4}$$

where $P\left(B', B\right)$ is the probability function of the total field experienced by muon and ΔB is the width of the probability function. The total probability density is obtained by convoluting (4.4) with the field distribution from the pure London model in the (4.3)

$$\rho'\left(B'\right) \equiv \int_{B=0}^{\infty} P\left(B', B\right) \rho(B)\, \mathrm{d}B \tag{4.5}$$

Since the stopping distributions ($\rho(z)$) are obtained as discrete numbers from TRIM.SP simulations, the integral in (4.5) is replaced by a summation to calculate the total probability density. As may be seen from the figure 4.4a, the field distributions from a maximum-entropy (ME) analysis [162--164] are wider than that expected from a pure London model ($\sigma_{\mathrm{nuc}} = 0$). For the ME analysis a Gaussian apodization ($t_{\mathrm{apod}} = 2.0\,\mu\mathrm{s}$) is used for all the energy dependent spectra. In apodization, the statistical errors in asymmetry are enhanced, by multiplying with an increasing function in time, for the later part of a spectrum, as

$$\sigma_{\mathrm{apodized}}(t) \equiv \exp\left(+\frac{t^2}{t_{\mathrm{apod}}^2}\right) \sigma(t). \tag{4.6}$$

The apodization time is chosen such that at $\sqrt{2}t_{\mathrm{apod}}$, the asymmetry signal either fully relaxes or disappears in noise. Apodization leads to a very small symmetric broadening and smoothing of

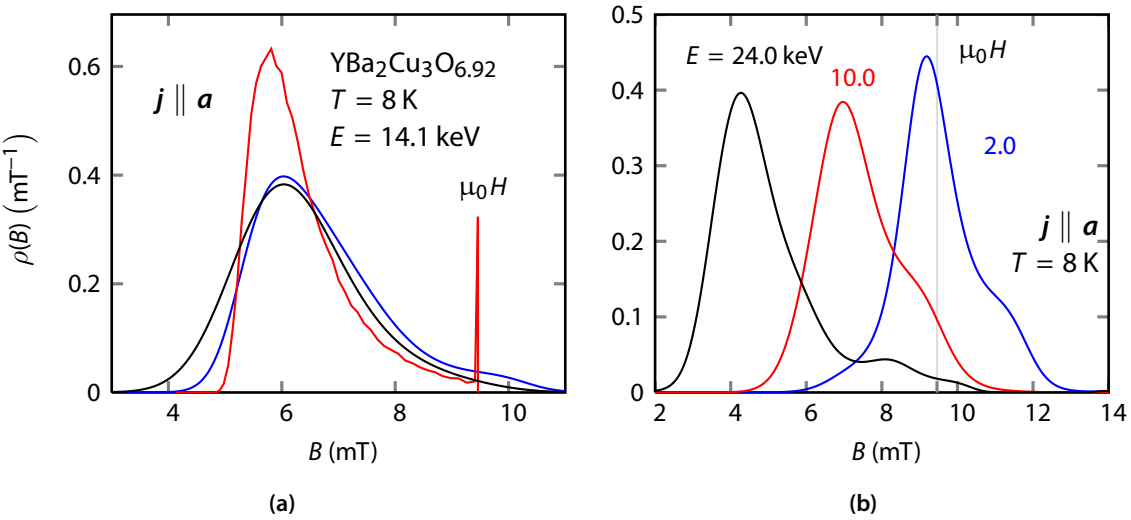

Figure 4.4 : (a) Magnetic field distribution as seen by muons at an implantation energy of $E = 14.1$ keV and at $T = 8$ K in an external magnetic field $\mu_0 H = 9.5$ mT, applied parallel to the b axis of the crystals. The field distribution corresponds to the asymmetry spectrum (△) in the figure 4.6. The red line (——) is model field from pure London model with $d = 10.3$ nm, $\lambda_a = 128.9$ nm and $\sigma_{\text{nuc}} = 0$. The spike in $\rho(B)$ at the applied field is from muons stopping in dead layer. The black line (——) is the theoretical distribution convoluted with a Gaussian with a second central moment $\Delta B = 0.72$ mT corresponding to the average $\sigma_{\text{nuc}} = 0.61\ \mu\text{s}^{-1}$ from the figure 4.8a). The blue line (——) is obtained from maximum-entropy analysis. The the slight difference between the ME results and the London model may, in part, be due to the simplified model we are using for the deadlayer. The higher weight at high fields in the actual field distribution may be due to from trapped vortices close to the surface and is not taken fully into account by our symmetrically broadened field distribution. (b) Maximum-entropy field distributions are shown at three different energies. At the lowest energy, there is significant broadening which may be due to muons close to the surface where there may be broadening due to vortices or demagnetization affects.

the field distribution but is not expected to change the average magnetic field $\langle B \rangle$. It is interesting to note that there is some weight at fields (cf. figure 4.4b) higher than the applied field $\mu_0 H$ which cannot be accounted for by (4.3). However, it should be noted that χ^2/DF is close to 1 (cf. table 4.1) in the Meissner model fit (4.3) and as such actual field distributions cannot be very different from the ones realized from the Meissner model (4.3). Also, the phase (φ) of the incoming muon beam is not properly taken into account in the ME analysis. Yet, tails in ME field distribution (figure 4.4b) are indication of higher fields than predicted from our simple model, possibly due to a small fraction of muons seeing a large fields at the edges of the sample. Also the fast reduction (due to Ni hyperfine interactions) of asymmetry in earlier times (cf. figure 4.5) contributes to the long tail in field distribution. In one sense, ME gives a better representation of the field distribution since it does not involve any particular model. However, for the purposes of extracting useful parameters such as λ, fits to the Meissner model in the time domain are more useful. Figure 4.5 shows a comparison of Meissner model fit and prediction from maximum-entropy Fourier analysis. As has been argued before, fast decay [168] in asymmetry, in the first [0-0.15] μs, is due to muons' interaction of large random field from Ni moments. From the asymmetry spectra figure 4.5 (top panel), it is clear that no discernible

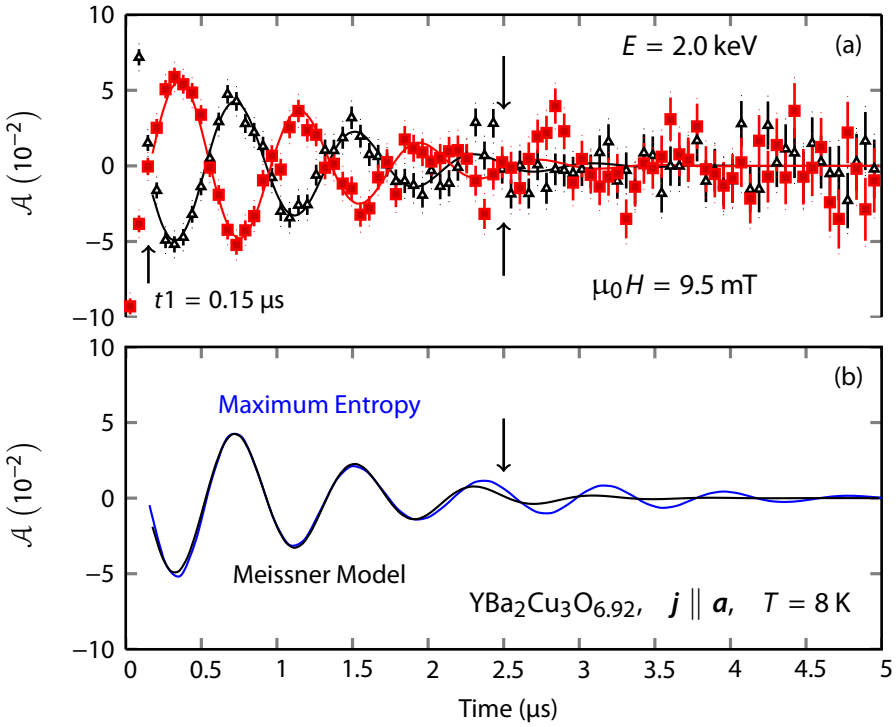

Figure 4.5 : Comparison of Meissner model fits and maximum-entropy Fourier results: **(a)** The red (■) and black (△) points represent the muon asymmetry spectra in $YBa_2Cu_3O_{6.92}$ at energy 2 keV in an external field of 9.5 mT. The solid red (——) and black (——) lines are maximum-entropy fits (0.15 μs to 8.0 μs) to the spectra. Fits exclude [0 – 0.15] μs - which primarily contains precession from Ni (sample plate). The arrows at 2.5 μs point to the time where the experimental asymmetry signal is lost in noise. **(b)** A comparison of theoretical fits of maximum-entropy (——) and London model (——) is shown. It is clear that no discernible experimental asymmetry is left after 2.5 μs; while ME predicts a small oscillating asymmetry for an additional ~ 2.0 μs. This suggests that the ME prediction of field distribution should be viewed with caution.

experimental asymmetry is left after 2.5 μs; while ME predicts a small oscillating asymmetry for an additional ~ 2.0 μs. This suggests that the ME prediction of field distribution is to be viewed with some caution. The longer tails in figure 4.4 are indicative of higher local magnetic field experienced by muons landing close to the sample surface. This may in part be due to ME transformation which can produce signal where there are not any.

In the equations (4.1) and (4.2), φ should depend only on geometric parameters and the average muon arrival time on the sample. Thus, one way to analyze the spectra is to fix φ to values obtained at some temperature above T_c, as has been described in [157]. However, φ may be different in the superconducting state compared to the values for $T > T_c$, as we will see shortly. φ may also depend on muon implantation energy in the following manner: in the normal state ($T > T_c$), the angular part of the asymmetry is given by

$$\mathcal{A}(t) \sim \cos\left(\omega(t - t_0)\right) \tag{4.7}$$

assuming $\varphi = 0$, for simplicity. Here $\omega = \gamma_\mu B$ is the frequency and t_0 being the time muon

enters the sample. If an error is made in determining $t_0 \rightarrow t_0 - dt$, then (4.7) becomes

$$\mathcal{A}(t) \sim \cos\left(\omega(t - t_0) + \omega dt\right) \tag{4.8}$$

Equation (4.8) implies that the fitted phase will be ωdt. However, in the superconducting state and at a high implantation energy, muons deep inside the sample will see a reduced field and a corresponding reduced frequency $\omega'_E < \omega$, assuming for simplicity that all the muons precess in a single frequency. This implies that, in superconducting state, (4.8) may be written as

$$\mathcal{A}(t) \sim \cos\left(\omega'_E(t - t_0) + \omega'_E dt\right) \tag{4.9}$$

implying a phase shift of $(\omega'_E - \omega)dt$, relative to the normal state, will be detected. The possibility of the actual frequency distribution being more asymmetric than our theoretical frequency distribution one can also introduce an apparent phase shift. To summarize, imperfections in the fitting function, time-of-flight distribution and detector geometry may all contribute to an energy dependent phase shift. For this reason, phases for individual energies were kept free (**individual phase**) in the global fit. A shared phase global fit analysis (**shared phase**) was also done which yields $\lambda_{a/b}$ values within the systematic errors ~ 3 nm. This is also a strong indication that the subtleties of muon arrival time, detector geometry and thereby the phases (φ) and broadening parameter (σ) do not significantly influence absolute values of magnetic penetration depth reported from these measurements.

Figure 4.6a shows the muon precession signal in the normal state at 110 K in a small magnetic field of 9.5 mT applied along the *a* axis of the crystals with an implantation energy at 14.1 keV. The fitted precession signal in figure 4.6a also includes a damping rate of 0.086(11) μs^{-1} which is consistent with that expected from randomly oriented Cu nuclear dipole moments. Meissner screening of the external field is apparent by comparing the normal state (figure 4.6a) with the superconducting state (figure 4.6b). As mentioned earlier, the superconducting state data are fitted to (4.2) with shared A_0, d and λ for all the spectra at 8 K in both *a* and *b* directions. The depth dependence of the average internal field is evident by comparing the two spectra (▵ and ■) in figure 4.6b which have different implantation profiles. Examples of the field profiles are shown in figure 3.7a. Figure 4.7 shows the average local field [$\langle B \rangle = \int \rho(z)B(z)dz$] determined from fits at a single energy as a function of beam energy (bottom scale) and corresponding mean implantation depth (top scale). The filled circles (○) and filled squares (■) are from data taken with the shielding currents flowing along the *a* and *b* axes respectively (or equivalently the magnetic field along the *b* and *a* axes respectively). The corresponding London model curves are generated from a global fit of runs taken at 8 K for both orientations and all energies using the calculated TRIM.SP implantation profiles. The common parameters are $\lambda_a = 128.9(12)$ nm, $\lambda_b = 108.4(10)$ nm and $d = 10.3(4)$ nm. In the **shared phase** fits, d is fixed to 10.3 nm and the obtained $\lambda_{a/b}$ differs by only about 1 nm as shown in the table 4.1. Statistical uncertainties are determined from the

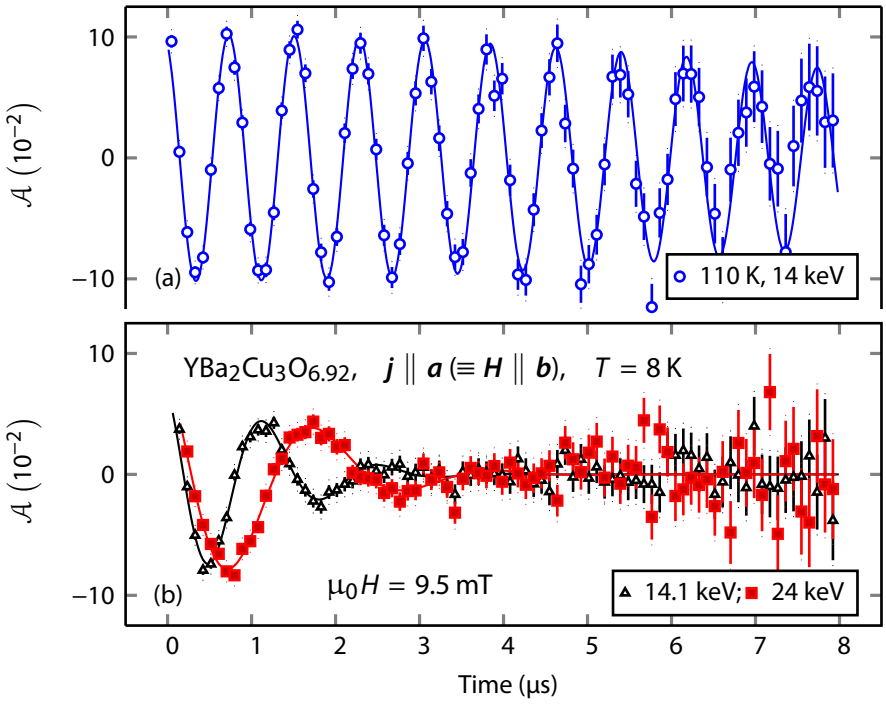

Figure 4.6 : **(a)** The muon spin precession signal in the normal state of $YBa_2Cu_3O_{6.92}$ at 110 K in an external field of 9.5 mT applied parallel to the *b* direction. The mean implantation energy is $E = 14.1$ keV which corresponds to a mean implantation depth of 65 nm. In the normal state, external field ($\mu_0 H$) penetrates the sample fully and all implanted muons experience the same magnetic field - which is reflected in the precession frequency of the asymmetry spectrum. A small damping of asymmetry is due top randomly oriented Cu nuclear dipole moments. **(b)** The same conditions as top panel, except in the superconducting state at $T = 8$ K for two energies 14.1 keV and 24 keV. $\boldsymbol{H} \parallel \boldsymbol{b}$ results in shielding current flowing parallel to *a* direction ($\boldsymbol{j} \parallel \boldsymbol{a}$). Notice the drop in average frequency in the superconducting states. Higher energy muons experience a corresponding distribution of lower magnetic fields due to London decay and due to muons stopping at different depths. The distribution of fields causes rapid dephasing of muon polarization and consequently a loss of signal at ~ 2.5 μs.

global χ^2 surface and take into account the correlation between $\lambda_{a/b}$ and d. Since there is almost no correlation between d and λ_a/λ_b, this ratio is determined more accurately than the absolute values of λ_a and λ_b as may be seen in the table 4.1. As may be evidenced from figure 4.7, the average field falls exponentially from the surface for higher implantation energies however, close to the surface, deviation from a simple exponential is modeled from the curvature at the lowest energies. This implies that the shielding current is suppressed near the surface relative to a London model. This model of a simple deadlayer is idealized but the nature of the data does not warrant more complicated picture. It is unclear to what extent this suppression of the supercurrent density is intrinsic as a result of the discontinuous nature of electronic properties near a surface. A suppression of the supercurrent density was also reported in a previous low energy μSR study of the field profile in a thin film of $YBa_2Cu_3O_{6.92}$ and attributed to surface roughness [169]. It is difficult to exclude such extrinsic effects which could also lead to a suppression of the supercurrent density near a surface. Measurements on atomically flat cleaved surfaces are

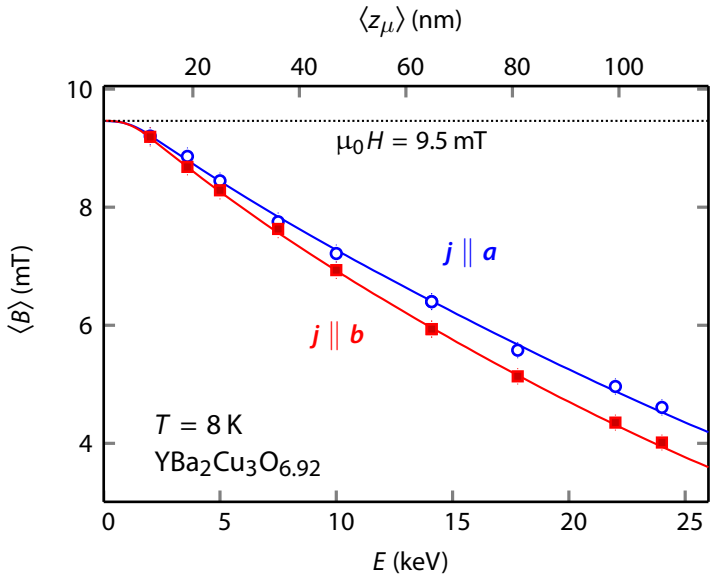

Figure 4.7 : (a) The average magnetic field (⟨B⟩) versus mean stopping depth in an applied field of 9.5 mT such that the shielding currents are flowing in the *a* direction ($j \parallel a$,○) and *b* direction ($j \parallel b$,■). The curves are the average fields generated from a global fit of all the spectra at 8 K taken at all energies and for both orientations. The common parameters are λ_a, λ_b and d. The individual points are from a fit to the same model but at a single depth. The differences between the data points and curves reflect how close the data at a single energy agrees to the global fit.

needed to resolve the origin of d. There are no other measurements of electromagnetic properties as a function of depth in $YBa_2Cu_3O_{6.92}$ crystals to compare with. Surface sensitive techniques such as STM and ARPES are only sensitive to the top few unit cells where the properties can be very different than in the bulk.

It may also be noted from figure 4.8a, that the fitted asymmetry drops from 0.10 at 2 keV to 0.05 at 2 keV. This is expected since at low energies, incoming muons have an angular distribution as they approach the sample surface and at lower energy, many of them undergo large angle scattering such that they can be back scattered off the surface. Such muons form muonium $\left(\mu^+e^-\right)$ or stop in the walls of the stainless steel vacuum vessel. In either case, they do not contribute to the precession signal at the Larmor frequency. The average phase from the **individual phase** fits is close to that from the **shared phase** fits, indicating that the latter model determines some "effective average phase" as one would expect. The energy dependence of the broadening parameter σ reflects the random local fields and is also temperature independent below 0.8 T_c, as evidenced from data shown in figure 4.8b. This suggests there may be bulk magnetization effects, whereby flux expelled from neighboring crystals broadens the magnetic field distribution at the surface of any given crystal. However, it will be seen in the next section that σ did not change appreciably when the crystals were separated (cf. figure 4.2). This indicates that each crystal of YBCO experiences a distribution of fields independent of the other crystals. This in turn suggests the broadening may be related to the bulk demagnetization effects and/or surface

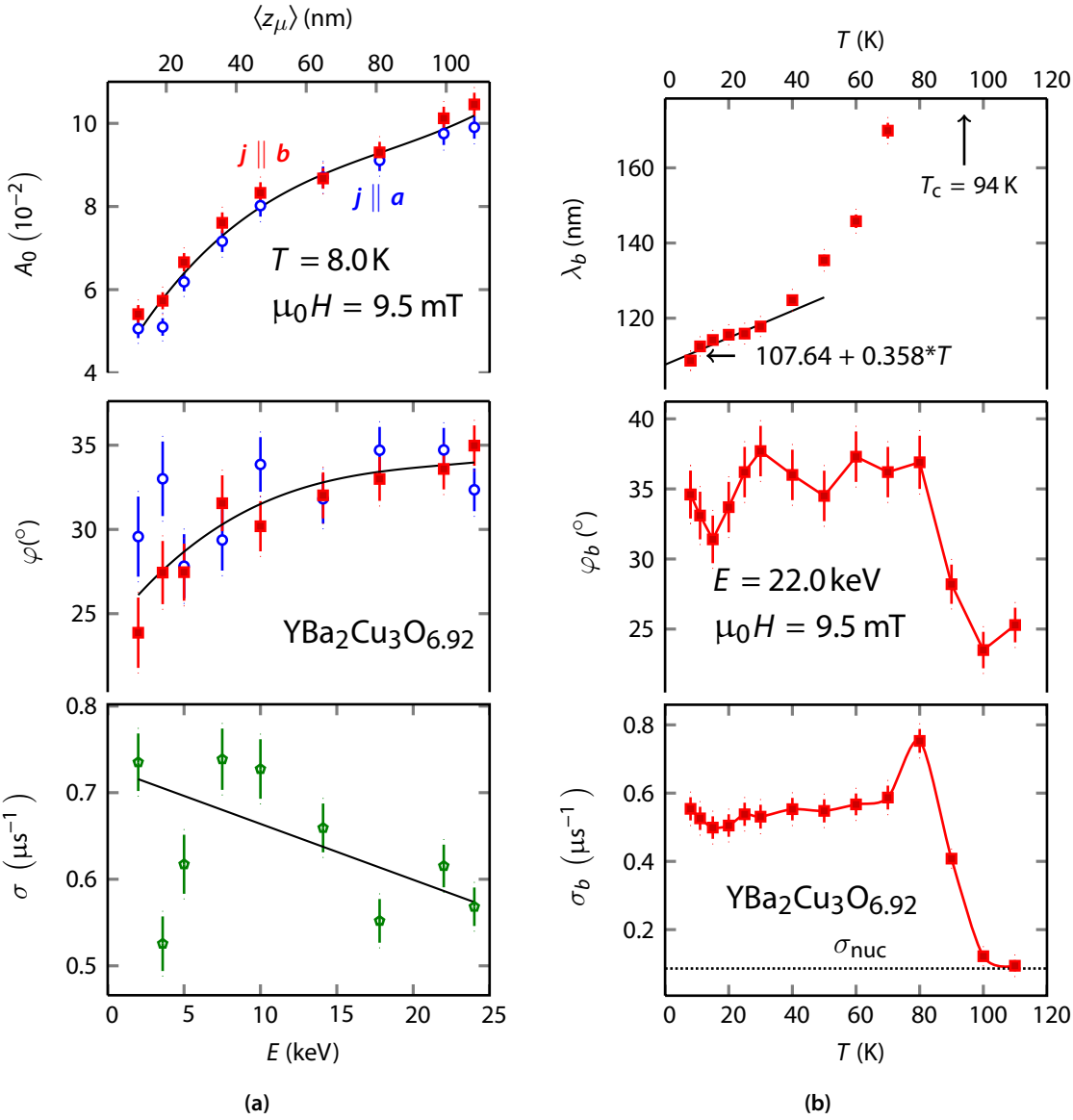

Figure 4.8 : (a) The asymmetry, phase and broadening parameter versus mean stopping depth in an applied field of 9.5 mT in $YBa_2Cu_3O_{6.92}$ in the global fit of all asymmetry spectra in both directions (*a, b*). The asymmetry and phase were kept as free parameters at each energy dependent spectra. Reduced asymmetry at lower energies is due to backscattering of muons. The dipolar broadening σ is shared in both directions. (b) Temperature dependence of λ, φ and σ when $\boldsymbol{j} \parallel \boldsymbol{b}$. The slope from the linear fit of $\sigma_b(T)$ is used to extrapolate $\lambda_{a/b}(T = 8\,\mathrm{K})$ to their zero kelving values $\lambda_{a/b}(T = 0\,\mathrm{K})$.

Table 4.1 : Summary of results in $YBa_2Cu_3O_{6.92}$: Measured magnetic penetration depths at 8 K are shown for two models: "phase individual" and "phase shared", for individual energies. The errors are reported here are purely statistical. An additional ~ 2 % (~ 2 nm) error is due to uncertainty in stopping distribution. It may be noted that the two phase models yield penetration depths within a nm of each other for both *a* and *b* axis, stressing that the determination of phase does not affect the measurement of absolute λ.

B (mT)	*d* (nm)	φ ($^\circ$)	λ_a(8 K) (nm)	λ_b(8 K) (nm)	$\mathcal{R} \equiv \lambda_a/\lambda_b$	χ^2/DF
9.46	10.3(5)	32.2(6)[a]	128.9(12)	108.4(10)	1.19(1)	1.058
	10.3 (fixed)	33.0(8)[b]	130.2(14)	109.2(12)	1.19(1)	1.069

[a] Average of energy specific phases from "individual phase" analysis.
[b] Global phase from "shared phase" analysis.

roughness. Since σ reflects the broadening of an **effective field** at a specific energy, it is kept as a free parameter both in **individual phase** and **shared phase** models.

Table 4.1 gives our results for λ_a and λ_b measured at 8 K in $YBa_2Cu_3O_{6.92}$. The errors reported here are purely the statistical uncertainties. Systematic errors due to uncertainties in the muon stopping distribution and the extrapolation to 0 K are estimated to be about 3 %. At the moment, the latter dominates the overall uncertainty but should improve with refinements of the stopping distribution calculations.

4.1.2 Temperature Dependence of Penetration Depth and Estimation of Energy Gap in $YBa_2Cu_3O_{6.92}$

The absolute value of λ_b as a function of temperature is shown in figure 4.8b. The data points are the fitted values of λ_b determined from a fit to the model at a single implantation energy of 22 keV. Since d is not temperature dependent it was fixed at 10.3 nm. The solid line is a linear fit of our data below 30 K and gives a slope of 0.357(67) nm K^{-1}. This was used to extrapolate our measurement of λ_b at 8 K down to zero temperature. The slope and extrapolated value depend slightly on the fitted temperature range, adding an additional systematic error of about 1 nm. To obtain $\lambda_a(0)$, normalized superfluid density in *a* and *b* axis directions are taken as approximately equal, for $T < 8$ K, as in the (4.10)

$$\left(\frac{\lambda_a(0)}{\lambda_a(T)}\right)^2 \simeq \left(\frac{\lambda_b(0)}{\lambda_b(T)}\right)^2$$
$$\Rightarrow \lambda_a(0) = \lambda_b(0)\left(\frac{\lambda_a(T)}{\lambda_b(T)}\right), \tag{4.10}$$

where $\lambda_{a/b}(T)$ are the finite temperature penetration depths measured by our modified London model. For low temperatures (4.10) is justified as may be seen from the 0 – 40 K fits of superfluid density in figure 4.10. This is reasonable since $1/\lambda^2 \propto n_s/m^*$ and n_s is a scalar quantity independent of orientation. Thus to the extent that the effective mass tensor is T-independent one would not expect $(\lambda(0)/\lambda(T))^2$ to be orientation dependent.

The temperature dependence of the magnetic penetration depth and the corresponding superfluid density are shown in the figures 4.9 and 4.10. For determination of $\lambda_{a/b}(T)$, the dead layer has been fixed to 10.3 nm as d is not expected to change with temperature. The obtained $\lambda_{a/b}$ are fitted according to the semiclassical model of a cylindrical Fermi surface [170] where the normalized superfluid density is given by

$$\left(\frac{\lambda(0)}{\lambda(T)}\right)_a^2 = 1 - \frac{1}{2\pi k_B T}\int_0^{2\pi}\cos^2\phi\int_0^{\infty}\cosh^{-2}\left(\frac{\sqrt{\epsilon^2+\Delta^2(\phi,T)}}{2k_BT}\right)d\epsilon d\phi \tag{4.11a}$$

$$\left(\frac{\lambda(0)}{\lambda(T)}\right)_b^2 = 1 - \frac{1}{2\pi k_B T}\int_0^{2\pi}\sin^2\phi\int_0^{\infty}\cosh^{-2}\left(\frac{\sqrt{\epsilon^2+\Delta^2(\phi,T)}}{2k_BT}\right)d\epsilon d\phi \tag{4.11b}$$

where $\sqrt{\epsilon^2+\Delta^2(\phi,T)}$ is the quasiparticle (pair) energy. The temperature dependence of the gap is approximated by

$$\Delta(T) = \Delta_0(0)\tanh\left(\frac{\pi k_B T_c}{\Delta_0(0)}\sqrt{a\left(\frac{T_c}{T}-1\right)}\right)g(\phi), \tag{4.12}$$

where $\Delta_0(0)$ is zero temperature gap energy and $g_d = \cos(2\phi)$, $a_d = 4/3$ for a $d_{x^2-y^2}$ gap symmetry. In the weak-coupling limit, $\Delta_0(0) \approx 2.14\,k_BT_c$ [171]. The model in the equations (4.11a) and (4.11b) is employed to fit the data in the figure 4.9 and also shown in the figure 4.10.

The fit parameters in the model are $\Delta_{0,a/b}(0)$, $\lambda_{a/b}(0)$ while T_c is fixed to 94 K. The fit is done for data $T \leq 40$ K. Note that the applied magnetic field exceeds H_{c1} [174] at $T \simeq 55$ K. The fits yield $\lambda_a(0) = 125.9(19)$ nm, $\lambda_b(0) = 108.5(10)$ nm, $\Delta_{0,d,a}(0) = 23.3(60)$ meV $= 2.87(74)\,k_BT_c$ and $\Delta_{0,d,b}(0) = 23.7(34)$ meV $= 2.92(42)\,k_BT_c$ and thereby $|\Delta_a/\Delta_b|$ (defined as[1] $|\Delta_{0,d,a}(0)/\Delta_{0,d,b}(0)|$) $= 0.98(29)$. Fits to the microwave(μW) data, using the absolute values of $\lambda_{a/b}(0\,\text{K})$, yields $|\Delta_a/\Delta_b| = 2.73\,k_BT_c/2.62\,k_BT_c = 1.04$. The μSR gap values are higher than the weak coupling predictions. The gap anisotropy is close to that found via other methods: ARPES [175] ($|\Delta_a/\Delta_b| = 0.86$), Raman scattering [176] ($|\Delta_a/\Delta_b| = 0.83$), phase sensitive measurement [177] ($|\Delta_a/\Delta_b| = 0.82$). Although YBCO is thought to be primarily of $d_{x^2-y^2}$-wave gap superconductor, there are measurements suggesting an additional s-wave gap [178] from an upturn in superfluid density for $T \leq 10$ K. In $YBa_2Cu_3O_{6.92}$, as shown in figure 4.10, there is no such upturn. Based on the current data we may conclude that inclusion of an additional gap is not warranted.

In summary of this section, we have used low energy μSR to measure the magnetic field profiles in the Meissner state of a mosaic of detwinned single crystals of $YBa_2Cu_3O_{6.92}$. The comparison of $\lambda_{a/b}$ values obtained here with those from different methods is deferred until a later section. Since the data analysis method for the next three sections will be very similar to

[1] Note that the fitted energy gaps may be considered as "effective d-wave gaps" in a and b directions. An additional isotropic gap (eg. s-wave) may give rise to an anisotropic overall gap.

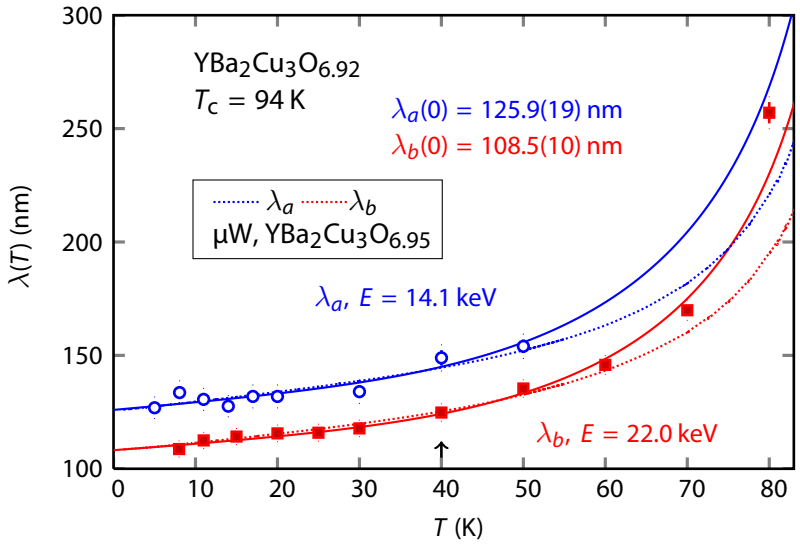

Figure 4.9 : Temperature dependence of the penetration depth $\lambda(T)$ for the two crystal orientations (a/b) at energies 14.1 keV and 22.0 keV, respectively. $\lambda(T)$ should be independent of muon implantation energies. The solid lines (——,——) are fits to the equations (4.11a) and (4.11b), with a pure $d_{x^2-y^2}$-wave order parameter symmetry, of the temperature region $0 \leq T \leq 40$ K (↑). Penetration depth data from microwave (μW : ·····, ·····) measurements [172, 173], shifted to agree to the $\lambda_{a/b}(0\,\mathrm{K})$ from the $d_{x^2-y^2}$-wave phenomenological fits, are also shown. Microwave data measures $\Delta\lambda(T)$ which requires the absolute value of the λ at some temperature before it can be converted to a T-dependence of the superfluid density. Interestingly, microwave data deviates from LE-μSR measurements for $T > 50$ K - the temperature at which $\mu_0 H$ exceeds H_{c1} and vortices start to enter.

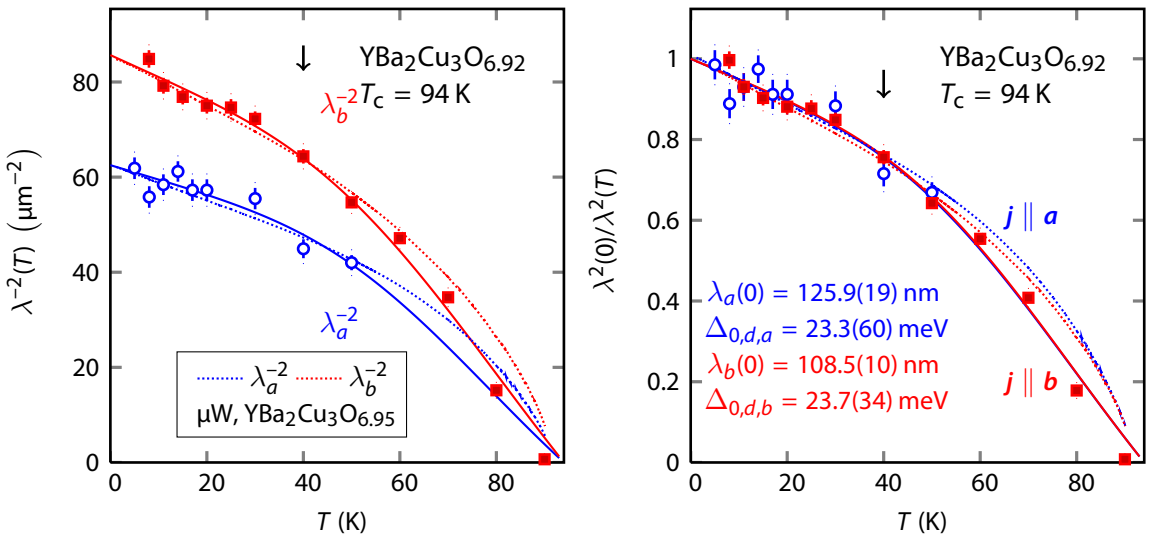

Figure 4.10 : (a) Temperature dependence of λ_a^{-2} and λ_b^{-2}. With the solid lines are fits to the equations (4.11a) and (4.11b), with a pure $d_{x^2-y^2}$-wave order parameter symmetry, in the temperature region $0 \leq T \leq 40$ K. (b) Normalized superfluid density. It may be noted that $\lambda_a^2(0)/\lambda^2(T) \simeq \lambda_b^2(0)/\lambda^2(T)$ for $T \leq 50$ K for both the μSR and the μW data. The fitted values of $\lambda_{a/b}(0\,\mathrm{K})$ from these temperature dependence is slightly different from the global fit measurements given in table 4.1. Penetration depth data from microwave measurements [172, 173], shifted to agree to the $\lambda_{a/b}(0\,\mathrm{K})$ from the $d_{x^2-y^2}$-wave phenomenological fits, are also shown. Note that there is close agreement between the current data and the microwave data for $T < 50$ K.

this one, we will primarily focus on discussing differences.

4.1.3 $YBa_2Cu_3O_{6.998}$

In this section, we present the analysis of a total of four sets of data: (i) in an external field of 4.7 mT at three temperatures 4 K, 5 K and 12 K (ii) in an external field of 9.5 mT at the temperature of 5 K.

Examples of the muon precession signals in the crystal mosaic may be seen in figure 4.11. Figure 4.11a shows the muon precession signal in the normal state at 100 K in a small magnetic field of 4.7 mT applied along the *a* axis of the crystals with an implantation energy at 23.1 keV. In figure 4.11a, the average frequency corresponds to the applied field with a damping rate of

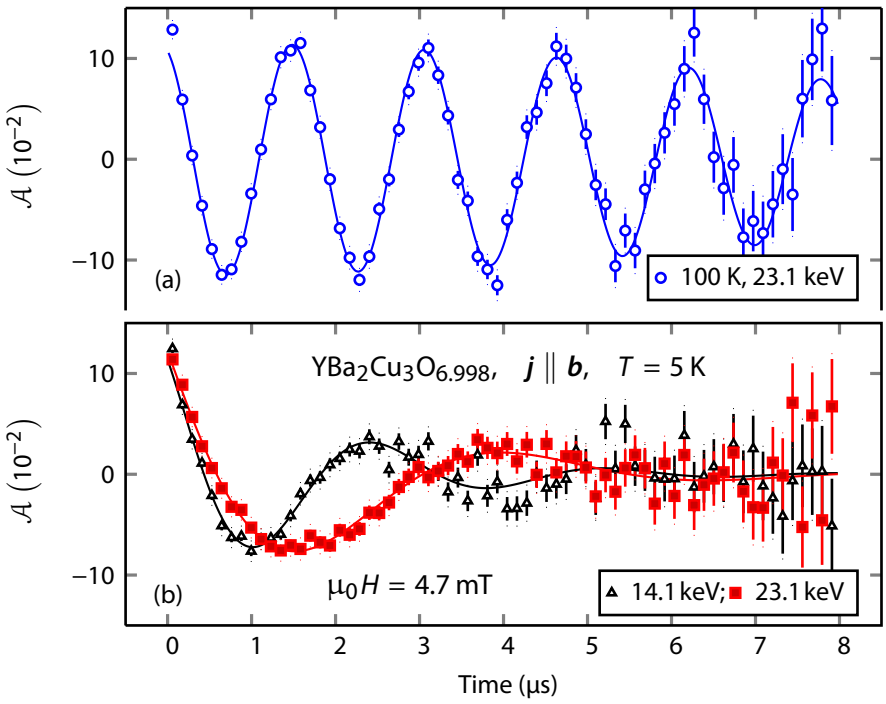

Figure 4.11 : (a) The muon spin precession signal in the normal state of $YBa_2Cu_3O_{6.998}$ at 100 K, 23.1 keV in an external field of 4.7 mT applied parallel to the *a* direction.(b) The same conditions as (a) except in the superconducting state at T = 5 K with an two implantation energies 14.1 keV and 23.1 keV. The solid lines are fits to a London model profile described in the previous section.

0.110(10) μs^{-1}, which is slightly larger than obtained in $YBa_2Cu_3O_{6.92}$, where the fitted σ was 0.086(11) μs^{-1}. All measurements in the superconducting state were carried out under **zero-field-cooled** conditions in order to avoid flux trapping at the surface. Meissner screening of the external field is apparent by comparing the normal state in figure 4.11a with the superconducting states in figure 4.11b. The depth dependence of the average internal field(ω) is also evident by comparing the two spectra in the figure 4.11b which have different implantation profiles. The curves in figure 4.11b are generated from fits to a London model profile as described in the previous section.

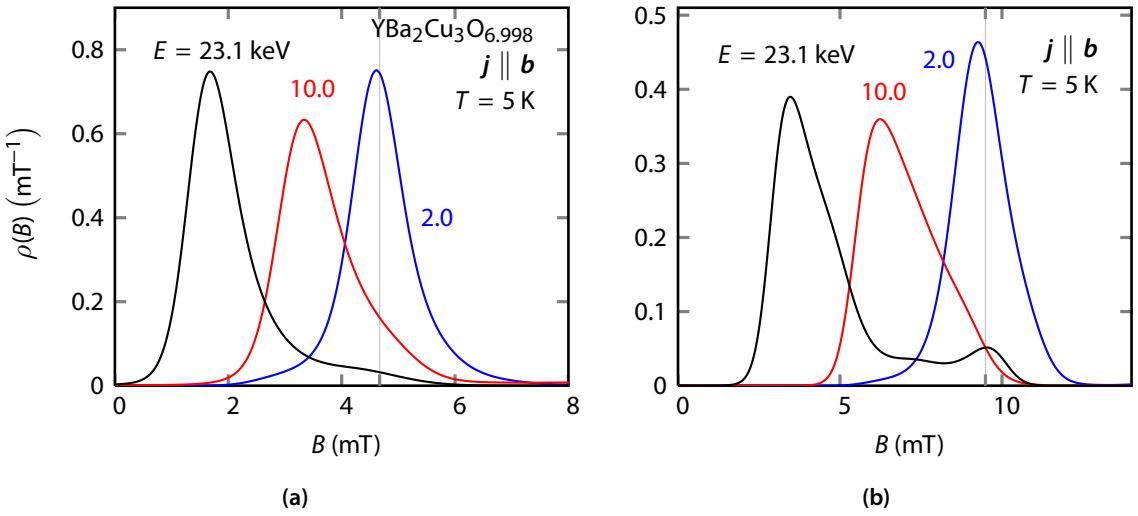

Figure 4.12 : Magnetic field distributions generated by maximum-entropy method at various implantation energies and at $T = 5$ K in an external applied magnetic field $(\mu_0 H)$ of (a) 4.7 mT and (b) 9.5 mT, applied parallel to the *a* axis.

Maximum entropy field distributions corresponding to the two external fields of 4.7 mT and 9.5 mT are shown in the figure 4.12. As may be noticed, $\rho(B)$, determined at the higher applied field (9.5 mT), is more asymmetric. However, in both cases, there are long tails, in field distributions, even at higher implantation energies possibly due to trapped vortices (dead layer) close to the surface.

At low temperatures, significantly below the critical temperature T_c, the broadening parameter σ is about 0.4 μs^{-1} (figure 4.13) which is about half of that observed (figure 4.8a) in $YBa_2Cu_3O_{6.92}$ in 9.5 mT. The mosaic geometry has virtually no effect on σ - which indicates that muons experience broadened field distribution in each crystal, possibly due to surface roughness and/or demagnetization effects at the edges of each crystal. However, simulations done by Mike *et al.* [1] suggest that $\sigma(E)$ having a peak at some energy - which is not observed.

Figure 4.14 shows the average local field $\langle B \rangle = \int \rho(z)B(z)dz$ determined from fits at a single energy as a function of beam energy (bottom scale) and corresponding mean implantation depth (top scale). The open circles and filled squares are from data taken with the shielding currents flowing along the *a* and *b* axes respectively (or equivalently the magnetic field along the *b* and *a* axes respectively). As may be noticed in figure 4.14, the theoretical global fitted $\langle B \rangle$ curves are in excellent agreement with the individually measured $\langle B \rangle$. The common parameters are all shown in the table 4.2 and $\lambda_{a/b}$ along with χ^2 per degrees of freedom are plotted in the figure 4.18. Since there is almost no correlation between d and λ_a/λ_b, this ratio is determined more accurately than the absolute values of λ_a and λ_b as shown in the seventh column of the table 4.2. Slightly different penetration depths $\lambda_{a/b}$ and other parameters are obtained in the **individual phase** fits compared to the **shared phase** fits. Differences in average magnetic field between the two models

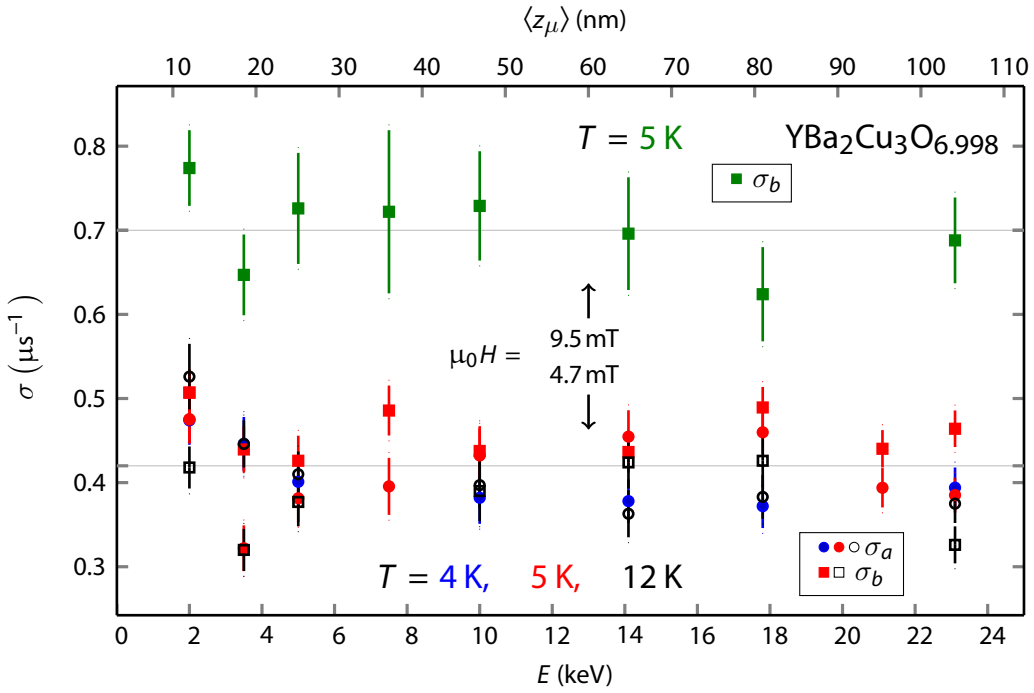

Figure 4.13 : Broadening parameter as function of mean energy or depth for various magnetic fields: The three important parameters for individual energy runs in the global fit, with shared λ_a, λ_b and d are shown. The broadening parameter (σ) shows some random variation with averages close to 0.42 μs^{-1} and 0.7 μs^{-1} at the external fields of $\mu_0 H$ = 4.7 mT and 9.5 mT , respectively.

are negligible.

Figure 4.15 shows the temperature dependence of penetration depth λ_a at 4.7 mT and 23.1 keV. The λ_a's are obtained via the method of "individual phase" analysis of measurements with fixed d = 14.79 nm, obtained from global fit of measurements in both a and b direction. The measured λ_a's are fitted to a line giving $\lambda_a(0\,\mathrm{K})$ = 112.26(146) nm and slope of the line $\left(\Delta\lambda/\Delta T = 0.495(78)\,\mathrm{nm\,K^{-1}}\right)$. Since these measurements were done at a single energy, $\lambda_a(0\,\mathrm{K})$ is not as good a measure of penetration depth at zero temperature. Nevertheless, the fitted magnetic penetration depth ($\lambda_a(5\,\mathrm{K}) \sim 115$ nm) is close to the absolute λ_a's found from global fits as shown in the table 4.2. The $\Delta\lambda/\Delta T$ is a good measure of low temperature dependence of λ_a and can be used to extrapolate zero temperature penetration depths from the finite temperature ones.

It may be noted that $\lambda_{a/b}$ increases slightly as the temperature is increased, from 4 K to 5 K, which is consistent with $\sim$ 0.5 $\mathrm{nm\,K^{-1}}$, found from the temperature dependence in the figure 4.15. It may also be noted that the ratio between the two penetration depths, $\mathcal{R}$, varies only slightly ($\sim$ 4 %) depending on whether the **individual phase** or the **shared phase** model was used. Furthermore, the difference is within the statistical ($\sim$ 1 % to 2 %) and systematic uncertainties ($\sim$ 3 %) in $\lambda_{a/b}$. The **goodness of fit**, χ^2/DF, becomes slightly worse ($\sim$ 10 %) with the **shared phase** model, which is reasonable since there are fewer degrees of freedom with the shared phase

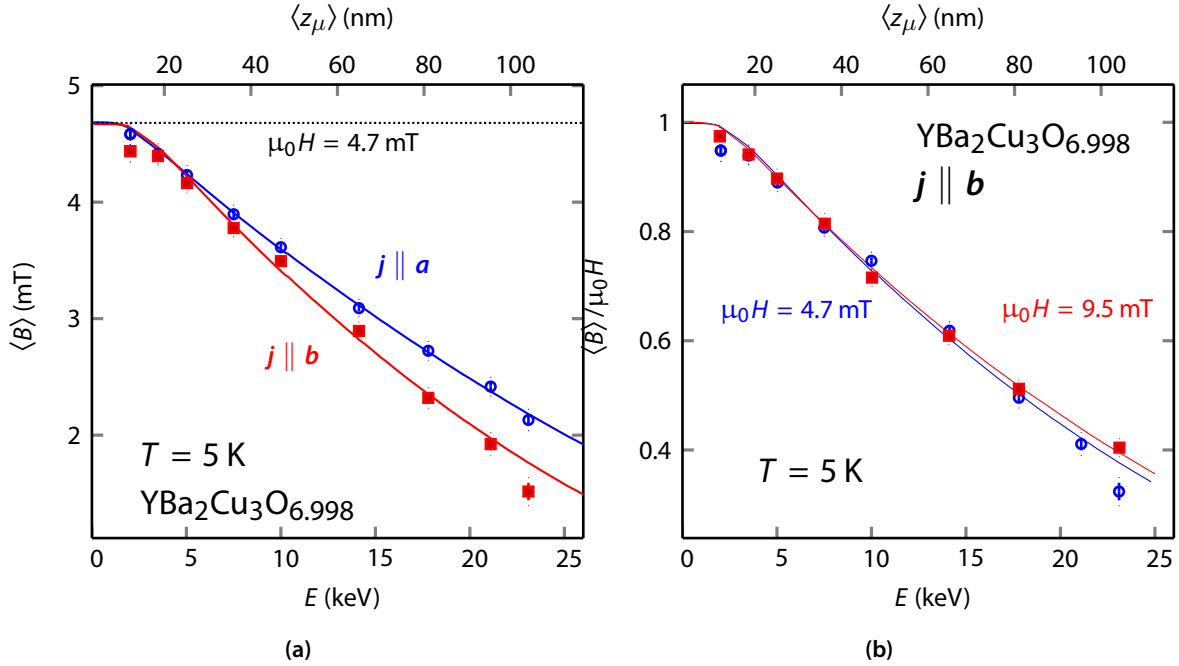

Figure 4.14 : (a) The average magnetic field (⟨B⟩) versus mean stopping depth in an applied field of 4.7 mT. The curves are the average fields generated from a global fit of all the spectra at 5 K taken at all energies and for both orientations (cf. figure 4.7). (b) Relative average magnetic fields in this sample for two temperatures and two magnetic fields. It is apparent that the absolute magnetic penetration depths measured at the low different magnetic fields are almost the same.

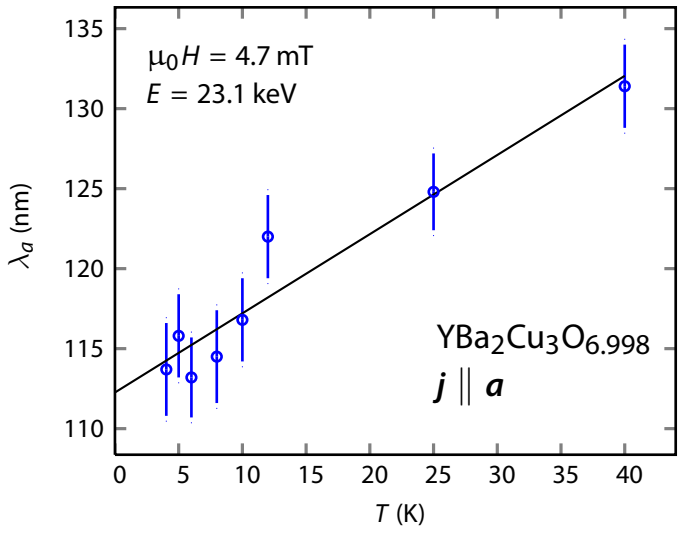

Figure 4.15 : Temperature dependence of magnetic penetration depth below 40 K. The muon beam energy for this set of runs is E = 23.1 keV and an external field of 4.7 mT is applied parallel to b-axis. A linear fit of $\lambda_a(T)$ yields $\lambda_a(0\,\mathrm{K})$ = 112.26(146) nm and $\left(\Delta\lambda/\Delta T = 0.495(78)\ \mathrm{nm\,K^{-1}}\right)$.

fits.

Using the phenomenological models equations (4.11a), (4.11b) and (4.12) introduced in the previous section, figures 4.16 and 4.17 shows the temperature dependence of penetration depths, $\lambda^{-2}(T)$ and normalized superfluid density, respectively. The penetration depths are measured by

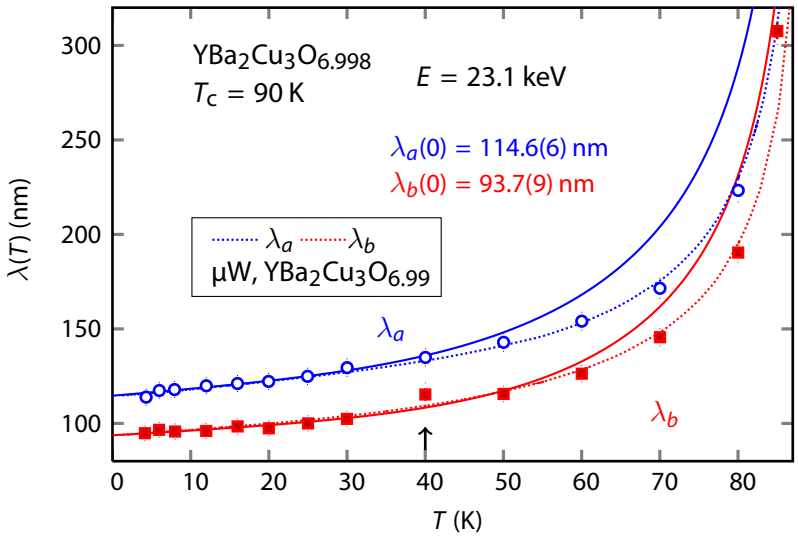

Figure 4.16 : Temperature dependence of the magnetic penetration depth $\lambda(T)$ for the two crystal orientations in at 23.1 keV implantation energy. The solid lines are fits to the (4.10) with a pure $d_{x^2-y^2}$-wave order parameter symmetry, of the temperature region $0 \leq T \leq 40$ K (↑). However, unlike in figure 4.9 the penetration depths are measured by keeping the phase fixed to 23.1° (cf. table 4.2). Penetration depth data from microwave (μW) measurements [172, 173], shifted to agree to the $\lambda_{a/b}(0\,\mathrm{K})$ from the $d_{x^2-y^2}$-wave phenomenological fits, are also shown. Interestingly, microwave data agree with LE-μSR measurements for the entire temperature range upto T_c. This is unlike the scenario in $YBa_2Cu_3O_{6.92}$ (cf. figure 4.9) where the agreement, between our data and microwave measurements, is observed for $0 \leq T \leq 50$ K. Vortices most likely entered in $YBa_2Cu_3O_{6.92}$ for $T > 55$ K.

keeping the phase fixed to 23.1° (cf. table 4.2). In the temperature dependence of $YBa_2Cu_3O_{6.92}$ (cf. figure 4.9), phases for individual temperature measurements were kept free. This method of a common phase is employed to limit the correlation between phase and frequency at the low magnetic field of $\mu_0 H = 4.7$ mT. Theoretical fits to a $d_{x^2-y^2}$-gap are obtained for $T \leq 40$ K ($\mu_0 H \sim H_{c1}(80\,\mathrm{K})$). The zero temperature energy gaps are found as $\Delta_{0,d,a} = 19.7(13)$ meV $= 2.53(17)\, k_B T_c$ and $\Delta_{0,d,b} = 23.4(43)$ meV $= 3.01(55)\, k_B T_c$ - yielding a gap anisotropy 0.84(16). Fits to the microwave(μW) data yields $|\Delta_a/\Delta_b| = 2.71\, k_B T_c / 2.70\, k_B T_c = 1.00$. The μSR gap values are higher than the weak coupling prediction as was observed in $YBa_2Cu_3O_{6.92}$, whereas the gap anisotropy is close to other measures of gap anisotropy in YBCO. Although the gap anisotropy in this section is consistent with some other measurements, there is a large uncertainty in the measured value primary due to λ_a^{-2} not being a very good fit to a $d_{x^2-y^2}$-gap model.

Results reported in this section are summarized in the table 4.2 and figure 4.18. It is interesting to note that the **dead layer** d (the layer close to the surface of the crystals where supercurrent is suppressed) varies between 15 nm to 17 nm; whereas in $YBa_2Cu_3O_{6.92}$, it was found

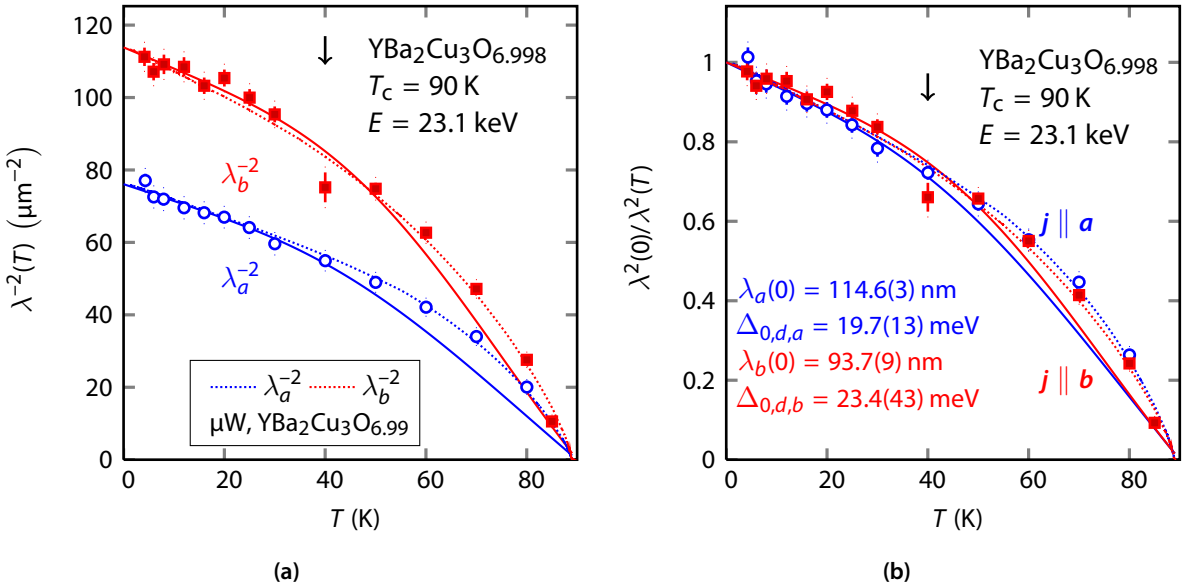

Figure 4.17 : (a) Temperature dependence of λ_a^{-2} and λ_b^{-2} (b) Normalized superfluid density. Penetration depth data from microwave measurements [172, 173], shifted to agree with the $\lambda_{a/b}(0\,\mathrm{K})$ from the $d_{x^2-y^2}$-wave phenomenological fits, are also shown.

Table 4.2 : Summary of results for $YBa_2Cu_3O_{6.998}$: Measured magnetic penetration depth in external fields of 4.7 mT and 9.5 mT are shown, for "phase individual" and "phase shared" models. Note, there is some φ-dependence (which contributes to the systematic uncertainty) of measured penetration depths. It's interesting to note that the "dead layer" d is within 10 nm to 20 nm indicating that it is a temperature and magnetic field invariant quantity. The shared phase for 4.7 mT measured is ~ 25° and slightly higher for the data at 9.5 mT. The χ^2/DF is slightly less for "individual phase" models, which indicates better fits.

B (mT)	T (K)	d (nm)	φ (°)	λ_a (nm)	λ_b (nm)	$\mathcal{R} \equiv \lambda_a/\lambda_b$	χ^2/DF
4.66	4	14.8(9)	27.0(16)[a]	115.6(18)	∅	∅	1.323
			25.9(13)[b]	119.2(24)	∅	∅	1.385
4.67	5	17.2(15)	27.0(16)[a]	107.5(39)	84.0(35)	1.28(2)	1.257
			23.0(13)[b]	114.2(26)	92.7(22)	1.23(1)	1.382
4.66	12	16.8(6)	27.9(15)[a]	117.2(25)	87.7(21)	1.34(3)	1.448
			25.4(6)[b]	120.3(18)	93.9(14)	1.28(1)	1.586
9.49	5	16.5(8)	31.1(20)[a]	∅	91.9(22)	∅	1.105
			30.1(16)[b]	∅	94.4(17)	∅	1.135

[a] Average of energy specific phases from "individual phase" analysis.
[b] Global phase from "shared phase" analysis.

to be 10.3 nm. Regardless of the temperature, oxygen doping and applied external magnetic field, there seems to be a thin outside layer on the order of 10 nm where the shielding currents are suppressed compared to a simple London model. Regardless of the **phase models**, the determination of phase is not very sensitive to whether we have data along both axis or just one axis. Determination of phase is important since the fitted values of $\lambda_{a/b}$ depends on whether we allow for individual phases or assume a common phase for the whole energy scan. To discern between phase and frequency (and thereby average field), more oscillations in the signal is better, which happens closer to the surface. Deeper in the sample, field drops by a significant fraction and thereby the frequency decreases which results in the phase and the average frequency being somewhat correlated. Nevertheless it is important to note that the correlation between φ and ω has less effect on global parameters such in d and $\lambda_{a/b}$ as they are determined from a range of implantation energies (i.e global fit). The fitted phases are found to be almost temperature independent, but vary weakly with applied magnetic field, as φ increases $\sim 5°$ if the applied field is doubled. With the mosaic of $YBa_2Cu_3O_{6.92}$, the global φ was found to be 33.0(8) at an external magnetic field of 9.5 mT. While the origin of dependence of phase on applied magnetic field remains to be understood, the determination of the magnetic penetration depths $\lambda_{a/b}$ and their ratio $\mathcal{R}$ can still be determined with a few percent uncertainty. With our simple model of the magnetic penetration depth, the dead layer d and penetration depths $\lambda_{a/b}$ are inversely correlated, such that as d increases, $\lambda_{a/b}$ decreases. However, the ratio $\mathcal{R}$ is insensitive to the variations just mentioned and thereby is more robust and less susceptible to systematic effects. Although measured at finite temperatures (4 K, 5 K and 12 K), we expect $\mathcal{R}$ to be weakly dependent on temperature at low temperatures since it depends on the effective mass tensor.

As may be noticed the from table 4.2 and figure 4.18, the χ^2/DF depends on applied external magnetic field and only slightly on the (phase) model. The χ^2/DF also is smaller (better fit) for a fit with energy specific phases compared to a global phase. This is expected as more free (fit) parameters mean more degrees of freedom for the model and thus a better fit, however it introduces correlations among variables φ, σ and asymmetry. Nonetheless, statistical uncertainty in the "shared phase" model is better as χ^2/DF is inversely correlated with the number of parameters. Model dependent systematic uncertainties can be avoided if better measurements of the phase are done for a specific set of measurements. In the following section, we describe a better method to determine the phase, which avoids the uncertainty introduced by leaving it a free parameter. However, it should still be noted that any phase dependence of $\lambda_{a/b}$ introduces an additional error of the order of statistical uncertainty in either shared or independent phase global fits.

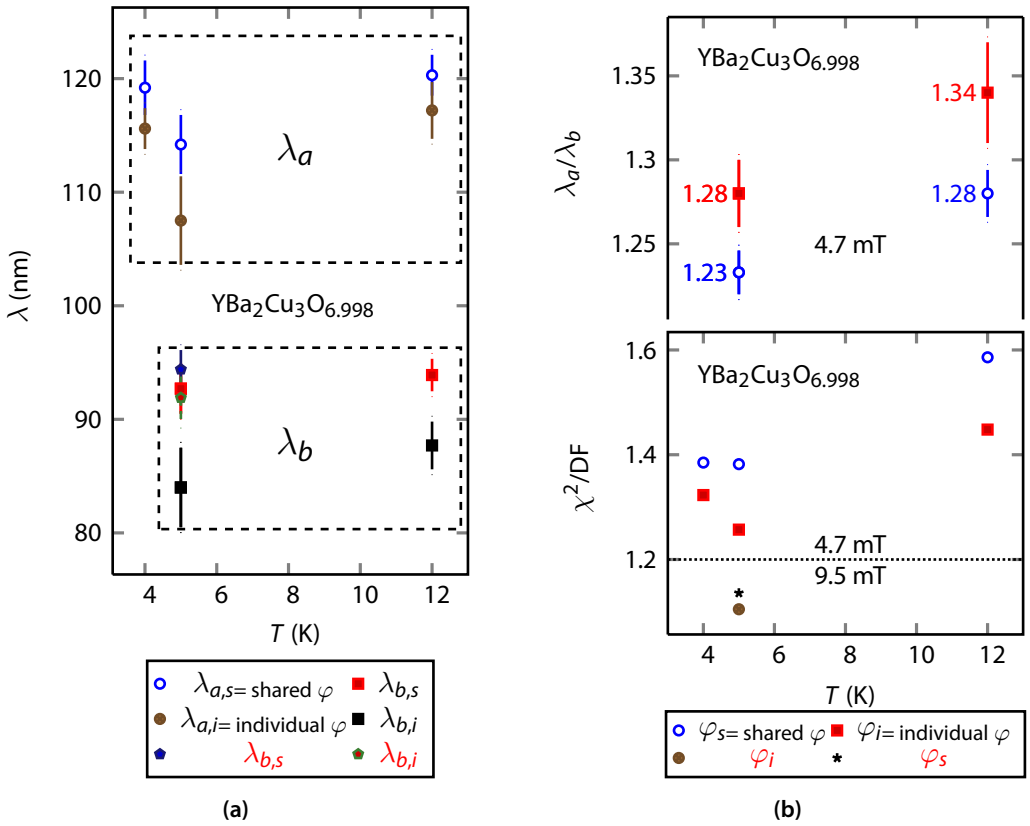

Figure 4.18 : Summary of results for $YBa_2Cu_3O_{6.998}$: Measured magnetic penetration depth in external fields of 4.7 mT and 9.5 mT are shown, for **individual(shared) phase** models. There is some φ-dependence (of the order of systematic uncertainty) of measured penetration depths. The λ_a/λ_b and χ^2/DF is slightly less for **individual phase**, which indicates better fits.

4.1.4 $YBa_2Cu_3O_{6.52}$

As has been discussed in the sections 4.1.1 and 4.1.3, statistical uncertainties in the determination of magnetic penetration depths $\lambda_{a/b}$ are on the order of a few percent. However, the **shared phase** vs **individual phase** models suggests one should add to this a systematic uncertainty of about 3 %. To have a simpler model having one effective phase (depending on when muon enters into sample and partially on other geometric factors), a novel method was used to determine φ. Two normal state runs were taken at a single field (to be determined from fit) but one of them having it's direction reversed. The resulting spectra is plotted in the figure 4.19. These normal

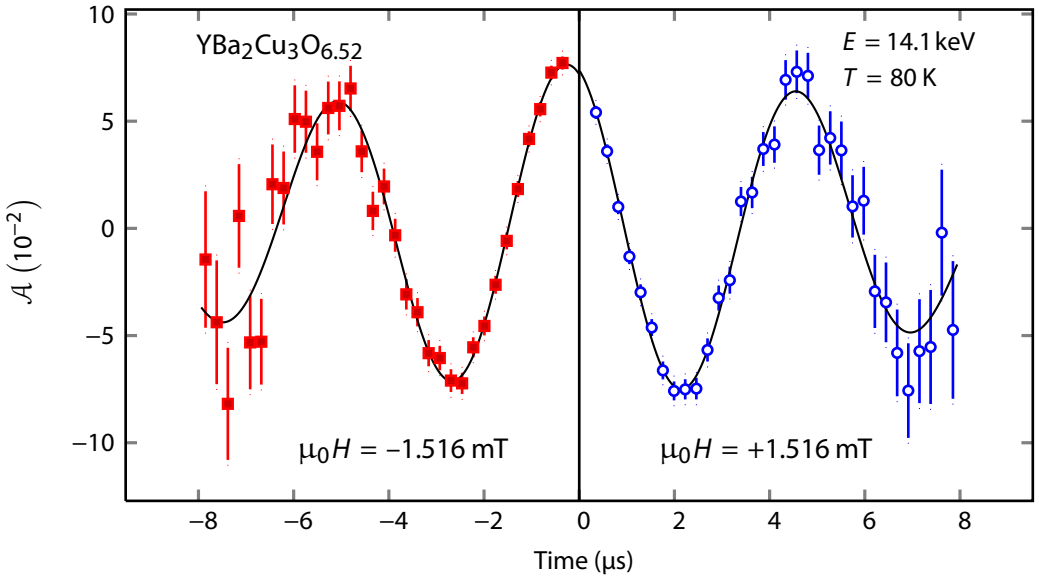

Figure 4.19 : $YBa_2Cu_3O_{6.52}$ in an applied field of 1.45 mT and −1.45 mT at 80 K. Field reversing is like taking a measurement in negative time. $\varphi = 19.8(10)°$ and $\sigma = 0.14(1)\ \mu s^{-1}$.

states runs were taken, as a standard procedure, *after* the superconducting state runs. Having a negative magnetic field $-B$ is nearly identical to having a precession in negative time, as

$$\omega t \equiv \gamma_\mu(-B)t = (\gamma_\mu B)(-t).$$

Combining the two precession signals as shown in figure 4.19 for negative and positive times allows one to, in effect, double the time window of observation and also to determine the phase unambiguously. The data in the normal state are fit to a damped cosine:

$$\mathcal{A}(t) \equiv A_0 \exp\left(-\sigma^2 t^2/2\right) \cos\left(\gamma_\mu \mu_0 H t + \varphi_0\right)$$

one can determine $\mu_0 H$, φ_0 and σ. The fitted values from figure 4.19 were found to be $\mu_0 H = 1.514(6)$ mT , $\varphi_0 = 19.8(10)°$ and $\sigma = 0.14(1)\ \mu s^{-1}$. This unique determination of phase is specially crucial at low field since, muon oscillation frequencies ($\omega = \gamma_\mu B$) are also lower and fewer

full oscillations are available, introducing a large correlation between φ and ω, in figure 4.20. Note the clear reduction in precession frequency (thereby, internal field) in figure 4.20 from nor-

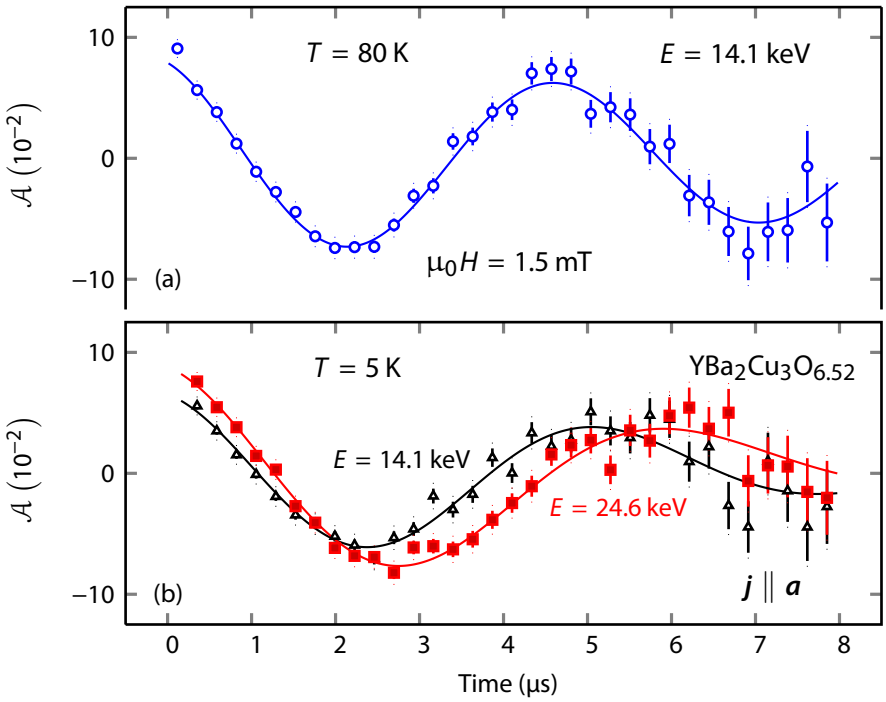

Figure 4.20 : Top: The muon spin precession signal in the normal state of $YBa_2Cu_3O_{6.52}$ at 80 K in an external field of 1.5 mT applied parallel to the *b*-direction. The mean implantation energy is $E = 14.1$ keV - which corresponds to a mean implantation depth of 65 nm. Bottom: The same conditions as above except in the superconducting state at $T = 5$ K with energy $E = 14.1$ keV and 24.6 keV .

mal state to superconducting states. It should be stressed that treating φ as a geometric parameter equal to the normal state phase is a deviation from the analyses done so far. However at such low magnetic fields this is the best option since the phase and frequency are so strongly correlated. Fixing φ to the normal state values yields a better estimate of average frequencies with only a slightly higher χ^2/DF. However, it may be noticed from table 4.3 that set of runs at 1.5 mT yields the lowest χ^2/DF as well. The phase determined for measurements at 7.8 mT is similar to the "field reversed" method while the phase in 4.6 mT set of runs is estimated from interpolating the phases in 1.5 mT and 7.8 mT set of measurements, assuming linear variation of phase with applied field.

The fitted broadening parameter, σ, as a function of energy, obtained from the global fit, is shown in figure 4.21 for $\mu_0 H = 1.5$ mT, 4.6 mT and 7.8 mT. At 1.5 mT, σ is almost independent of implantation energy, except close to the surface - where there appears to be an upturn in the higher magnetic field. This suggests there may be some vortex penetration near the surface which would lead to a field distribution which is broader than expected from just the stopping distribution $\rho(z)$ alone. One possible explanation is that vortices enter close to surface which

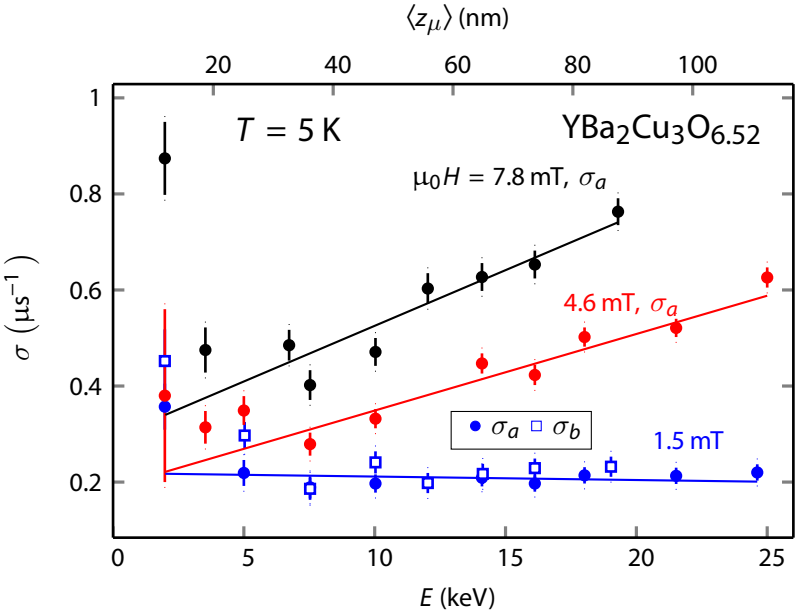

Figure 4.21 : $YBa_2Cu_3O_{6.52}$ broadening parameter are shown for an external applied field of 1.45 mT, 4.6 mT and 7.8 mT such that the shielding currents are flowing in the *a* direction ($\boldsymbol{j} \parallel \boldsymbol{a}$). The common parameters are λ_a, λ_b and d. The upturn in σ at lower energies are possibly due to vortex entrance close to the surface. The solid lines are guides to the eye.

would introduce broadening in the magnetic field while maintaining an average field close to the external applied field. Deeper in the sample, the diamagnetic shift is larger and therefore, $\sigma(E) \propto E$ - seen in the measurements at 4.6 mT and 7.8 mT (cf. figure 4.22).

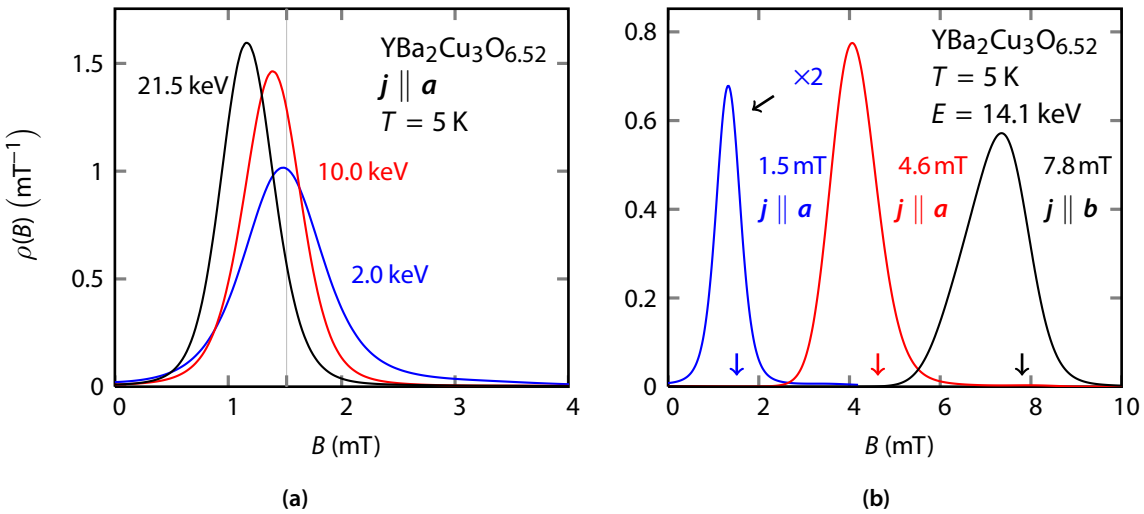

Figure 4.22 : Maximum-entropy magnetic field distribution, in $YBa_2Cu_3O_{6.52}$, at various implantation energies and at T = 5 K in an external applied magnetic field ($\mu_0 H$) of (a) 1.5 mT and (b) 4.6 mT applied parallel to the *b* axis. The arrows (↓,↓,↓) in (b) indicate the applied external fields for the corresponding ME field ($\mu_0 H$) distributions.

The superconducting state runs at 1.5 mT were fit to the London model, as described earlier,

yielding global fit values for $\lambda_{a/b}$ and dead layer d. The corresponding global and individual average magnetic fields are shown in the figure 4.23a. As before the difference between the the

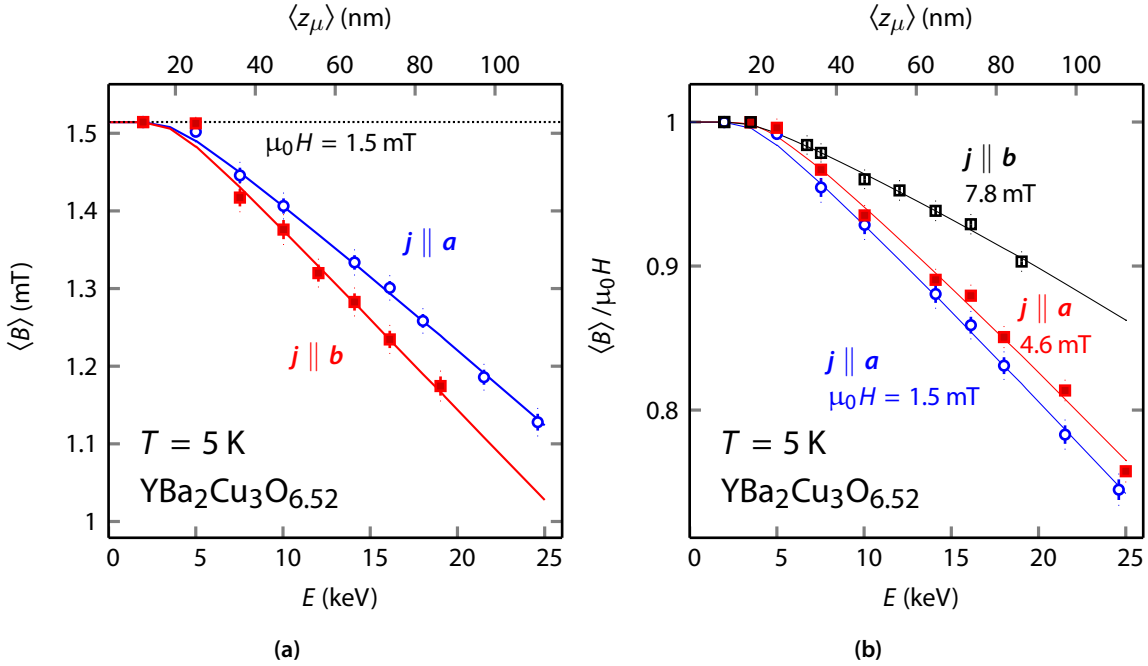

Figure 4.23 : (a) The average magnetic field $\langle B \rangle$ versus energy (mean stopping depth) in an applied field of 1.45 mT such that the shielding currents are flowing in the a direction ($j \parallel a$, open circles) and b direction ($j \parallel b$, filled squares). (b) Relative average local magnetic field with respect to the applied field as a function of muon implantation energy for the two fields of 4.7 mT and 9.5 mT applied parallel to the b axis of the $YBa_2Cu_3O_{6.52}$. The depicted fields have been calculated in the same way as in figure 4.7 and normalized to the applied fields.

global fit and the individual points reflects how well the data at individual energies agrees with the global fit. A comparison of the relative average magnetic field as a function of energy for 1.5 mT, 4.6 mT and 7.8 mT is shown in the figure 4.23b. It is evident that the lowest $\lambda_{a/b}$ for this sample results from the 1.5 mT set of runs. As may be noticed the average field ($\langle B \rangle$) in the figure 4.23 doesn't drop until ~ 5 keV, corresponding to an implantation energy ~ 25 nm which is also reflected in the dead layer d in the table 4.3. One interesting phenomenon consistently seen in all analysis is that the d is between 10 nm to 25 nm, irrespective of the external field magnitude $\mu_0 H$ or orientation, suggesting that some intrinsic mechanism being responsible for the reduced supercurrent close to the surface.

To extract $\lambda_{a/b}$ (0 K), temperature dependent measurements of penetration depths have been obtained as shown in the figure 4.24. It may be noticed that at low temperatures, λ is linear only at the external field of 1.5 mT. The non-linear behavior in 4.6 mT is likely due to vortex penetration. This is consistent with the fact that $\sigma(E)$ increases almost linearly, with energy, as shown in the figure 4.21. Note the unusual temperature dependence of $\lambda_a(T)$ in the 4.6 mT set of measurements. These prompted us to make measurements at a significantly lower magnetic field of 1.5 mT. The resulting $\Delta\lambda/\Delta T = 6.30(96)\,\mathrm{nm\,K^{-1}}$ from the 1.5 mT temperature dependence

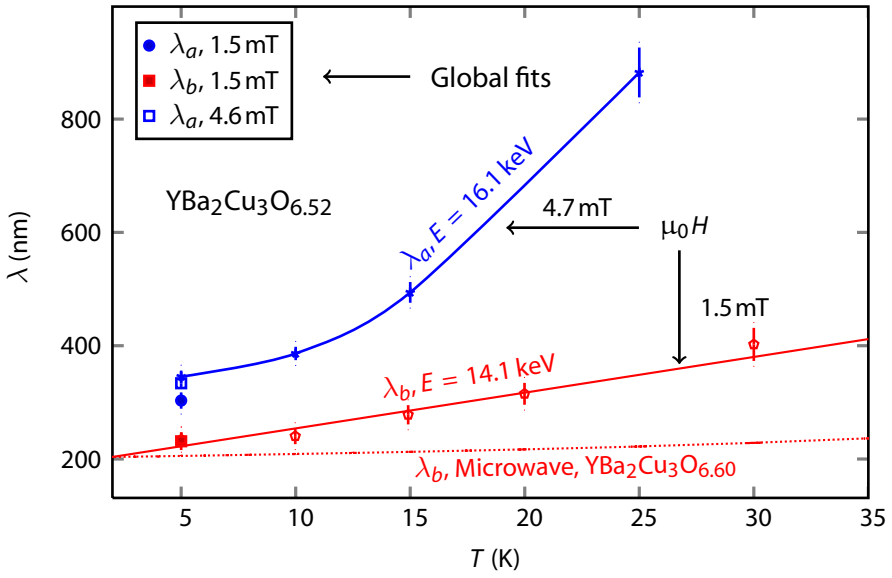

Figure 4.24 : As may be noticed, λ sharply increases with temperature at $\mu_0 H = 4.6$ mT. Possible entrance of vortices is likely the reason of increase of "effective λ". This prompted us to take low field (1.5 mT) set of runs. The fit parameters at 1.5 mT external field are, $\lambda_a(0\,\mathrm{K}) = 191.0(134)$ nm. $\Delta\lambda/\Delta T = 6.30(96)\,\mathrm{nm\,K^{-1}}$. The slope is an order of magnitude bigger than that found in other oxygen dopings of YBCO. Penetration depth data from microwave measurements [172, 173], shifted to agree with the $\lambda_b(2\,\mathrm{K})$ from the linear fit, is also shown. As may be noticed clearly, $\Delta\lambda/\Delta T$ in our data is significantly higher than the slope $\left(\sim 0.82\,\mathrm{nm\,K^{-1}}\right)$ from microwave data. The difference may be partly due to the difference in oxygen concentration (O=6.52 vs O=6.60). Measurements in even lower magnetic fields ($\sim$ 0.5 mT) may be needed to compare $\Delta\lambda/\Delta T$ in the two methods.

has been used to extrapolate $\lambda_b(5\,\mathrm{K})$ to $\lambda_b(0\,\mathrm{K})$. Although $\lambda(T)$ is linear at low temperatures, the slope $\Delta\lambda/\Delta T$ is an order of magnitude larger compared to the other two oxygen dopings of O=6.998 and O=6.92. It suggests that measurements at even a lower field may be required to test if the value at 1.5 mT is intrinsic. The magnetic penetration depth in the other orientations $\lambda_a(0\,\mathrm{K})$ has been obtained using the equation

$$\lambda_b(0\,\mathrm{K}) = \frac{\lambda_a(0\,\mathrm{K})}{\mathcal{R}}, \tag{4.13}$$

where $\mathcal{R}$ is the ratio of penetration depths measured at 5 K.

Figure 4.25a shows effective penetration depth λ_b's dependence on external field. The phase was left fixed at the respective normal state values. As argued before, data taken at the higher fields ($>$ 1.5 mT) may involve vortex penetration and obtained λ_a should be regarded as an effective penetration in the presence of vortices. Note that the effective λ_as from the global fit (figure 4.23) involving many energies are much more reliable than those in figure 4.25a which are obtained using the spectrum at a single energy. Nevertheless, the almost linear field dependence is strong evidence for vortex penetration at the higher fields. This is not too surprising for $x = 6.52$ since the lower critical field is expected to be much smaller than in the $x = 6.92$

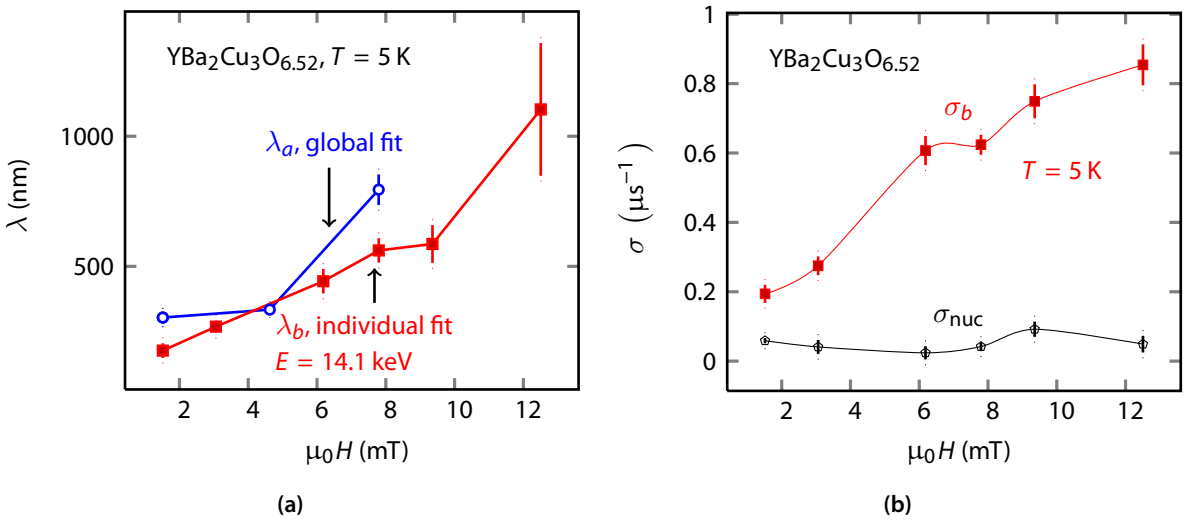

Figure 4.25 : (a) Single measurements of effective penetration depths in various external magnetic fields are shown here. The almost linear rise in λ_b with magnetic field stresses that lower external field must be used and also be made sure that the samples are indeed in the Meissner state. (b) The rise of σ with $\mu_0 H$ indicates broadening of field distribution due to vortex penetration.

Table 4.3 : Summary of results in $YBa_2Cu_3O_{6.52}$: Measured magnetic penetration depths at 5 K are shown. The errors reported here are just statistical errors. An additional (~ 2 nm) error is due to uncertainty in stopping distribution. The lowest penetration depths were obtained for both *a* and *b* axis in 1.5 mT external field. The penetration depths at higher fields of 4.6 mT and 7.8 mT include contributions from vortices entering the sample, as may be observed from $\sigma \propto E$ (see figure 4.21) at higher energies. In this sense, they are an effective penetration depth in the presence of vortices.

B (mT)	T (K)	d (nm)	φ (°)	λ_a (nm)	λ_b (nm)	$\mathcal{R} \equiv \lambda_a/\lambda_b$	χ^2/DF
1.52	5	22.9(2)	19.8(10)[a]	303.2(144)	231.3(155)	1.31(6)	0.999
4.63	5	27.0(12)	22.0(13)[b]	333.7(99)	∅	∅	1.117
7.79	5	22.9(2)	24.1(16)[a]	∅	605.7(165)	∅	1.075

[a] Measured via reversing of field.
[b] Interpolated.

or $x = 6.998$ sample. Also, it may be noted from figure 4.25b, the broadening parameter σ increases with $\mu_0 H$. This also corroborates our assertion that vortices are present in all other measurements except possibly at 1.5 mT. Although the single fit λ_bs in figure 4.25a are not very reliable, they serve to emphasize that caution must be taken to measure the magnetic penetration depth in the Meissner state in a low enough field to be sure there is no vortex penetration. Otherwise, λ obtained is some effective penetration depth which depends on the degree of vortex penetration at the edges.

From the measured $\lambda_{a/b}$ in table 4.3, it is very likely only minor vortex penetration happened in 4.6 mT set of runs whereas a significant number of vortices (cf. asymmetric $\rho(B)$ in figure 4.22) entered in a 7.8 mT set of runs, making the global λ very long.

4.2 $Ba(Co_{0.074}Fe_{0.926})_2As_2$

In this section, we present measurements of the magnetic field profile and magnetic penetration depth on single crystals of $Ba(Co_{0.074}Fe_{0.926})_2As_2$. In the current study, we measure the field profile directly on a freshly cleaved surface of $Ba(Co_{0.074}Fe_{0.926})_2As_2$ using the modified London model as described in the section 4.1.1. The single crystal of optimally-doped $Ba(Co_{0.074}Fe_{0.926})_2As_2$ was grown using a self-flux method [179]. The crystal was approximately square-shaped with dimensions 5.6 mm × 4.5 mm × 0.3 mm and exhibited a transition at T_c = 21.7 K as measured by SQUID magnetometry (figure 4.26). The crystal was cleaved to a thickness of about 0.3 mm

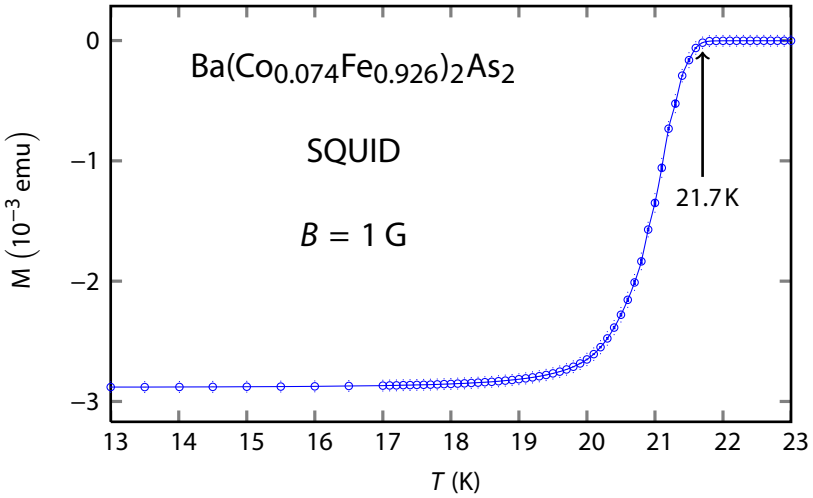

Figure 4.26 : Data from O. Ofer: Magnetization of $Ba(Co_{0.074}Fe_{0.926})_2As_2$ as a function of temperature, showing that the superconducting transition starts at T_c = 21.7 K.

under flowing N_2 gas just prior to loading it into the ultra-high-vacuum sample chamber.

Figure 4.27 shows typical μSR precession signals obtained in a 4.7 mT field applied parallel to the *ab* face of the crystal. The top panel shows the precession signal in the normal state where the mean internal field is equal to the applied field obtained via fitting the spectrum to a Gaussian damped precession signal. The normal state at $\mu_0 H$ = 4.7 mT yields σ of 0.12 μs^{-1}. Signals taken below T_c are shown in the bottom panel. All the measurements in the Meissner state were made in **zero field cooled** method as detailed earlier. The reduction of precession frequency, for a higher muon implantation energy, is clearly visible comparing the two spectra (▵ and ■) in the figure 4.27. The broadening parameters obtained in the superconducting state are shown in the figure 4.28. The $\langle\sigma\rangle$ in the Meissner state of $\mu_0 H$ = 4.7 mT is slightly higher (0.28(1) μs^{-1}) than that (0.21(1) μs^{-1}) corresponding to that obtained at $\mu_0 H$ = 2.5 mT. The increase of σ with external field may be due to demagnetization effects, arising from a slight misorientation of the field with respect to *a* – *b* plane. Any bulk demagnetization effect is linearly dependent to the external field. However, the present pnictide sample is a single crystal. The additional (not accounted for by the stopping distribution $\rho(z)$) broadening increases by only ~ 25 % with the

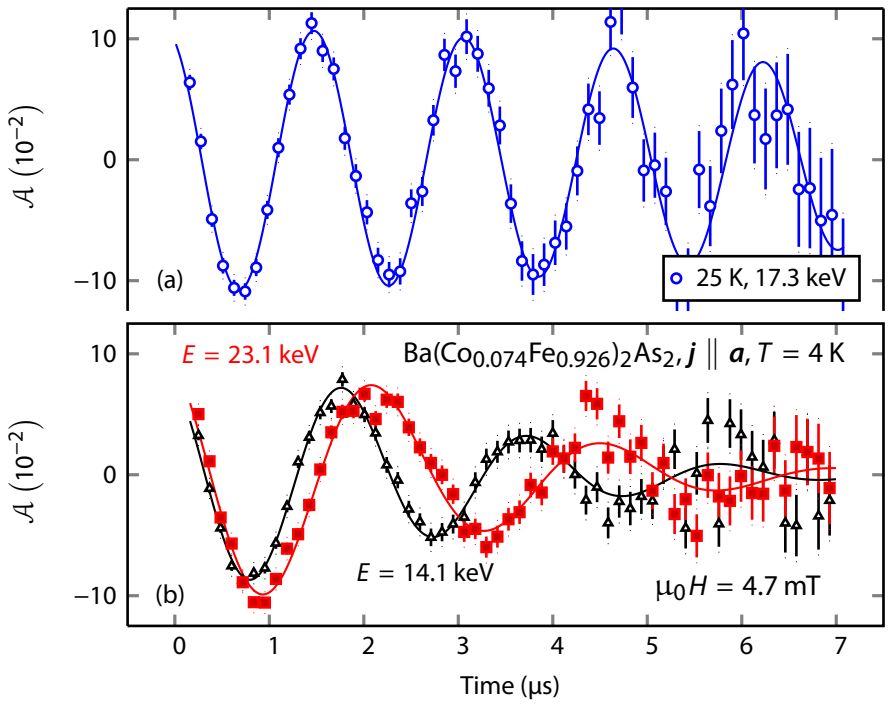

Figure 4.27 : Muon precession signals in $Ba(Co_{0.074}Fe_{0.926})_2As_2$ in an applied field of $\mu_0 H = 4.7$ mT. (a) In the normal state at $T = 25$ K. (b) In the superconducting state at $T = 4$ K with $E = 14.1$ keV and $E = 23.1$ keV.

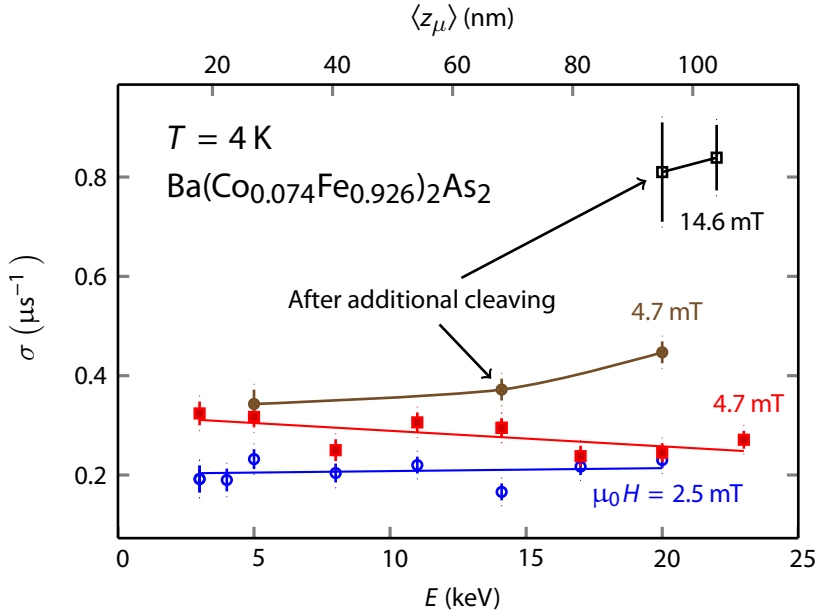

Figure 4.28 : Broadening parameter (σ) in $Ba(Co_{0.074}Fe_{0.926})_2As_2$ in external applied fields of $\mu_0 H = 2.5$ mT and $\mu_0 H = 4.7$ mT. The solid lines are guides to the eye.

approximate doubling of $\mu_0 H$. Also it may be noted from the figure 4.28, that σ does not increase sharply close to the surface as has been seen previously in the two YBCO mosaics shown in the figures 4.13 and 4.21. This suggests that there are no vortices close to the surface and yet there is a suppression of superfluid density ~ 15 nm, close to the sample surface, as may be seen from the curvatures of the global fits in the figure 4.29.

Figure 4.29 shows the average local field $\langle B \rangle$ as a function of the beam energy at $T = 4$ K. The data are consistent with an exponential decrease as a function of increasing depth or implantation energy, as expected from a London model. The global fit parameters are $\lambda(T = 4\,\text{K}) =$

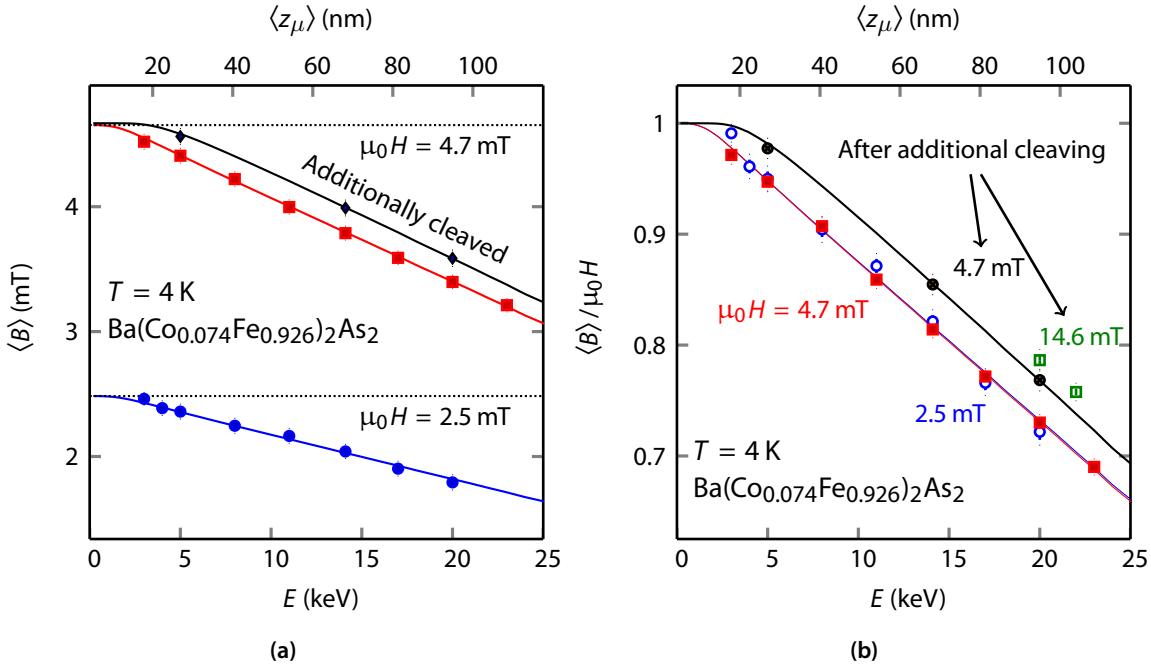

Figure 4.29 : (a) The average magnetic field versus the muon energy at $T = 4$ K with $\mu_0 H = 2.5$ mT, 4.7 mT and 14.6 mT. The dotted line indicate the applied field and the solid line indicates a fit to (2.18). (b) Relative average magnetic field in the above mentioned external fields. Notice that there is little field dependence of λ - measured in 2.5 mT and 4.7 mT; however, after additional cleaving (——), the deadlayer seems to get larger (~ 27 nm). This suggests that d is not due to demagnetization - which would have predicted a smaller d for a thinner sample. The average magnetic field in 14.6 mT possibly includes significant vortex contribution (cf. figure 4.30b).

251.7(19) nm and $d = 14.5(9)$ nm where the uncertainties are purely statistical. There is also a 3 % systematic uncertainty in λ due to uncertainties in the muon stopping distribution. Similar results were obtained at a magnetic field of 2.5 mT, where $\lambda = 252.2(45)$ nm, indicating there is little field dependence in λ, which is also reflected in the $\langle B \rangle$ in the figure 4.29b. Results of analyses done on two phase (**independent and shared**) models are shown in the table 4.4. Notice that the average of phases from **individual phase** is within ~ 1°, while **shared phase** yields a ~ 3°. Yet with all the model dependence of A_0, σ and φ, there is only ~ 2 nm difference in the measured λ in the external fields of 2.5 mT and 4.7 mT. This suggests the robustness of our

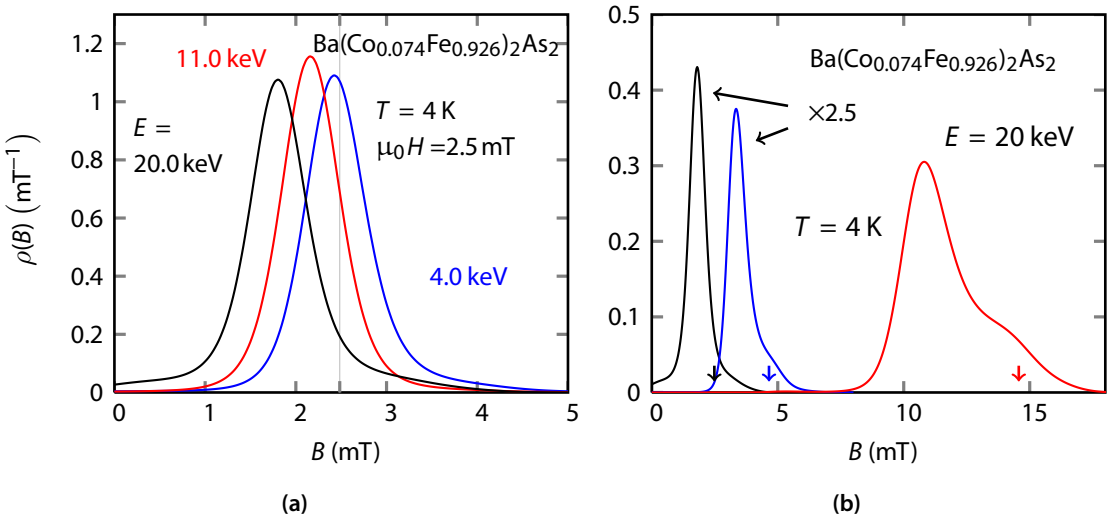

Figure 4.30 : (a) Magnetic field distribution as seen by muons at various implantation energies and at $T = 5$ K in an external applied magnetic field $(\mu_0 H)$ of 2.5 mT, applied parallel to the *ab* plane. (b) Same as in (a) except field distributions are shown for $\mu_0 H = 2.5$ mT, 4.7 mT and 14.6 mT, indicated by the respective arrows (↓,↓,↓).

Table 4.4 : Measured London penetration depths at 4 K are shown. The errors reported here are just statistical errors. An additional (~ 2 nm) error is due to uncertainty in stopping distribution.

	4.7 mT			2.5 mT		
State	λ (nm)	$\varphi(^\circ)$	χ^2/DF	λ (nm)	$\varphi(^\circ)$	χ^2/DF
Normal	–	25.5(18)	0.932	–	21.4(17)	0.972
Superconducting	252.8(19)	30.9(12)[a]	1.118	254.5(41)	27.6(7)[a]	1.030
	251.7(19)	28.3(6)[b]	1.052	252.2(45)	27.8(5)[b]	1.029
Superconducting and cleaved	254.4(52)	27.9(9)[a]	1.198			
	253.9(51)	27.5(2)[b]	1.178			

[a] Global phase from **shared phase** analysis.
[b] Average of energy specific phases from **individual phase** analysis.

method in obtaining the absolute London penetration depth in this pnictide.

The temperature dependence of λ measured with LE-μSR (■) and with μW (——), MFM (○) and tunnel-diode-resonator (TDR) (——) are shown in the figure 4.31. The data points were obtained with a single energy of 21.3 keV with d fixed to the value determined from the global fit at $T = 4$ K (see figure 4.29). Note the temperature dependence of λ at low temperatures is similar to recent TDR results [180] on a thin sample but considerably weaker than previous studies on thicker crystals [181]. This suggests early studies may have been affected by an anomalous temperature-dependent field penetration from the *c*-axis edges. It is interesting to note that all of these results are stronger than found by MFM also shown in figure 4.31 [182]. However, there are recent published results showing agreement between TDR and MFM [183]. One difference is that the present measurements, as well as previous TDR results, measure an average over the

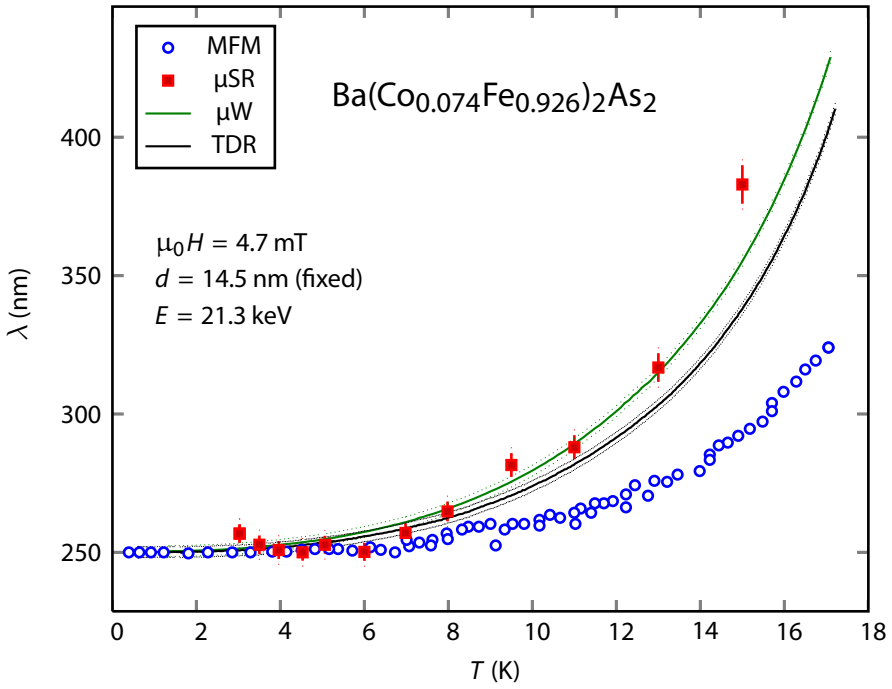

Figure 4.31 : The temperature dependence of λ plotted versus $t = T/T_c$. The red squares (■) are measurements of the absolute value of λ from LE-μSR whereas the green line (——) are from microwave cavity perturbation on a piece of the same crystal shifted to overlap with the LE-μSR at low temperature. For comparison, we also show recent TDR (——) and MFM (○) results for $\Delta\lambda$, all shifted to agree at $T = 0$ K.

surface whereas MFM is a point-like probe. Such differences between methods and crystals indicate there are considerable variations in the spectrum of low energy excitations depending on doping and/or surface quality.

In conclusion, we have investigated the absolute value of the magnetic penetration depth in the Meissner state of freshly-cleaved $Ba(Co_{0.074}Fe_{0.926})_2As_2$ using LE-μSR. The absolute value of λ extrapolated to $T = 0$ is 250(8) nm, where most of this uncertainty originates from the muon stopping distribution. There is no evidence of sharp rise in field broadening close to the sample surface. Also there is weaker field dependence of σ which may have a different origin other than bulk magnetization effect. It has been reported that a two-gap *s*-wave model and a weak power law model describes the temperature dependence of the superfluid density equally well [184]. The latter model is characteristic of any non *s*-wave gap.

4.3 Summary of Results

Table 4.5 shows the summary of measured London penetration depths, extrapolated to $T = 0$ K, for three oxygen dopings of $YBa_2Cu_3O_{6+x}$. The first column is the measured $\lambda_{a,b}$ extrapolated to $T = 0$ K. The error in brackets is the statistical uncertainty and the second error is an estimate of the systematic uncertainty. For comparison, $\lambda_{a,b}$ values from other techniques are also given.

In $YBa_2Cu_3O_{6.92}$, "individual phase" and "shared phase" models yield $\lambda_{a,b}$ within a nm of

each other and the anisotropies are the same. This implies that there is little dependence on the model used to fit the data. The λ_{ab} values obtained here are in good agreement with bulk μSR measurement in vortex state extrapolated to zero field. It may be noted that conventional μSR is very different type of measurement done in the presence of vortices. The λ_{ab} in $YBa_2Cu_3O_{6.92}$ obtained here is shorter than that obtained in a thin film. The difference is understandable considering the measurement in the film was done at 20 K and the T_c of the film (87.5 K) is less than in crystals possibly indicating a different doping level than in crystals.

Row two of table 4.5 represent our results of $\lambda_{a,b}$ in Ortho-I $YBa_2Cu_3O_{6.998}$, measured at 5 K and 4.7 mT, extrapolated to 0 K by the method described above. Note, there is very close agreement between our result and ESR on Gd-doped Ortho-I $YBa_2Cu_3O_{6.95}$ [185].

Row three of table 4.5 represent our results of $\lambda_{a,b}$ in $YBa_2Cu_3O_{6.52}$, measured at 5 K and 1.5 mT, extrapolated to 0 K. $\lambda_{a,b}$'s were measured in 1.5 mT, 4.7 mT and 7.8 mT. However, at the higher magnetic fields of 4.7 mT and 7.8 mT the unusual temperature dependence is clear evidence for vortex penetration. In 1.5 mT external field, a unique determination of phase was made by reversing the field, essentially doubling the range of muon polarization's oscillation time. Determination of the phase is crucial especially at low field since the frequency is low and very few full oscillations are observed in the the muon polarization. It is also interesting that the low temperature linear dependence of λ in $YBa_2Cu_3O_{6.52}$ is an order of magnitude

Table 4.5 : Measurements of the absolute value of the magnetic penetration depth $(\lambda_{a,b})$ in $YBa_2Cu_3O_{6.52}$, $YBa_2Cu_3O_{6.92}$ and $YBa_2Cu_3O_{6.998}$. Average magnetic penetration depth $\lambda_{ab} = \sqrt{\lambda_a \lambda_b}$. Vortex state measurements are quoted without systematic errors.

λ_a (nm)	λ_b (nm)	λ_{ab} (nm)	λ_a/λ_b	Comment
125.6(17) ± 3	105.5(11) ± 3	115.1(10) ± 3	1.19(1)	$YBa_2Cu_3O_{6.92}$ [a]
105.0(39) ± 3	82.0(33) ± 3	92.8(26) ± 3	1.28(2)	$YBa_2Cu_3O_{6.998}$ [a]
261.7(212) ± 3	199.8(162) ± 3	228.7(131) ± 3	1.31(6)	$YBa_2Cu_3O_{6.52}$ [a]
		118.0(4)		μSR in vortex state[b] [124]
		146(3)		LE-μSR in thin film at 20 K [169]
160	100	126.5	1.6	IR reflectivity at 10 K [111]
103(8)	80(5)	91(7)	1.29(7)	ESR on Gd-doped $YBa_2Cu_3O_{6.995}$ [185]
202(22)	140(28)	168(19)	1.4(3)	ESR on Gd-doped $YBa_2Cu_3O_{6.52}$ [185]
		150(10)	1.16(2)	μSR at 10 K [186]
		138(5)	1.18(2)	SANS at 10 K [187]

[a] This work

[b] Conventional μSR

Table 4.6 : Measurements of the absolute value of the magnetic penetration depth $(\lambda_{a/b})$ in $Ba(Co_{0.074}Fe_{0.926})_2As_2$. Average magnetic penetration depth $\lambda_{ab} = \sqrt{\lambda_a \lambda_b}$.

λ_{ab} (nm)	Comment
250.0(26) $\pm$ 5	$Ba(Co_{0.074}Fe_{0.926})_2As_2$ [a]
325(50)	MFM [182] in $Ba(Co_{0.05}Fe_{0.95})_2As_2$
190(10)	Estimated for a range of dopings in $BaCo_xFe_{2-x}As_2$ [188]
250(36)	MFM [189] on $Ba(Co_{0.074}Fe_{0.926})_2As_2$

[a] This work

higher than those found in other two oxygen dopings. Note that λ_{ab} in LE-μSR is significantly longer than that measured with ESR on Gd-doped $YBa_2Cu_3O_{6.52}$. This is surprising considering the other two oxygen dopings have produced very similar results. It would be interesting to do measurements at even lower magnetic fields with low energy μSR to see if the λ is in closer agreement with the ESR results.

The first row in table 4.6 gives the measured λ_{ab}, extrapolated to 0 K for the pnictide. Measurements were done in external field of 2.5 mT and 4.7 mT. The λ_{ab} s obtained for both external field in "shared phase" and "individual phase" models were within ~ 4 nm i.e, introducing ~ 2 % systematic uncertainty. There is broad agreement in the temperature dependence of λ between LE-μSR, TDR & μW, at least at this one Co concentration. However, the MFM results look significantly different. This method is unique in that it probes $\Delta\lambda$ on much smaller length scale. For comparison, some results from other methods, especially MFM are also shown. Among the MFM results, one experiment made on the exact same Co-doping as ours, yield the same λ, however with a much larger uncertainty.

Figure 4.32 shows the critical temperature versus $1/(\lambda_a\lambda_b)^{-1} = n_s/\sqrt{m_a^* m_b^*}$. A linear relationship between the two quantities was first suggested by Uemura *et al.* LE-μSR results significantly differ from a linear relationship. Recent ESR measurements on Gd-doped YBCO [185] arrived at the same conclusion - although, the measured penetration depths are somewhat different than this work. It is clear the true relationship seems to be sub-linear dependence of T_c on λ_{ab}^{-2}. The linear relationship has been widely regarded as an evidence of preformed Cooper pairs that form above T_c at a temperature T^*. The superconducting T_c occurs when the order parameter phases become coherent. Interestingly Bose-Einstein condensation in 3D also predicts a sub-linear relationship of T_c on λ_{ab}^{-2}. The sub-linear relationship of T_c versus λ_{ab}^{-2} is clear indication of other mechanisms being influential in determining T_c. One of the interesting aspects from figure 4.32 is that optimally doped cuprate and Co-doped pnictide almost falls on a straight line going through the origin to optimally doped YBCO. Measurements on a range of dopings will be needed to determine the exact relationship of T_c on λ_{ab}^{-2}. The dependence of the anisotropy (λ_a/λ_b) on O-doping in $YBa_2Cu_3O_{6+x}$ is very surprising. In $YBa_2Cu_3O_{6.995}$, $\lambda_c/\lambda_{ab} \sim 7.0$ [185] - which indicates this system is much more three dimensional BEC system

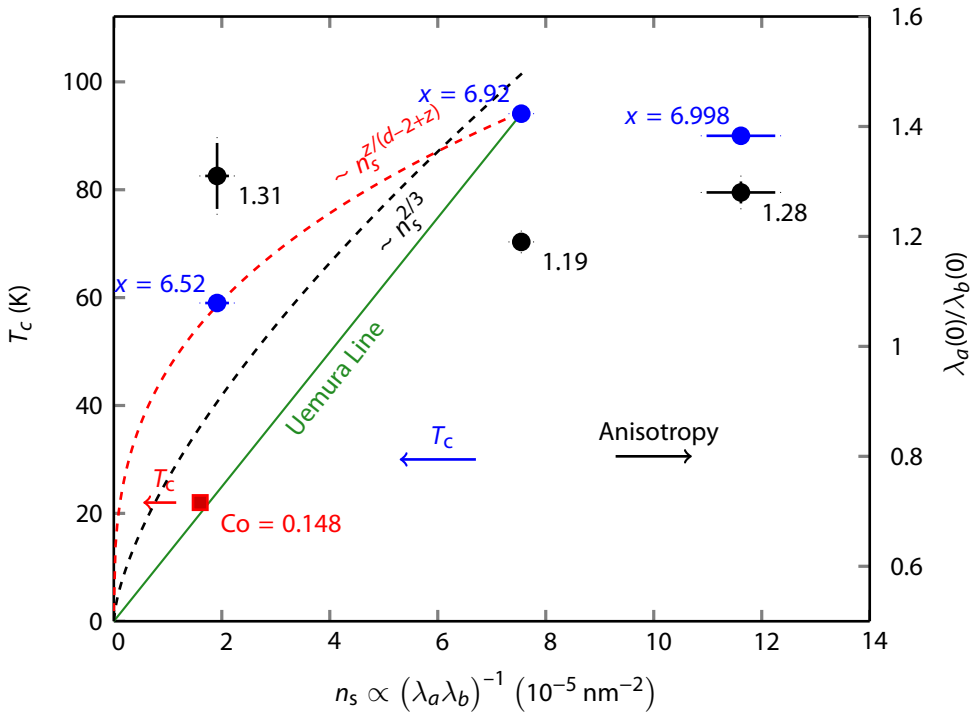

Figure 4.32 : T_c and anisotropy vs superfluid density n_s are shown. T_c vs n_s in YBCO (●) appears to be sub-linear. The theoretical models of 3D-*XY* critical fluctuation $\left(\sim n_s^{z/(d-2+z)},\ d = 3, z = 0.53 \text{ (fitted)}\right)$ and 3D-BEC $\left(\sim n_s^{2/3}\right)$ are also used to fit points ($x = 6.52$ and 6.92). It is interesting that T_c for optimally doped $YBa_2Cu_3O_{6.92}$ and $Ba(Co_{0.074}Fe_{0.926})_2As_2$ (■) almost fall on a (Uemura) line. The penetration depth anisotropy in $YBa_2Cu_3O_{6+x}$ (●) is surprisingly weakly dependent on superfluid density.

than in $YBa_2Cu_3O_{6.52}$ where $\lambda_c/\lambda_{ab} \sim 45.0$ [185]. This drop in dimensionality could also play a role in the reduction of T_c going from Ortho-I to Ortho-II since BEC T_c is suppressed in a more 2D superconductor (cf. section 2.4). The in-plane anisotropy in magnetic penetration depth may be influenced by several factors such as lattice anisotropy - which may cause static charge stripes [190]. From in-plane resistivity anisotropy measurements [191], these spin stripes are claimed to be intrinsically conducting and transport is easier along the direction of the stripes. It has been argued that CuO_2 planes, not the CuO chains, are responsible [45] for these stripe states. Although CuO chains can contribute superfluid carriers, for $T < 80$ K, carriers in the chains are thought to be localized [166] and do not contribute to the electrical transport properties for this temperature range. However, CuO chains may exert a potential on the planes - thereby indirectly influencing the effective mass tensor and electrical transport as well as the anisotropy in the magnetic penetration depth. The measured anisotropies $\left(\lambda_a/\lambda_b\right)$ in $YBa_2Cu_3O_{6.998}$ (every CuO chain is full) and $YBa_2Cu_3O_{6.52}$ (every second CuO chain is full) are very similar; however, $YBa_2Cu_3O_{6.92}$ (not fully ordered chains) yields a very different anisotropy. This suggests chain ordering may be important in determining in-plane anisotropy. Measurements of anisotropies for a number of dopings will be required to elucidate the anisotropy's dependence on chain or-

dering and superfluid density.

4.4 Discussion on ``Deadlayer"

As mentioned in earlier sections, a superconductor below H_{c1} expels any external magnetic field and the internal decays exponentially inside the sample close to the surface, according to the London equations. However, very close to surface, there is apparently a distance over which magnetic field essentially remains constant - suggesting an effective dead layer. One possible explanation is surface roughness: small perturbations from a perfect flat geometry. Recently the problem has been studied theoretically using a combination of analytic and numerical methods [1]. Without loss in generality, the rough surface was modeled as one which varies harmonically in space:

$$z = \epsilon \cos(\omega_x x)\cos(\omega_y y). \tag{4.14}$$

Lindstrom *et al.* [1] has found via linear analysis, that average magnetic field $|\boldsymbol{B}|_{\text{avg}}$ does indeed differ from the London solution by as much as 1 %. These simulations (figure 4.33) suggest that for surfaces with roughness amplitudes (ϵ) in the ballpark of $\lambda/10$ whose spatial frequencies aren't too high, the dead layer is no bigger than $\lambda/20$. This is consistent with observation. However, one difference between theory and experiment is that the gradient in the average field in the direction normal to the surface is always finite in theory whereas a simple deadlayer model used in this thesis assumes $\mathrm{d}|\boldsymbol{B}/\mathrm{d}z|$ is zero inside the deadlayer.

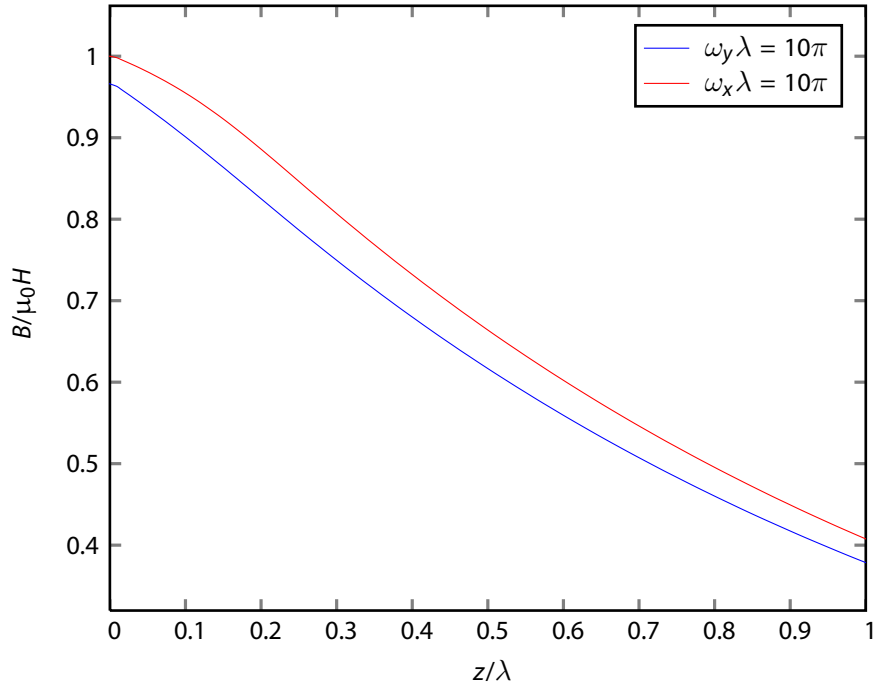

Figure 4.33 : Simulated external field [1] for the depth range 0 nm to 10λ. Only the region of 0-λ is shown. The blue and red curves are for sinusoidal variation in surface height along *y* and *x* axis, respectively, while the external field is along *x*-direction. The fits to simulations suggest an average ~ 5 % longer λ.

Another possibility is that magnetic flux can penetrate near the surface in the form of vortices which is favored if there is suppression of the order parameter near twin or grain boundaries [192, 193]. Surface roughness will also tend to favor vortex penetration due to demagnetization effects associated with a rough surface. For example it has been proposed that surface roughness is the source of vortex nucleation at fields $H \leq H_{c1}$ [194]. Surface vortices have been observed in YBCO in fields as minute as 4 G applied parallel to a – b plane [195]. Thus it seems possible that the higher magnetic fields required for low energy μSR will favor vortex penetration near the vacuum-surface boundary. Such vortex penetration and surface roughness would also contribute to the additional line broadening we observe in the Meissner state. Field inhomogeneities may result from local variations of the supercurrent close to surface due to surface roughness, twin boundaries and grain boundaries [196]. Further experiments on atomically flat surfaces may help elucidate the origin of the reduction of screening supercurrents near the surface.

CHAPTER 5 CONCLUSIONS AND OUTLOOK

In this thesis, the most direct measurements of the magnetic penetration depth in the $\lambda_{a/b}$ and its anisotropyies $\left(\equiv \lambda_a/\lambda_b\right)$ have been made for three different oxygen (x = 6.52, 6.92 and 6.998) contents of $YBa_2Cu_3O_{6+x}$ as well as in $Ba(Co_{0.074}Fe_{0.926})_2As_2$. A novel method, using low energy muons, was used to measure the field profile directly in the Meissner state. Using the London model and simulated stopping profiles in the Meissner state, one is able to extract a precise measurement of the magnetic penetration depth as a function of observable parameters such doping, magnetic field, and temperature. The measured penetration depths depend only slightly on the details of the model used. For example, the uncertainty in the manner, by which the phase is treated, is included as a systematic error in the final results. The field profiles are obtained directly by measuring the muon frequency spectrum - which contains most of the relevant information about muons' local magnetic environment, as a function of the implantation energy. All measurements in the superconducting state were carried out under **zero-field-cooled** conditions in order to avoid flux trapping in the sample. This is the first direct observation of exponentially decaying field profiles in high quality crystals of an exotic superconductor $YBa_2Cu_3O_{6+x}$ and $Ba(Co_{0.074}Fe_{0.926})_2As_2$. The measured values of λ are somewhat different from previous works using bulk methods. The fitted λ is independent of magnetic field at sufficiently low magnetic fields, as one expects from a simple London model ignoring any non linear effects. However, care must be taken to ensure that the field is low enough to avoid vortex penetration. Surprisingly, the field below which the fitted λ is independent of field, is substantially below H_{c1}, which is not fully understood at present.

Small deviations, from the London model, are observed, below the surface of the crystals, which indicate that there is a suppression of the supercurrent density close to the surface, on the scale of d around 10 nm to 20 nm. Also there is a substantial broadening of the field distribution beyond what one would expect from the range straggling and Cu nuclear dipole moments. The mosaic geometry has virtually no affect on this broadening which indicates that muons experience broadened field distribution in each crystal. It seems likely that surface roughness and/or demagnetization affects at the edges of each crystal are at least partially responsible for the deviations from the London model. A suppression of the supercurrent density was also reported in a previous low energy μSR study of the field profile in a thin film of $YBa_2Cu_3O_{6.92}$ and attributed to surface roughness. Also, this is confirmed by recent theoretical studies on the affect of surface roughness. Measurements on atomically flat cleaved surfaces may be needed to resolve the true origin of d and deviations from the London model we report.

Our most important result is that the measured $\lambda_{a/b}(0\,\mathrm{K})$ values do not follow the widely reported Uemura relation $\left(T_c \propto \lambda_{ab}^{-2}\right)$. Interestingly Bose-Einstein condensation in 3D and

3D-*XY* critical fluctuation also predict a sub-linear relationship of T_c on λ_{ab}^{-2}. It is also important to note that YBCO becomes more two dimensional at lower doping. This could partially be responsible for the reduction in T_c at low doping. For example, in a 2D system, the critical temperature $T_c = 0$, so that there cannot be any superconductivity in such a system at any finite temperature.

One of the interesting aspects of the T_c-vs - $\left(\lambda_{ab}^{-2}\right)$ is that optimally doped cuprate and Co-doped pnictide almost falls on a straight line going through the origin to optimally doped YBCO. Thus while the variation of T_c versus doping in YBCO does not follow the Uemura relation, we do confirm that the T_c at optimal doping does seem to follow this relation when comparing different families. Clearly many more measurements are needed in a variety of supercondcutors to see how valid this empirical relationship really is.

We also report the a – b anisotropy in the penetration depth for all three oxygen concentrations of $YBa_2Cu_3O_{6+x}$. The a–b anisotropy, being the ratio of λ (between the a and b directions), is determined with more accuracy than the penetration depths themselves. There is a rather weak dependence of λ_a/λ_b on oxygen concentration - which is surprising considering the significant changes in the oxygen chains between Ortho-I and Ortho-II.

A low temperature linear dependence of $\lambda_{a/b}^{-2}$ has also been observed in all the oxygen dopings in $YBa_2Cu_3O_{6+x}$, which is an important signature for a d-wave superconducting gap function. The temperature dependence of the London penetration depth $\lambda_{a/b}$ can be fit to a semi-classical model of a cylindrical Fermi surface in YBCO. The T-dependence is consistent with μW measurements. Our measurements of $\lambda(0)$ are much more accurate and are needed to convert $\Delta\lambda(T)$ (from μW measurements) into the T-dependence of the superfluid density. The fitted superconducting gaps $\Delta_{a/b}(0\,\mathrm{K})$ are consistent with a $d_{x^2-y^2}$-type order in YBCO. Gap anisotropy in YBCO is close to 1, suggesting that effective mass tensors in two directions are independent of temperature. A two-gap s-wave model and a weak power law model describe the temperature dependence of the superfluid density equally well in $Ba(Co_{0.074}Fe_{0.926})_2As_2$.

Perhaps most importantly, it is shown that low energy μSR can be used to probe the near surface region of small single crystals which are much smaller than the beam diameter.

Future Work: It should be possible to test the origins suppressed superconductivity near the surface, by depositing thin metallic layers on top of the crystals. By controlling the thickness of the metallic layer, it should be possible to implant muons close to the surface of a superconductor using a muon energy around 2 keV. Basically the overlayer would act as a degrader. Very low energy muons will stop close to the interface between the superconductor and normal metal interface. In this way, it may be possible to probe the magnetic field much close to the surface of the superconductor than is currently possible. In this way, it may be possible to discern between demagnetization effects and a true dead layer from surface roughness.

We note that, these experiments require a considerable amount of beamtime since the amplitude of the signal is reduced compared to studies on large samples. One way to increase our

signal to noise ratio would be to make the sample plate just big enough to hold the sample. This would get rid of the non precessing background signal coming from muons landing on the nickel sample plate. Also, current positron counters may be replaced by incorporating position sensitive detectors to ensure the positron is coming from the sample and not elsewhere. Despite these limitations, the technique has proven to work extremely well. It has provided the most accurate measurements of the London penetration depth so far. We expect this method will have a significant impact on the field of exotic superconductivity.

BIBLIOGRAPHY

[1] Lindstrom, M. Asymptotic and numerical modeling of magnetic field profiles in superconductors with rough boundaries and multi-component gas transport in PEM fuel cells. University Of British Columbia (2010). ◇ Cited on pages viii, 54 & 75.

[2] Onnes, H. K. Commun. Phys. Lab. Univ. Leiden, **120b,122b,124c** (1911). ◇ Cited on page 1.

[3] Onnes, H. K. The resistance of pure mercury at helium temperatures. Comm. Leiden., **120 b** (1911). ◇ Cited on page 1.

[4] Meissner, W. and Oschenfel, R. Naturwiss., **21** (1933). ◇ Cited on page 1.

[5] London, F. and London, H. Proc. R. Soc. London, **A149** (1935). ◇ Cited on page 1.

[6] Ginzburg, V. L. and Landau, L. D. On the Theory of superconductivity. Zh. Eksp. Teor. Fiz., **20**, 1064--1082 (1950). ◇ Cited on page 1.

[7] Bardeen, J., Cooper, L. N., and Schrieffer, J. R. Theory of Superconductivity. Phys. Rev., **108**, 1175--1204 (1957). ◇ Cited on page 1.

[8] Bardeen, J., Cooper, L. N., and Schrieffer, J. R. Microscopic Theory of Superconductivity. Phys. Rev., **106**, 162--164 (1957). ◇ Cited on page 1.

[9] McMillan, W. L. Transition temperature of strong-coupled superconductors. Phys. Rev., **167**, 331--344 (1968). ◇ Cited on page 2.

[10] Cooper, L. N. Bound Electron Pairs in a Degenerate Fermi Gas. Phys. Rev., **104**, 1189--1190 (1956). ◇ Cited on pages 2 & 15.

[11] Bednorz, J. G. and Müller, K. A. Possible high T_c superconductivity in the Ba-La-Cu-O system. Zeitschrift für Physik B Condensed Matter, **64**, 189--193 (1986). ◇ Cited on page 2.

[12] Wu, M. K., Ashburn, J. R., Torng, C. J., Hor, P. H., Meng, R. L., Gao, L., Huang, Z. J., Wang, Y. Q., and Chu, C. W. Superconductivity at 93 K in a new mixed-phase Y-Ba-Cu-O compound system at ambient pressure. Phys. Rev. Lett., **58**, 908--910 (1987). ◇ Cited on page 2.

[13] Elert, G. (2002), Highest critical temperature superconductor. [Online; accessed 5-February-2012]. ◇ Cited on page 3.

[14] Blatter, G., Feigel'man, M. V., Geshkenbein, V. B., Larkin, A. I., and Vinokur, V. M. Vortices in high-temperature superconductors. Rev. Mod. Phys., **66**, 1125--1388 (1994). ◇ Cited on page 4.

[15] Sachdev, S. and Zhang, S.-C. Tuning Order in Cuprate Superconductors. Science, **295**, 452--454 (2002). ◇ Cited on page 5.

[16] Hill, R. W., Proust, C., Taillefer, L., Fournier, P., and Greene, R. L. Breakdown of Fermi-liquid theory in a copper-oxide superconductor. Nature, **414**, 711--715 (2001). ◇ Cited on page 6.

[17] Capponi, J. J., Chaillout, C., Hewat, A. W., Lejay, P., Marezio, M., Nguyen, N., Raveau, B., Soubeyroux, J. L., Tholence, J. L., and Tournier, R. Structure of the 100 K Superconductor $YBa_2Cu_3O_7$ between (5 - 300) K by Neutron Powder Diffraction. EPL (Europhysics Letters), **3**, 1301 (1987). ◇ Cited on page 7.

[18] Momma, K. and Izumi, F. *VESTA*: a three-dimensional visualization system for electronic and structural analysis. Journal of Applied Crystallography, **41**, 653--658 (2008). ◇ Cited on page 7.

[19] Keren, A., Le, L. P., Luke, G. M., Sternlieb, B. J., Wu, W. D., Uemura, Y. J., Tajima, S., and Uchida, S. Muon-spin-rotation measurements in infinite-layer and infinite-chain cuprate antiferromagnets: $Ca_{0.86}Sr_{0.14}CuO_2$ and Sr_2CuO_3. Phys. Rev. B, **48**, 12926--12935 (1993). ◇ Cited on pages 6 & 13.

[20] Tallon, J. L., Bernhard, C., Shaked, H., Hitterman, R. L., and Jorgensen, J. D. Generic superconducting phase behavior in high-T_c cuprates: T_c variation with hole concentration in $YBa_2Cu_3O_{7-\delta}$. Phys. Rev. B, **51**, 12911--12914 (1995). ◇ Cited on page 6.

[21] Bishop, A., et al. Real and marginal isotope effects in cuprate superconductors. Journal of Superconductivity and Novel Magnetism, **20**, 393--396 (2007), 10.1007/s10948-007-0235-6. ◇ Cited on page 7.

[22] Lanzara, A., et al. Evidence for ubiquitous strong electron-phonon coupling in high-temperature superconductors. Nature, **412**, 510--514 (2001). ◇ Cited on page 7.

[23] Devereaux, T. P., Cuk, T., Shen, Z.-X., and Nagaosa, N. Anisotropic electron-phonon interaction in the cuprates. Phys. Rev. Lett., **93**, 117004 (2004). ◇ Cited on page 7.

[24] Bohnen, K.-P., Heid, R., and Krauss, M. Phonon dispersion and electron-phonon interaction for $YBa_2Cu_3O_7$ from first-principles calculations. EPL (Europhysics Letters), **64**, 104 (2003). ◇ Cited on page 7.

[25] Falter, C. and Hoffmann, G. A. Nonlocal electron-phonon coupling of ionic charge-fluctuation type and phonon anomalies in high-temperature superconductors. Phys. Rev. B, **64**, 054516 (2001). ◇ Cited on page 7.

[26] Chung, J.-H., et al. In-plane anisotropy and temperature dependence of oxygen phonon modes in $YBa_2Cu_3O_{6.95}$. Phys. Rev. B, **67**, 014517 (2003). ◇ Cited on page 7.

[27] Reznik, D., Pintschovius, L., Ito, M., Iikubo, S., Sato, M., Goka, H., Fujita, M., Yamada, K., Gu, G. D., and Tranquada, J. M. Electron-phonon coupling reflecting dynamic charge inhomogeneity in copper oxide superconductors. Nature, **440**, 1170--1173 (2006). ◇ Cited on page 7.

[28] Giustino, F., Cohen, M. L., and Louie, S. G. Small phonon contribution to the photoemission kink in the copper oxide superconductors. Nature, **452**, 975--978 (2008). ◇ Cited on page 7.

[29] Anderson, P. W. The Resonating Valence Bond State in La_2CuO_4 and Superconductivity. Science, **235**, 1196--1198 (1987). ◇ Cited on page 7.

[30] Anderson, P. W. Resonating valence bonds: A new kind of insulator? Materials Research Bulletin, **8**, 153 -- 160 (1973). ◇ Cited on page 7.

[31] Anderson, P. W., Lee, P. A., Randeria, M., Rice, T. M., Trivedi, N., and Zhang, F. C. The physics behind high-temperature superconducting cuprates: the `plain vanilla' version of RVB. Journal of Physics: Condensed Matter, **16**, R755 (2004). ◇ Cited on page 7.

[32] Baskaran, G., Zou, Z., and Anderson, P. W. The resonating valence bond state and high-T_c superconductivity -- A mean field theory. Solid State Communications, **63**, 973 -- 976 (1987). ◇ Cited on page 7.

[33] Vaknin, D., Sinha, S. K., Moncton, D. E., Johnston, D. C., Newsam, J. M., Safinya, C. R., and King, H. E. Antiferromagnetism in La_2CuO_{4-y}. Phys. Rev. Lett., **58**, 2802--2805 (1987). ◇ Cited on page 8.

[34] Tranquada, J. M., et al. Neutron-Diffraction Determination of Antiferromagnetic Structure of Cu Ions in $YBa_2Cu_3O_{6+x}$ with $x = 0.0$ and 0.15. Phys. Rev. Lett., **60**, 156--159 (1988). ◇ Cited on page 8.

[35] Moudden, A. H., Shirane, G., Tranquada, J. M., Birgeneau, R. J., Endoh, Y., Yamada, K., Hidaka, Y., and Murakami, T. Antiferromagnetic ordering of Cu ions in $NdBa_2Cu_3O_{6.1}$. Phys. Rev. B, **38**, 8720--8723 (1988). ◇ Cited on pages 8 & 13.

[36] Shirane, G., Endoh, Y., Birgeneau, R. J., Kastner, M. A., Hidaka, Y., Oda, M., Suzuki, M., and Murakami, T. Two-dimensional antiferromagnetic quantum spin-fluid state in La_2CuO_4. Phys. Rev. Lett., **59**, 1613--1616 (1987). ◇ Cited on pages 8 & 13.

[37] Endoh, Y., et al. Static and dynamic spin correlations in pure and doped La_2CuO_4. Phys. Rev. B, **37**, 7443--7453 (1988). ◇ Cited on page 8.

[38] Niedermayer, C., Bernhard, C., Blasius, T., Golnik, A., Moodenbaugh, A., and Budnick, J. I. Common Phase Diagram for Antiferromagnetism in $La_{2-x}Sr_xCuO_4$ and $Y_{1-x}Ca_xBa_2Cu_3O_6$ as Seen by Muon Spin Rotation. Phys. Rev. Lett., **80**, 3843--3846 (1998). ◇ Cited on page 8.

[39] Hussey, N. E. Low-energy quasiparticles in high-T_c cuprates. Advances in Physics, **51**, 1685--1771 (2002). ◇ Cited on page 8.

[40] Hussey, N. E., Abdel-Jawad, M., Carrington, A., Mackenzie, A. P., and Balicas, L. A coherent three-dimensional Fermi surface in a high-transition-temperature superconductor. Nature, **425**, 814--817 (2003). ◇ Cited on page 8.

[41] Yamaji, K. On the Angle Dependence of the Magnetoresistance in Quasi-Two-Dimensional Organic Superconductors. Journal of the Physical Society of Japan, **58**, 1520--1523 (1989). ◇ Cited on page 8.

[42] Audouard, A., Jaudet, C., Vignolles, D., Liang, R., Bonn, D. A., Hardy, W. N., Taillefer, L., and Proust, C. Multiple Quantum Oscillations in the de Haas-van Alphen Spectra of the Underdoped High-Temperature Superconductor $YBa_2Cu_3\mathbf{O}_{6.5}$. Phys. Rev. Lett., **103**, 157003 (2009). ◇ Cited on page 9.

[43] Tanaka, K., et al. Distinct Fermi-Momentum-Dependent Energy Gaps in Deeply Underdoped Bi2212. Science, **314**, 1910--1913 (2006). ◇ Cited on page 9.

[44] Ding, H., Yokoya, T., Campuzano, J. C., Takahashi, T., Randeria, M., Norman, M. R., Mochiku, T., Kadowaki, K., and Giapintzakis, J. Spectroscopic evidence for a pseudogap in the normal state of underdoped high-T_c superconductors. Nature, **382**, 51--54 (1996). ◇ Cited on page 9.

[45] Daou, R., et al. Broken rotational symmetry in the pseudogap phase of a high-T_c superconductor. Nature, **463**, 519--522 (2010). ◇ Cited on pages 9 & 74.

[46] Timusk, T. and Statt, B. The pseudogap in high-temperature superconductors: an experimental survey. Reports on Progress in Physics, **62**, 61 (1999). ◇ Cited on page 9.

[47] Loeser, A. G., Shen, Z.-X., Dessau, D. S., Marshall, D. S., Park, C. H., Fournier, P., and Kapitulnik, A. Excitation Gap in the Normal State of Underdoped $Bi_2Sr_2CaCu_2O_{8+\delta}$. Science, **273**, 325--329 (1996). ◇ Cited on page 9.

[48] Laughlin, R. B. PERSPECTIVES A critique of two metals. Advances in Physics, **47**, 943 -- 958 (1998). ◇ Cited on page 9.

[49] Sachdev, S. Quantum Criticality: Competing Ground States in Low Dimensions. Science, **288**, 475--480 (2000). ◇ Cited on page 9.

[50] Tallon, J. and Loram, J. The doping dependence of T^* - what is the real high-T_c phase diagram? PHYSICA C, **349**, 53--68 (2001). ◇ Cited on page 9.

[51] Li, Y., Baledent, V., Barisic, N., Cho, Y., Fauque, B., Sidis, Y., Yu, G., Zhao, X., Bourges, P., and Greven, M. Unusual magnetic order in the pseudogap region of the superconductor $HgBa_2CuO_{4+\delta}$. Nature, **455**, 372--375 (2008). ◇ Cited on page 9.

[52] Varma, C. M. Non-Fermi-liquid states and pairing instability of a general model of copper oxide metals . Phys. Rev. B, **55**, 14554--14580 (1997). ◇ Cited on page 9.

[53] Varma, C. M. Pseudogap Phase and the Quantum-Critical Point in Copper-Oxide Metals. Phys. Rev. Lett., **83**, 3538--3541 (1999). ◇ Cited on page 9.

[54] Gurvitch, M. and Fiory, A. T. Resistivity of $La_{1.825}Sr_{0.175}CuO_4$ and $YBa_2Cu_3O_7$ to 1100 K: Absence of saturation and its implications. Phys. Rev. Lett., **59**, 1337--1340 (1987). ◇ Cited on page 9.

[55] Thomas, G. A., Orenstein, J., Rapkine, D. H., Capizzi, M., Millis, A. J., Bhatt, R. N., Schneemeyer, L. F., and Waszczak, J. V. $Ba_2YCu_3O_{7-\delta}$: Electrodynamics of Crystals with High Reflectivity. Phys. Rev. Lett., **61**, 1313--1316 (1988). ◇ Cited on page 9.

[56] Gurvitch, M., Valles, J. M., Cucolo, A. M., Dynes, R. C., Garno, J. P., Schneemeyer, L. F., and Waszczak, J. V. Reproducible tunneling data on chemically etched single crystals of $YBa_2Cu_3O_7$. Phys. Rev. Lett., **63**, 1008--1011 (1989). ◇ Cited on page 9.

[57] Anderson, P. W. The `strange metal' is a projected Fermi liquid with edge singularities. Nat Phys, **2**, 626--630 (2006). ◇ Cited on page 9.

[58] Varma, C. M., Littlewood, P. B., Schmitt-Rink, S., Abrahams, E., and Ruckenstein, A. E. Phenomenology of the normal state of Cu-O high-temperature superconductors. Phys. Rev. Lett., **63**, 1996--1999 (1989). ◇ Cited on page 9.

[59] Gough, C. E., Colclough, M. S., Forgan, E. M., Jordan, R. G., Keene, M., Muirhead, C. M., Rae, A. I. M., Thomas, N., Abell, J. S., and Sutton, S. Flux quantization in a high-T_c superconductor. Nature, **326**, 855--855 (1987). ◇ Cited on page 9.

[60] Tsuei, C. C., Kirtley, J. R., Chi, C. C., Yu-Jahnes, L. S., Gupta, A., Shaw, T., Sun, J. Z., and Ketchen, M. B. Pairing Symmetry and Flux Quantization in a Tricrystal Superconducting Ring of $YBa_2Cu_3O_{7-\delta}$. Phys. Rev. Lett., **73**, 593--596 (1994). ◇ Cited on page 9.

[61] Gammel, P. L., Bishop, D. J., Dolan, G. J., Kwo, J. R., Murray, C. A., Schneemeyer, L. F., and Waszczak, J. V. Observation of Hexagonally Correlated Flux Quanta In $YBa_2Cu_3O_7$. Phys. Rev. Lett., **59**, 2592--2595 (1987). ◇ Cited on page 9.

[62] Ren, Z. A., Yang, J., Lu, W., Yi, W., Che, G. C., Dong, X. L., Sun, L. L., and Zhao, Z. X. Superconductivity at 52 K in iron based F doped layered quaternary compound $Pr[O_{1-x}F_x]FeAs$. Materials Research Innovations, **12**, 105--106 (2008). ◇ Cited on page 10.

[63] Chen, G. F., Li, Z., Wu, D., Li, G., Hu, W. Z., Dong, J., Zheng, P., Luo, J. L., and Wang, N. L. Superconductivity at 41 K and Its Competition with Spin-Density-Wave Instability in Layered $CeO_{1-x}F_xFeAs$. Phys. Rev. Lett., **100**, 247002 (2008). ◇ Cited on page 10.

[64] Chen, X. H., Wu, T., Wu, G., Liu, R. H., Chen, H., and Fang, D. F. Superconductivity at 43 K in $SmFeAsO_{1-x}F_x$. Nature, **453**, 761--762 (2008). ◇ Cited on page 10.

[65] Kamihara, Y., Watanabe, T., Hirano, M., and Hosono, H. Iron-Based Layered Superconductor $La[O_{1-x}F_x]FeAs$ (x = 0.05-0.12) with T_c = 26 K. Journal of the American Chemical Society, **130**, 3296--3297 (2008). ◇ Cited on pages 10 & 11.

[66] Kreyssig, A., et al. Pressure-induced volume-collapsed tetragonal phase of $CaFe_2As_2$ as seen via neutron scattering. Phys. Rev. B, **78**, 184517 (2008). ◇ Cited on page 10.

[67] Sefat, A. S., Jin, R., McGuire, M. A., Sales, B. C., Singh, D. J., and Mandrus, D. Superconductivity at 22 K in Co-Doped $BaFe_2As_2$ Crystals. Phys. Rev. Lett., **101**, 117004 (2008). ◇ Cited on page 10.

[68] Canfield, P. C. and Fisk, Z. Growth of single crystals from metallic fluxes. Philosophical Magazine Part B, **65**, 1117--1123 (1992). ◇ Cited on page 10.

[69] Huang, Q., Qiu, Y., Bao, W., Green, M. A., Lynn, J. W., Gasparovic, Y. C., Wu, T., Wu, G., and Chen, X. H. Neutron-Diffraction Measurements of Magnetic Order and a Structural Transition in the Parent $BaFe_2As_2$ Compound of FeAs-Based High-Temperature Superconductors. Phys. Rev. Lett., **101**, 257003 (2008). ◇ Cited on pages 10 & 11.

[70] de la Cruz, C., et al. Magnetic order close to superconductivity in the iron-based layered $LaO_{1-x}F_xFeAs$ systems. Nature, **453**, 899--902 (2008). ◇ Cited on pages 10 & 11.

[71] Rotter, M., Tegel, M., and Johrendt, D. Superconductivity at 38 K in the Iron Arsenide $(Ba_{1-x}K_x)Fe_2As_2$. Phys. Rev. Lett., **101**, 107006 (2008). ◇ Cited on page 11.

[72] Klauss, H.-H., et al. Commensurate Spin Density Wave in LaFeAsO: A Local Probe Study. Phys. Rev. Lett., **101**, 077005 (2008). ◇ Cited on page 11.

[73] Krellner, C., Caroca-Canales, N., Jesche, A., Rosner, H., Ormeci, A., and Geibel, C. Magnetic and structural transitions in layered iron arsenide systems: AFe$_2$As$_2$ versus RFeAsO. Phys. Rev. B, **78**, 100504 (2008). ◇ Cited on page 11.

[74] Jesche, A., et al. Strong coupling between magnetic and structural order parameters in $SrFe_2As_2$. Phys. Rev. B, **78**, 180504 (2008). ◇ Cited on page 11.

[75] Goldman, A. I., Argyriou, D. N., Ouladdiaf, B., Chatterji, T., Kreyssig, A., Nandi, S., Ni, N., Bud'ko, S. L., Canfield, P. C., and McQueeney, R. J. Lattice and magnetic instabilities in $CaFe_2As_2$: A single-crystal neutron diffraction study. Phys. Rev. B, **78**, 100506 (2008). ◇ Cited on page 11.

[76] Gen-Fu, C., Zheng, L., Gang, L., Wan-Zheng, H., Jing, D., Jun, Z., Xiao-Dong, Z., Ping, Z., Nan-Lin, W., and Jian-Lin, L. Superconductivity in Hole-Doped $(Sr_{1-x}K_x)Fe_2As_2$. Chinese Physics Letters, **25**, 3403 (2008). ◇ Cited on page 11.

[77] Sasmal, K., Lv, B., Lorenz, B., Guloy, A. M., Chen, F., Xue, Y.-Y., and Chu, C.-W. Superconducting Fe-Based Compounds $(A_{1-x}Sr_x)Fe_2As_2$ with A = K and Cs with Transition Temperatures up to 37 K. Phys. Rev. Lett., **101**, 107007 (2008). ◇ Cited on page 11.

[78] Ren, Z.-A., et al. Superconductivity and phase diagram in iron-based arsenic-oxides $ReFeAsO_{1-\delta}$ (Re = rare-earth metal) without fluorine doping. EPL (Europhysics Letters), **83**, 17002 (2008). ◇ Cited on page 11.

[79] Kito, H., Eisaki, H., and Iyo, A. Superconductivity at 54 K in F-Free $NdFeAsO_{1-y}$. Journal of the Physical Society of Japan, **77**, 063707 (2008). ◇ Cited on page 11.

[80] Johnston, D. C. (2010), The Puzzle of High Temperature Superconductivity in Layered Iron Pnictides and Chalcogenides. ◇ Cited on page 11.

[81] Tranquada, J. M. Modulated superfluid density in an iron-pnictide superconductor. Physics, **3**, 41 (2010). ◇ Cited on page 11.

[82] Nandi, S., et al. Anomalous Suppression of the Orthorhombic Lattice Distortion in Superconducting $Ba(Fe_{1-x}Co_x)_2As_2$ Single Crystals. Phys. Rev. Lett., **104**, 057006 (2010). ◇ Cited on page 11.

[83] Dong, J., et al. Competing orders and spin-density-wave instability in La(O_{1-x} F_x)FeAs. EPL (Europhysics Letters), **83**, 27006 (2008). ◇ Cited on page 11.

[84] Boeri, L., Dolgov, O. V., and Golubov, A. A. Is $LaFeAsO_{1-x}F_x$ an Electron-Phonon Superconductor? Phys. Rev. Lett., **101**, 026403 (2008). ◇ Cited on page 12.

[85] Mazin, I. and Schmalian, J. Pairing symmetry and pairing state in ferropnictides: Theoretical overview. Physica C: Superconductivity, **469**, 614 -- 627 (2009). ◇ Cited on pages 12 & 21.

[86] D.J. and Singh Electronic structure of Fe-based superconductors. Physica C: Superconductivity, **469**, 418--424 (2009). ◇ Cited on page 12.

[87] Yildirim, T. Origin of the 150-K Anomaly in LaFeAsO: Competing Antiferromagnetic Interactions, Frustration, and a Structural Phase Transition. Phys. Rev. Lett., **101**, 057010 (2008). ◇ Cited on page 12.

[88] Dai, J., Si, Q., Zhu, J.-X., and Abrahams, E. Iron pnictides as a new setting for quantum criticality. Proceedings of the National Academy of Sciences, **106**, 4118--4121 (2009). ◇ Cited on page 12.

[89] Sefat, A. S., Singh, D. J., Jin, R., McGuire, M. A., Sales, B. C., and Mandrus, D. Renormalized behavior and proximity of $BaCo_2As_2$ to a magnetic quantum critical point. Phys. Rev. B, **79**, 024512 (2009). ◇ Cited on page 12.

[90] Liu, R. H., et al. Anomalous Transport Properties and Phase Diagram of the FeAs-Based $SmFeAsO_{1-x}F_x$ Superconductors. Phys. Rev. Lett., **101**, 087001 (2008). ◇ Cited on page 12.

[91] Luetkens, H., et al. The electronic phase diagram of the $LaO_{1-x}F_xFeAs$ superconductor. Nat Mater, **8**, 305--309 (2009). ◇ Cited on page 12.

[92] Grafe, H.-J., et al. ^{75}As NMR Studies of Superconducting $LaFeAsO_{0.9}F_{0.1}$. Phys. Rev. Lett., **101**, 047003 (2008). ◇ Cited on page 12.

[93] Matano, K., Ren, Z. A., Dong, X. L., Sun, L. L., Zhao, Z. X., and qing Zheng, G. Spin-singlet superconductivity with multiple gaps in $PrFeAsO_{0.89}F_{0.11}$. EPL (Europhysics Letters), **83**, 57001 (2008). ◇ Cited on page 12.

[94] Ning, F., Ahilan, K., Imai, T., Sefat, A. S., Jin, R., McGuire, M. A., Sales, B. C., and Mandrus, D. ^{59}Co and ^{75}As NMR Investigation of Electron-Doped High T_c Superconductor $BaFe_{1.8}Co_{0.2}As_2$ (T_c = 22 K). Journal of the Physical Society of Japan, **77**, 103705 (2008). ◇ Cited on page 12.

[95] Uemura, Y. J., et al. Magnetic-field penetration depth in K_3C_{60} measured by muon spin relaxation. Nature, **352**, 605--607 (1991). ◇ Cited on page 12.

[96] Hardy, W. N., Bonn, D. A., Morgan, D. C., Liang, R., and Zhang, K. Precision measurements of the temperature dependence of λ in $YBa_2Cu_3O_{6.95}$: Strong evidence for nodes in the gap function. Phys. Rev. Lett., **70**, 3999--4002 (1993). ◇ Cited on pages 12, 13 & 14.

[97] Sonier, J. E., et al. New muon-spin-rotation measurement of the temperature dependence of the magnetic penetration depth in $YBa_2Cu_3O_{6.95}$. Phys. Rev. Lett., **72**, 744--747 (1994). ◇ Cited on page 12.

[98] Uemura, Y. J., et al. Universal Correlations between T_c and $\frac{n_s}{m^*}$ (Carrier Density over Effective Mass) in High-T_c Cuprate Superconductors. Phys. Rev. Lett., **62**, 2317--2320 (1989). ◇ Cited on page 12.

[99] Uemura, Y. J., et al. Basic similarities among cuprate, bismuthate, organic, Chevrel-phase, and heavy-fermion superconductors shown by penetration-depth measurements. Phys. Rev. Lett., **66**, 2665--2668 (1991). ◇ Cited on page 12.

[100] Drew, A. J., et al. Coexistence of Magnetic Fluctuations and Superconductivity in the Pnictide High Temperature Superconductor $SmFeAsO_{1-x}F_x$ Measured by Muon Spin Rotation. Physical Review Letters, **101**, 097010 (2008). ◇ Cited on page 12.

[101] Franz, M. and Iyengar, A. P. Superfluid Density of Strongly Underdoped Cuprate Superconductors from a Four-Dimensional *XY* Model. Phys. Rev. Lett., **96**, 047007 (2006). ◇ Cited on page 12.

[102] Iulian Hetel, M. R., Thomas R. Lemberger Quantum critical behaviour in the superfluid density of strongly underdoped ultrathin copper oxide films. Nature Physics, **3** (2007). ◇ Cited on page 13.

[103] Schrieffer, J. R., Wen, X.-G., and Zhang, S.-C. Spin-bag mechanism of high-temperature superconductivity. Phys. Rev. Lett., **60**, 944--947 (1988). ◇ Cited on page 13.

[104] Basov, D. N. and Timusk, T. Electrodynamics of high- T_c superconductors. Rev. Mod. Phys., **77**, 721--779 (2005). ◇ Cited on page 13.

[105] Grabowski, S., Schmalian, J., and Bennemann, K. H. Electronic theory for bilayer-effects in high-t_c superconductors. Physica C: Superconductivity, **282-287**, 1681 -- 1682 (1997). ◇ Cited on page 13.

[106] Atkinson, W. A. and Sonier, J. E. Role of CuO chains in vortex core structure in $YBa_2Cu_3O_{7-\delta}$. Phys. Rev. B, **77**, 024514 (2008). ◇ Cited on page 13.

[107] Morr, D. K. and Balatsky, A. V. Proximity Effects and Quantum Dissipation in the Chains of $YBa_2Cu_3O_{6+x}$. Phys. Rev. Lett., **87**, 247002 (2001). ◇ Cited on page 13.

[108] Nunner, T. S. and Hirschfeld, P. J. Microwave conductivity of d-wave superconductors with extended impurities. Phys. Rev. B, **72**, 014514 (2005). ◇ Cited on page 13.

[109] Friedmann, T. A., Rabin, M. W., Giapintzakis, J., Rice, J. P., and Ginsberg, D. M. Direct measurement of the anisotropy of the resistivity in the a-b plane of twin-free, single-crystal, superconducting $YBa_2Cu_3O_{7-\delta}$. Phys. Rev. B, **42**, 6217--6221 (1990). ◇ Cited on page 13.

[110] Gagnon, R., Lupien, C., and Taillefer, L. T^2 dependence of the resistivity in the Cu-O chains of $YBa_2Cu_3O_{6.9}$. Phys. Rev. B, **50**, 3458--3461 (1994). ◇ Cited on page 13.

[111] Basov, D. N., Liang, R., Bonn, D. A., Hardy, W. N., Dabrowski, B., Quijada, M., Tanner, D. B., Rice, J. P., Ginsberg, D. M., and Timusk, T. In-Plane Anisotropy of the Penetration Depth in $YBa_2Cu_3O_{7-\delta}$ and $YBa_2Cu_4O_8$ Superconductors. Phys. Rev. Lett., **74**, 598--601 (1995). ◇ Cited on pages 13 & 72.

[112] Zhang, K., Bonn, D. A., Kamal, S., Liang, R., Baar, D. J., Hardy, W. N., Basov, D., and Timusk, T. Measurement of the *ab* Plane Anisotropy of Microwave Surface Impedance of Untwinned $YBa_2Cu_3O_{6.95}$ Single Crystals. Phys. Rev. Lett., **73**, 2484--2487 (1994). ◇ Cited on page 13.

[113] Gros, C., Joynt, R., and Rice, T. M. Superconducting instability in the large-U limit of the two-dimensional Hubbard model. Zeitschrift für Physik B Condensed Matter, **68**, 425--432 (1987). ◇ Cited on page 13.

[114] Weng, Z. Y., Lee, T. K., and Ting, C. S. d-wave superconducting condensation in the spin-density-wave background. Phys. Rev. B, **38**, 6561--6567 (1988). ◇ Cited on page 13.

[115] Monthoux, P., Balatsky, A. V., and Pines, D. Toward a theory of high-temperature superconductivity in the antiferromagnetically correlated cuprate oxides. Phys. Rev. Lett., **67**, 3448--3451 (1991). ◇ Cited on page 13.

[116] Annett, J., Goldenfeld, N., and Renn, S. R. Interpretation of the temperature dependence of the electromagnetic penetration depth in $YBa_2Cu_3O_{7-\delta}$. Phys. Rev. B, **43**, 2778--2782 (1991). ◇ Cited on page 13.

[117] Annet, J. F., Goldenfeld, N., and Renn, S. R. Physical properties of high temperature superconductors II, edited by D. M. Ginsberg. World Scientific (1989). ◇ Cited on page 13.

[118] C. P. Poole, H. A. F. and Creswick, R. J. Superconductivity. Academic press, 2nd ed. edn. (1995). ◇ Cited on page 13.

[119] Suter, A., Morenzoni, E., Khasanov, R., Luetkens, H., Prokscha, T., and Garifianov, N. Direct Observation of Nonlocal Effects in a Superconductor. Phys. Rev. Lett., **92**, 087001 (2004). ◇ Cited on page 13.

[120] Amin, M. H. S., Affleck, I., and Franz, M. Low-temperature behavior of the vortex lattice in unconventional superconductors. Phys. Rev. B, **58**, 5848--5855 (1998). ◇ Cited on page 13.

[121] Sonier, J. E., Hundley, M. F., Thompson, J. D., and Brill, J. W. Low Field Anomaly in the Specific Heat of s-Wave Superconductors due to the Expansion of the Vortex Cores. Phys. Rev. Lett., **82**, 4914--4917 (1999). ◇ Cited on page 13.

[122] Sonier, J. E., Brewer, J. H., and Kiefl, R. F. μSR studies of the vortex state in type-II superconductors. Rev. Mod. Phys., **72**, 769--811 (2000). ◇ Cited on page 13.

[123] Maisuradze, A., Khasanov, R., Shengelaya, A., and Keller, H. Comparison of different methods for analyzing μSR line shapes in the vortex state of type-II superconductors. Journal of Physics: Condensed Matter, **21**, 075701 (15pp) (2009). ◇ Cited on page 13.

[124] Sonier, J. E., et al. Hole-doping dependence of the magnetic penetration depth and vortex core size in $YBa_2Cu_3O_{6+x}$: Evidence for stripe correlations near (1/8) hole doping. Physical Review B (Condensed Matter and Materials Physics), **76**, 134518 (2007). ◇ Cited on pages 13 & 72.

[125] Sonier, J. E., Kiefl, R. F., Brewer, J. H., Chakhalian, J., Dunsiger, S. R., MacFarlane, W. A., Miller, R. I., Wong, A., Luke, G. M., and Brill, J. W. Muon-Spin Rotation Measurements of the Magnetic Field Dependence of the Vortex-Core Radius and Magnetic Penetration Depth in $NbSe_2$. Phys. Rev. Lett., **79**, 1742--1745 (1997). ◇ Cited on page 13.

[126] Fiory, A. T., Hebard, A. F., Mankiewich, P. M., and Howard, R. E. Renormalization of the Mean-Field Superconducting Penetration Depth in Epitaxial $YBa_2Cu_3O_7$ Films. Phys. Rev. Lett., **61**, 1419--1422 (1988). ◇ Cited on pages 13 & 14.

[127] Ma, Z., Taber, R. C., Lombardo, L. W., Kapitulnik, A., Beasley, M. R., Merchant, P., Eom, C. B., Hou, S. Y., and Phillips, J. M. Microwave penetration depth measurements on $Bi_2Sr_2CaCu_2O_8$ single crystals and $YBa_2Cu_3O_{7-\delta}$ thin films . Phys. Rev. Lett., **71**, 781--784 (1993). ◇ Cited on pages 13 & 14.

[128] Klein, N., Tellmann, N., Schulz, H., Urban, K., Wolf, S. A., and Kresin, V. Z. Evidence of two-gap *s*-wave superconductivity in $YBa_2Cu_3O_{7-\delta}$ from microwave surface impedance measurements. Phys. Rev. Lett., **71**, 3355--3358 (1993). ◇ Cited on pages 13 & 14.

[129] Gorter, C. *Paramagnetic Relaxation*, vol. 1 of Course of Theoretical Physics. Elsevier, second edn. (1947). ◇ Cited on page 16.

[130] Blatt, F. Modern physics. Physics series, McGraw-Hill (1992). ◇ Cited on page 16.

[131] Yang, C. N. Concept of Off-Diagonal Long-Range Order and the Quantum Phases of Liquid He and of Superconductors. Rev. Mod. Phys., **34**, 694--704 (1962). ◇ Cited on pages 19 & 20.

[132] Nieh, H. T., Su, G., and Zhao, B.-H. Off-diagonal long-range order: Meissner effect and flux quantization. Phys. Rev. B, **51**, 3760--3764 (1995). ◇ Cited on page 19.

[133] Sewell, G. L. Off-diagonal long-range order and the Meissner effect. Journal of Statistical Physics, **61**, 415--422 (1990). ◇ Cited on page 20.

[134] Fisher, M. P. A. Vortex-glass superconductivity: A possible new phase in bulk high-T_c oxides. Phys. Rev. Lett., **62**, 1415--1418 (1989). ◇ Cited on page 20.

[135] Kuroki, K., Onari, S., Arita, R., Usui, H., Tanaka, Y., Kontani, H., and Aoki, H. Unconventional Pairing Originating from the Disconnected Fermi Surfaces of Superconducting $LaFeAsO_{1-x}F_x$. Phys. Rev. Lett., **101**, 087004 (2008). ◇ Cited on page 20.

[136] Sigrist, M. and Rice, T. M. Symmetry classification of states in high temperature superconductors. Zeitschrift für Physik B Condensed Matter, **68**, 9--14 (1987). ◇ Cited on page 20.

[137] Wenger, F. and Östlund, S. *d*-wave pairing in tetragonal superconductors. Phys. Rev. B, **47**, 5977--5983 (1993). ◇ Cited on page 20.

[138] Li, Q. P., Koltenbah, B. E. C., and Joynt, R. Mixed s-wave and d-wave superconductivity in high-T_c systems. Phys. Rev. B, **48**, 437--455 (1993). ◇ Cited on page 20.

[139] Zhang, S.-C. A Unified Theory Based on SO(5) Symmetry of Superconductivity and Antiferromagnetism. Science, **275**, 1089--1096 (1997). ◇ Cited on page 20.

[140] Kirtley, J. R., Tsuei, C. C., Ariando, Verwijs, C. J. M., Harkema, S., and Hilgenkamp, H. Angle-resolved phase-sensitive determination of the in-plane gap symmetry in $YBa_2Cu_3O_{7-\delta}$. Nat Phys, **2**, 190--194 (2006). ◇ Cited on page 21.

[141] Kirtley, J. R., Tsuei, C. C., Sun, J. Z., Chi, C. C., Yu-Jahnes, L. S., Gupta, A., Rupp, M., and Ketchen, M. B. Symmetry of the order parameter in the high-T_c superconductor $YBa_2Cu_3O_{7-\delta}$. Nature, **373**, 225--228 (1995). ◇ Cited on page 21.

[142] Tsuei, C. C., Kirtley, J. R., Hammerl, G., Mannhart, J., Raffy, H., and Li, Z. Z. Robust $d_{x^2-y^2}$ Pairing Symmetry in Hole-Doped Cuprate Superconductors. Phys. Rev. Lett., **93**, 187004 (2004). ◇ Cited on page 21.

[143] Mazin, I. I. Superconductivity gets an iron boost. Nature, **464**, 183--186 (2010). ◇ Cited on page 22.

[144] Mazin, I. I., Singh, D. J., Johannes, M. D., and Du, M. H. Unconventional Superconductivity with a Sign Reversal in the Order Parameter of $LaFeAsO_{1-x}F_x$. Phys. Rev. Lett., **101**, 057003 (2008). ◇ Cited on page 21.

[145] Wu, C. S., Ambler, E., Hayward, R. W., Hoppes, D. D., and Hudson, R. P. Experimental test of parity conservation in beta decay. Phys. Rev., **105**, 1413--1415 (1957). ◇ Cited on page 26.

[146] Nakamura, K. and Group, P. D. Review of Particle Physics. Journal of Physics G: Nuclear and Particle Physics, **37**, 075021 (2010). ◇ Cited on page 26.

[147] Riseman, T. Ph.D. Thesis: μSR MEASUREMENT OF THE MAGNETIC PENETRATION DEPTH AND COHERENCE LENGTH IN THE HIGH-T_C SUPERCONDUCTOR $YBa_2Cu_3O_{6.95}$. University Of British Columbia (1993). ◇ Cited on page 28.

[148] Morris, G. Ph.D. Thesis: Muonium Formation and Diffusion in Cryocrystals. University Of British Columbia (1997). ◇ Cited on page 28.

[149] Schenck, A. Muon Spin Spectroscopy. Hilger, Bristol (1985). ◇ Cited on page 28.

[150] Cox, S. F. J. Implanted muon studies in condensed matter science. Journal of Physics C: Solid State Physics, **20**, 3187 (1987). ◇ Cited on page 28.

[151] Keller, H. Muon-spin rotation experiments in high-T_c superconductors and related materials. IBM Journal of Research and Development, **33**, 314 --323 (1989). ◇ Cited on page 28.

[152] Chow, K. Ph.D. Thesis: Spin dynamics and electronic structure of muonium and its charged states in silicon and gallium arsenide. University Of British Columbia (1994). ◇ Cited on page 28.

[153] Luke, G. Ph.D. Thesis: Quantum diffusion and spin dynamics of muons in copper. University Of British Columbia (1988). ◇ Cited on page 28.

[154] Prokscha, T., Morenzoni, E., Deiters, K., Foroughi, F., George, D., Kobler, R., Suter, A., and Vrankovic, V. The new μE4 beam at PSI: A hybrid-type large acceptance channel for the generation of a high intensity surface-muon beam. Nuclear Instruments and Methods in Physics Research Section A: Accelerators, Spectrometers, Detectors and Associated Equipment, **595**, 317 -- 331 (2008). ◇ Cited on page 29.

[155] Luetkens, K. Ph.D. Thesis. Gemeinsamen Naturwissenschaftlichen Fakultt der Technischen Universitat Carolo-Wilhelmina zu Braunschweig (2004). ◇ Cited on pages 30 & 31.

[156] Morenzoni, E., Glückler, H., Prokscha, T., Khasanov, R., Luetkens, H., Birke, M., Forgan, E. M., Niedermayer, C., and Pleines, M. Implantation studies of kev positive muons in thin metallic layers. Nuclear Instruments and Methods in Physics Research Section B: Beam Interactions with Materials and Atoms, **192**, 254 -- 266 (2002). ◇ Cited on pages 30 & 37.

[157] Wojek, B. M. Superconductivity and magnetism in cuprate single crystals and thin-film heterostructures. Ph.D. thesis, University of Zurich (2011). ◇ Cited on pages 32 & 45.

[158] Ziegler, J. F. (2011), The stopping and range of ions in matter. ◇ Cited on page 36.

[159] Eckstein, W. Computer Simulation of Ion-Solid Interactions. Springer, Berlin (1991). ◇ Cited on page 36.

[160] Morenzoni, E., Prokscha, T., Suter, A., Luetkens, H., and Khasanov, R. Nano-scale thin film investigations with slow polarized muons. Journal of Physics: Condensed Matter, **16**, S4583 (2004). ◇ Cited on page 37.

[161] Riseman, T. M. and Forgan, E. M. (1999), Maxmimum Entropy Fourier Analysis μSR: A Manual for MaxError. [Online; accessed 5-May-2012]. ◇ Cited on page 39.

[162] Riseman, T. and Forgan, E. Maximum entropy μSR analysis i: planting the kernel. Physica B: Condensed Matter, **326**, 226 -- 229 (2003). ◇ Cited on pages 39 & 43.

[163] Riseman, T. and Forgan, E. Maximum entropy μSR analysis ii: the search for truthful errors. Physica B: Condensed Matter, **326**, 230 -- 233 (2003). ◇ Cited on pages 39 & 43.

[164] Riseman, T. and Forgan, E. Maximum entropy μSR analysis iii: automatic selection of the default level and looseness factor. Physica B: Condensed Matter, **326**, 234 -- 237 (2003). ◇ Cited on pages 39 & 43.

[165] Liang, R., Bonn, D. A., and Hardy, W. N. Growth of high quality YBCO single crystals using BaZrO3 crucibles. Physica C: Superconductivity, **304**, 105 -- 111 (1998). ◇ Cited on page 41.

[166] Doiron-Leyraud, N., Proust, C., LeBoeuf, D., Levallois, J., Bonnemaison, J.-B., Liang, R., Bonn, D. A., Hardy, W. N., and Taillefer, L. Quantum oscillations and the Fermi surface in an underdoped high-T_c superconductor. Nature Publishing Group, **447**, 565--568 (2007). ◇ Cited on pages 42 & 74.

[167] Nagamine, K., Nagamiya, S., Hashimoto, O., Nishida, N., Yamazaki, T., and Patterson, B. D. Temperature-independent hyperfine field on μ^+ in nickel in the temperature range of 0.12-300 K. Hyperfine Interactions, **1**, 517--532 (1975). ◇ Cited on page 42.

[168] Saadaoui, H., Salman, Z., Prokscha, T., Suter, A., Wojek, B., and Morenzoni, E. Zero-field spin depolarization of low-energy muons in ferromagnetic nickel and silver metal. Physics Procedia, **30**, 164 -- 167 (2012), 12th International Conference on Muon Spin Rotation, Relaxation and Resonance (μSR2011). ◇ Cited on page 44.

[169] Jackson, T. J., et al. Depth-Resolved Profile of the Magnetic Field beneath the Surface of a Superconductor with a Few nm Resolution. Phys. Rev. Lett., **84**, 4958--4961 (2000). ◇ Cited on pages 47 & 72.

[170] Prozorov, R. and Giannetta, R. W. Magnetic penetration depth in unconventional superconductors. Superconductor Science and Technology, **19**, R41 (2006). ◇ Cited on page 51.

[171] Kogan, V. G., Fang, M. M., and Mitra, S. Reversible magnetization of high-T_c materials in intermediate fields. Phys. Rev. B, **38**, 11958--11961 (1988). ◇ Cited on page 51.

[172] Microwave penetration depth measurements at 1GHz. Accessed: 26/06/2012. ◇ Cited on pages 52, 57, 58 & 65.

[173] Bonn, D. A., Kamal, S., Bonakdarpour, A., Liang, R., Hardy, W. N., Homes, C., Basov, D., and Timusk, T. Surface Impedance Studies of YBCO. Czech. J. Phys., **46**, 3195 (1995). ◇ Cited on pages 52, 57, 58 & 65.

[174] Liang, R., Dosanjh, P., Bonn, D. A., Hardy, W. N., and Berlinsky, A. J. Lower critical fields in an ellipsoid shaped $YBa_2Cu_3O_{6.95}$ single crystal. Phys. Rev. B, **50**, 4212--4215 (1994). ◇ Cited on page 51.

[175] Fournier, D., et al. Loss of nodal quasiparticle integrity in underdoped $YBa_2Cu_3O_{6+x}$. Nature Physics, **6**, 905--911 (2010). ◇ Cited on page 51.

[176] Limonov, M. F., Rykov, A. I., Tajima, S., and Yamanaka, A. Superconductivity-induced effects on phononic and electronic raman scattering in twin-free $YBa_2Cu_3O_{7-\delta}$ single crystals. Phys. Rev. B, **61**, 12412--12419 (2000). ◇ Cited on page 51.

[177] Kirtley, J. R., Tsuei, C. C., Ariando, Verwijs, C. J. M., Harkema, S., and Hilgenkamp, H. Angle-resolved phase sensitive determination of the in-plane gap symmetry in $YBa_2Cu_3O_{7-\delta}$. Nat. Phys., **2**, 190--194 (2006). ◇ Cited on page 51.

[178] Khasanov, R., Strässle, S., Di Castro, D., and Masui, T. *et al.*. Multiple Gap Symmetries for the Order Parameter of Cuprate Superconductors from Penetration Depth Measurements. Phys. Rev. Lett., **99**, 237601 (2007). ◇ Cited on page 51.

[179] Ni, N., Tillman, M. E., Yan, J.-Q., Kracher, A., Hannahs, S. T., Bud'ko, S. L., and Canfield, P. C. Effects of Co substitution on thermodynamic and transport properties and anisotropic H_{c2} in $BaCo_xFe_{2-x}As_2$ single crystals. Phys. Rev. B, **78**, 214515 (2008). ◇ Cited on page 67.

[180] Kim, H., et al. London penetration depth in $Ba(T_xFe_{1-x})_2As_2$(T=Co, Ni) superconductors irradiated with heavy ions. Phys. Rev. B, **82**, 060518 (2010). ◇ Cited on page 70.

[181] Gordon, R. T., et al. Unconventional London Penetration Depth in Single-Crystal $Ba(Co_{0.07}Fe_{0.93})_2As_2$ Superconductors. Phys. Rev. Lett., **102**, 127004 (2009). ◇ Cited on page 70.

[182] Luan, L., Auslaender, O. M., Lippman, T. M., Hicks, C. W., Kalisky, B., Chu, J.-H., Analytis, J. G., Fisher, I. R., Kirtley, J. R., and Moler, K. A. Local measurement of the penetration depth in the pnictide superconductor $Ba(Co_{0.05}Fe_{0.95})_2As_2$. Phys. Rev. B, **81**, 100501 (2010). ◇ Cited on pages 70 & 73.

[183] Lippman, T. M., Kalisky, B., Kim, H., Tanatar, M. A., Bud'ko, S. L., Canfield, P. C., and Moler, K. A. (2012), Agreement between local and global measurements of the London penetration depth. ◇ Cited on page 70.

[184] Ofer, O., et al. Absolute value and temperature dependence of the magnetic penetration depth in $Ba(Co_{0.074}Fe_{0.926})_2As_2$. Phys. Rev. B, **85**, 060506 (2012). ◇ Cited on page 71.

[185] Pereg-Barnea, T., Turner, P. J., Harris, R., Mullins, G. K., Bobowski, J. S., Raudsepp, M., Liang, R., Bonn, D. A., and Hardy, W. N. Absolute values of the London penetration depth in $YBa_2Cu_3O_{6+x}$ measured by zero field ESR spectroscopy on Gd doped single crystals. Phys. Rev. B, **69**, 184513 (2004). ◇ Cited on pages 72, 73 & 74.

[186] Ager, C., et al. Angular-dependent muon-spin rotation and torque magnetometry on the mixed state of the high-temperature superconductor $YBa_2Cu_3O_{6+x}$. Phys. Rev. B, **62**, 3528--3533 (2000). ◇ Cited on page 72.

[187] Johnson, S. T., et al. Flux-Line Lattice Structures in Untwinned $YBa_2Cu_3O_{6+x}$. Phys. Rev. Lett., **82**, 2792--2795 (1999). ◇ Cited on page 72.

[188] Prozorov, R., Tanatar, M., Gordon, R., Martin, C., Kim, H., Kogan, V., Ni, N., Tillman, M., Bud'ko, S., and Canfield, P. Anisotropic london penetration depth and superfluid density in single crystals of iron-based pnictide superconductors. Physica C: Superconductivity, **469**, 582 -- 589 (2009). ◇ Cited on page 73.

[189] Luan, L., Lippman, T. M., Hicks, C. W., Bert, J. A., Auslaender, O. M., Chu, J.-H., Analytis, J. G., Fisher, I. R., and Moler, K. A. Local Measurement of the Superfluid Density in the Pnictide Superconductor $BaCo_xFe_{2-x}As_2$ across the Superconducting Dome. Phys. Rev. Lett., **106**, 067001 (2011). ◇ Cited on page 73.

[190] Normand, B. and Kampf, A. P. Lattice anisotropy as the microscopic origin of static stripes in cuprates. Phys. Rev. B, **64**, 024521 (2001). ◇ Cited on page 74.

[191] Ando, Y., Segawa, K., Komiya, S., and Lavrov, A. N. Electrical Resistivity Anisotropy from Self-Organized One Dimensionality in High-Temperature Superconductors. Phys. Rev. Lett., **88**, 137005 (2002). ◇ Cited on page 74.

[192] Aeppli, G., Ansaldo, E. J., Brewer, J. H., Cava, R. J., Kiefl, R. F., Kreitzman, S. R., Luke, G. M., and Noakes, D. R. Magnetic penetration depth and flux-pinning effects in high-T_c superconductor $La_{1.85}Sr0_{.15}CuO$. Phys. Rev. B, **35**, 7129--7132 (1987). ◇ Cited on page 76.

[193] Huebener, R. P. Flux Structures in Superconductors. Springer (2001). ◇ Cited on page 76.

[194] Konczykowski, M., Burlachkov, L. I., Yeshurun, Y., and Holtzberg, F. Evidence for surface barriers and their effect on irreversibility and lower-critical-field measurements in Y-Ba-Cu-O crystals. Phys. Rev. B, **43**, 13707--13710 (1991). ◇ Cited on page 76.

[195] Dolan, G. J., Holtzberg, F., Feild, C., and Dinger, T. R. Anisotropic vortex structure in $YBa_2Cu_3O_7$. Phys. Rev. Lett., **62**, 2184--2187 (1989). ◇ Cited on page 76.

[196] Jooss, C., Forkl, A., Warthmann, R., Habermeier, H. U., Leibold, B., and Kronmüller, H. Thickness and roughness dependence of magnetic flux penetration and critical current densities in $YBa_2Cu_3O_{7-\delta}$ thin films. Physica C: Superconductivity, **266**, 235 -- 252 (1996). ◇ Cited on page 76.